Metal Oxide Surfaces; Beyond UHV

A thesis submitted to The University of Manchester for the degree of

Doctor of Philosophy (Ph.D.)

in the Faculty of Engineering and Physical Sciences

2014

Mahmoud H. M. Ahmed

… and say: "My Lord! Increase me in knowledge"

Contents

Word Count: 40, 500 Words

List of Tables

List of Figures

Abstract

In this thesis, three experimental studies of metal oxide surfaces beyond UHV conditions are presented, in an attempt to bridge the so-called 'pressure' gap. In the first of these studies, surface X-ray diffraction has been employed to elucidate the surface structure of α-Cr_2O_3(0001) as a function of water partial pressure at room temperature. In ultra high vacuum, subsequent to exposure to ~ 2000 Langmuir of H_2O, the surface is determined to be terminated by a partially occupied double layer of chromium atoms. No evidence of adsorbed OH/H_2O is found under this regime. At a water partial pressure of ~ 30 mbar, a surface termination involving a single OH/H_2O species bound atop to each surface Cr atom is obtained.

Surface X-ray diffraction has also been employed to elucidate the geometry of the $TiO_2(011)/H_2O$ interface at room temperature. In ultra high vacuum, a surface structure in quantitative agreement with previously published studies is found. Most notably at a water partial pressure of ~ 30 mbar, the interface geometry is determined to be consistent with the predicted structure emerging from *ab initio calculations* in which the surface undergoes transformation from a (2×1) reconstruction to a (1×1) unit cell.

In the final investigation a procedure for non-UHV *wet-chemical* preparation of TiO_2 single crystal substrates is detailed. The potential of this recipe is demonstrated through application to rutile-TiO_2(110) and rutile-TiO_2(011) substrates. Characterisation with scanning probe microscopy, low energy electron diffraction and auger electron spectroscopy, indicate that flat, well-ordered, carbon-free surfaces can be generated. Notably, in contrast to the (2×1) surface unit cell found for TiO_2(011) prepared in ultra high vacuum, *wet-chemical* preparation results in a (4×1) termination; *wet-chemically* prepared TiO_2(110) displays an unreconstructed (1x1) surface.

Declaration

No portion of the work referred to in the thesis has been submitted in support of an application for another degree or qualification of this or any other university or other institute of learning

Copy Right Statement

I. The author of this thesis (including any appendices and/or schedules to this thesis) owns certain copyright or related rights in it (the "Copyright") and s/he has given The University of Manchester certain rights to use such Copyright, including for administrative purposes.

II. Copies of this thesis, either in full or in extracts and whether in hard or electronic copy, may be made **only** in accordance with the Copyright, Designs and Patents Act 1988 (as amended) and regulations issued under it or, where appropriate, in accordance with licensing agreements which the University has from time to time. This page must form part of any such copies made.

III. The ownership of certain Copyright, patents, designs, trademarks and other intellectual property (the "Intellectual Property") and any reproductions of copyright works in the thesis, for example graphs and tables ("Reproductions"), which may be described in this thesis, may not be owned by the author and may be owned by third parties. Such Intellectual Property and Reproductions cannot and must not be made available for use without the prior written permission of the owner(s) of the relevant Intellectual Property and/or Reproductions.

IV. Further information on the conditions under which disclosure, publication and commercialisation of this thesis, the Copyright and any Intellectual Property and/or Reproductions described in it may take place is available in the University of Manchester IP Policy (see http://www.campus.manchester.ac.uk/medialibrary/policies/intellectual-property.pdf), in any relevant Thesis restriction declarations deposited in the University Library, The University Library's regulations (see http://www.manchester.ac.uk/library/aboutus/regulations) and in The University's policy on presentation of Theses.

Acknowledgements

All praise is due to the all Mighty Allah (T) alone! Peace and blessings be upon His final messenger Mohammed (S), who said: ‘Whoever does not thank people (for their favour) has not thanked Allah (properly), Mighty and Glorious is He!’

Accordingly, I owe a great debt of thanks to the many people without whose support and expertise this thesis would have never seen the light of day!

Firstly, thanks are due to Dr. Rob Lindsay, my supervisor, for his inspiring enthusiasm, endless patience, helpful support and friendship during the past few years; it has been a great opportunity and honour for me to work with him. Particular thanks are also due to the remaining members of my (*direct* and *indirect*) supervisory team: Prof. David Vaughan, the late Dr. Paul Wincott, Dr. Hadeel Hussain and Dr. Xavier Torrelles. All of whom have given me freely of their time and expertise, and without whose guidance this work would have been impossible.

Finally this thesis would have not been possible without the endless encouragement and support of my family, in particular my parents, whose help and emotional support has been of immense value to me my whole life.

(This page intentionally left blank)

Chapter 1

Introduction

1.1. Aims and Objectives

There are a number of different physical and chemical processes that occur at surfaces and interfaces; the study of which is of great technological and scientific importance. The continual growth in studies of solid surfaces, since the establishment of modern surface science some 50 years ago [1-3], has also driven the development of experimental techniques with ability to detect finer surface details; the frontiers of surface science instrumentation are constantly being pushed. Consequently the ability to prepare and study well-characterised surfaces brought about by this ongoing development of many of these surface sensitive techniques has seen many researchers over the years turn their attention to metal oxide surfaces, which were predominately ignored in the early days of surface science due to their perceived complexity. The crystallographic, physical, chemical and electronic structure of metal oxide surfaces are far more complex than that of metals [2, 4].

Metal oxides are employed widely throughout industry in a huge variety of areas and their surfaces play crucial roles in an extremely wide range of technological phenomena [4]. These include catalysis, corrosion control coatings, solar cells, data storage devices and electronics [4].

In addition to their technological importance, oxide surfaces and interfaces are amazing systems for fundamental studies. Metal oxides can be found practically everywhere in nature; after all every metal, with exception of gold, forms an oxide when exposed to the ambient atmosphere [3]. They constitute a diverse and fascinating class of materials, which present a wide range of properties ranging from insulators to superconducting materials, from opaque to transparent, from magnetic to non-magnetic.

Until recently the vast majority of such studies have been concerned with highly idealised model systems; a single crystal substrate prepared in an ultra high vacuum

(UHV) environment. Quite justifiably, as a starting point, it is only by the study of such model systems that a deep and reliable mechanistic understanding of the physical and chemical properties of more complex surfaces may be achieved. However, such conditions are quite obviously far removed from the 'real world' or relevant operating environment of many technological systems. Such a dilemma has been termed a *'pressure'* or *'material'* gap [5], and must be taken into careful consideration when interpreting results for industrially relevant applications obtained from research carried out under surface science conditions.

More recently, many researchers have begun to focus their attention on bridging this gap by performing experiments in more relevant temperature and pressure environments, and with materials that more closely resembling the technologically relevant material. However, one obstacle to more technologically relevant studies concerns sample preparation. Broadly speaking there seems to be two possible approaches to sample preparation that can be taken, Pang *et al* [6] discuss the advantages and disadvantages of both. The first being sample preparation in UHV, followed by introduction into the relevant environment e.g. liquid/ ambient or high pressure, and the second involves sample preparation outside of UHV or the so-called non-UHV preparation. In the latter, sample characterisation must ensure that the surface is prepared well enough to meet the rigorous conditions of surface science studies i.e. ensuring the production of a well-ordered and largely contamination-free surface.

The *'pressure'* gap between the current understanding from model studies and the technologically relevant environment is the main motivation behind the studies described in this thesis. The materials probed here are chromium oxide and titanium dioxide.

1.2. Thesis Approach and Structure

The results Chapters (Chapters 4-6) of this thesis have been written in scientific paper format. Whilst this may lead to some repetition between chapters, it allows each chapter to stand-alone as a piece of independent scientific research, and indeed all these chapters have either been published or are in the process of being published.

Chapter 2 describes the theoretical background, experimental practicalities and instrumentation behind a number of experimental techniques, which are of importance to the studies in this thesis. A relatively thorough understanding of these techniques is vital when it comes to the analysis of the results obtained from experiments.

Chapter 3 provides a brief review of the current knowledge of the substrate materials investigated in this thesis, namely the (0001) surface of chromium dioxide, and the (110) and (011) surfaces of rutile titanium dioxide. Subsequent to describing the bulk structure, the clean surface structure of each respective material is discussed.

Research results are presented in Chapters 4, 5 and 6. The first of these studies investigating the surface geometry of the α-Cr_2O_3(0001) surface as a function of H_2O partial pressures, is described in Chapter 4. Motivated by the central role of surface chromia in the corrosion resistance of stainless steels [7], the goal of the work presented in this chapter is to quantitatively determine, using surface X-ray diffraction (SXRD), the impact of H_2O vapour on the surface structure of α-Cr_2O_3(0001). In contrast to the lack of experimental data, the surface structure as a function of H_2O partial pressure has been studied by means of first principle calculations [8]. It's concluded experimentally in this chapter that at room temperature and high pressure, water undergoes dissociation to form surface hydroxyls. At UHV, the surface is found to exhibit a partially occupied double layer of chromium atoms, a geometry largely consistent with that derived from previous SXRD [9] and quantitative low energy electron diffraction (LEED) [10] measurements, although there are some small differences in atomic coordinates and fractional layer occupancies. Upon increasing the H_2O partial pressure to the mbar regime, a phase where a single hydroxyl is bound to each surface Cr, i.e. the surface is fully hydroxylated, is found to be most stable. *Ab initio* calculations performed to date failed to predict the experimentally determined structure at higher H_2O partial pressure.

In Chapter 5 the quantitative determination of the geometric structure at the TiO_2(011)/H_2O interface employing SXRD is reported. The structure of clean rutile TiO_2(011) in UHV appears to be well understood, having been confirmed in several independent quantitative studies using SXRD [11, 12] and LEED-IV [13]; i.e. it presents a saw-tooth-like morphology with five-fold coordinated titanium and two-fold coordinated surface oxygen atoms arranged in rows along the $[01\bar{1}]$ direction. The surface geometry under an aqueous environment has, in contrast to the clean surface, only been studied by means of first principles calculations [14]. It is predicted that water dissociates at the interface to form hydroxyls, with a restructuring of the substrate towards a bulk (1×1) termination in the presence of an aqueous environment. The surface structure resulting from SXRD measurements in this study are largely consistent with this predicted geometry.

Recently, several groups (e.g. [15-17]) have attempted to prepare metal oxide surfaces, typically the TiO_2(110) surface, without resorting to UHV to provide a simpler route to studies of metal oxide surfaces in more technologically relevant environments. Chapter 6 is devoted to an alternative non-UHV wet chemical recipe for preparation of $TiO_2(110)$ and $TiO_2(011)$ for surface studies. Most importantly, the employment of hydrofluoric acid, which is difficult to handle, has been circumvented, replacing it with aqua regia (HCl and HNO_3). UV treatment was also undertaken in a final step to remove adventitious carbon contamination. The utility of this methodology has been critically assessed through characterisation of surface structure and composition of the prepared surfaces.

Finally, Chapter 7 provides a brief summary of the results presented in this thesis and proposes pathways for future research to build on the work presented here.

1.3. References

[1] G.A. Somorjai, Surface science and catalysis, Science, 227 (1985) 902-908.

[2] H.-J. Freund, Introductory Lecture: Oxide surfaces, Faraday Discussions, 114 (1999) 1-31.

[3] U. Diebold, S.-C. Li, M. Schmid, Oxide Surface Science, Annual Review of Physical Chemistry, 61 (2010) 129-148.

[4] V.E. Henrich, P.A. Cox, The Surface Science of Metal Oxides, First ed., Cambridge University Press, 1994.

[5] M. Bron, D. Teschner, A. Knop-Gericke, B. Steinhauer, A. Scheybal, M. Havecker, D. Wang, R. Fodisch, D. Honicke, A. Wootsch, R. Schlogl, P. Claus, Bridging the pressure and materials gap: in-depth characterisation and reaction studies of silver-catalysed acrolein hydrogenation, Journal of Catalysis, 234 (2005) 37-47.

[6] C.L. Pang, R. Lindsay, G. Thornton, Structure of Clean and Adsorbate-Covered Single-Crystal Rutile TiO_2 Surfaces, Chemical Reviews, 113 (2013) 3887-3948.

[7] V. Maurice, W.P. Yang, P. Marcus, XPS and STM study of passive films formed on Fe-22Cr(110) single-crystal surfaces, Journal of the Electrochemical Society, 143 (1996) 1182-1200.

[8] D. Costa, K. Sharkas, M.M. Islam, P. Marcus, Ab initio study of the chemical states of water on Cr_2O_3(0001): From the isolated molecule to saturation coverage, Surface Science, 603 (2009) 2484-2493.

[9] O. Bikondoa, W. Moritz, X. Torrelles, H.J. Kim, G. Thornton, R. Lindsay, Impact of ambient oxygen on the surface structure of alpha-Cr_2O_3(0001), Physical Review B, 81 (2010) 205439.

[10] M. Lubbe, W. Moritz, A LEED analysis of the clean surfaces of alpha-Fe_2O_3(0001) and alpha-Cr_2O_3(0001) bulk single crystals, Journal of Physics: Condensed Matter, 21 (2009) 134010.

[11] X. Torrelles, G. Cabailh, R. Lindsay, O. Bikondoa, J. Roy, J. Zegenhagen, G. Teobaldi, W.A. Hofer, G. Thornton, Geometric Structure of TiO_2(011)(2×1), Physical Review Letters, 101 (2008) 185501.

[12] X.-Q. Gong, N. Khorshidi, A. Stierle, V. Vonk, C. Ellinger, H. Dosch, H. Cheng, A. Selloni, Y. He, O. Dulub, U. Diebold, The 2×1 reconstruction of the rutile TiO_2(011) surface: A combined density functional theory, X-ray diffraction, and scanning tunneling microscopy study, Surface Science, 603 (2009) 138-144.

[13] S.E. Chamberlin, C.J. Hirschmugl, H.C. Poon, D.K. Saldin, Geometric structure of TiO_2(011)(2×1) surface by low energy electron diffraction (LEED), Surface Science, 603 (2009) 3367-3373.

[14] U. Aschauer, A. Selloni, Structure of the Rutile TiO_2(011) Surface in an Aqueous Environment, Physical Review Letters, 106 (2011) 166102.

[15] Y. Namai, O. Matsuoka, NC-AFM Observation of Atomic Scale Structure of Rutile-type TiO_2(110) Surface Prepared by Wet Chemical Process, The Journal of Physical Chemistry B, 110 (2006) 6451-6453.

[16] R. Shimizu, T. Hitosugi, K.S. Nakayama, T. Sakurai, M. Shiraiwa, T. Hasegawa, T. Hashizume, Preparation of Atomically Flat TiO_2(110) Substrate, Japanese Journal of Applied Physics, 48 (2009) 125506.

[17] Y. Yamamoto, K. Nakajima, T. Ohsawa, Y. Matsumoto, H. Koinuma, Preparation of Atomically Smooth TiO_2 Single Crystal Surfaces and Their Photochemical Property, Japanese Journal of Applied Physics, 44 (2005) L511-L514.

Chapter 2

Experimental Techniques: Principles, Theory and Practice

2.1 Introduction

The growing awareness, over the last fifty years or so, of the importance of understanding surface structure in order to gain an insight into surface phenomena for 'real world' applications has seen significant development of experimental techniques to gain such pertinent information from single crystal substrates. Analytical techniques include scattering/diffraction-based techniques for probing surface geometry e.g. surface X-ray diffraction (SXRD) and low energy electron diffraction (LEED I-V), and real space imaging approaches for understanding surface morphology and topography (e.g. Scanning Probe Microscopy (SPM)). In addition, emission based techniques are used for gaining an insight into the chemical composition of the surface, including X-ray photon spectroscopy (XPS) and Auger electron Spectroscopy (AES). All of which are typically employed in conjunction to get a complete understanding of the surface under consideration [1].

A number of these experimental techniques were employed to achieve the objectives of this thesis. Their theoretical foundations are described in the following sections, alongside experimental practicalities, and instrumentation.

2.2. Surface X-ray Diffraction (SXRD)

With the increasing availability of high-energy/flux synchrotron radiation, SXRD has become a standard technique for surface structure determination [2-5]. It is a quantitative surface probe, which allows atomic position determination, both parallel and perpendicular to the surface, to a very precise degree of accuracy; indeed with precision as small as ±0.01 Å [6].

SXRD has become a well-established technique for studying surfaces and interfaces owing primarily to the fact that X-rays interact weakly with matter. For small crystals (and by extension crystal surfaces) the amplitude of the scattered wave is much less than the incident wave amplitude, thus multiple scattering effects can be ignored, and single scattering approximation is sufficient to analyse the experimental data i.e. diffraction process can be treated by the kinematical rather than the dynamical theory of diffraction [7]. SXRD is not limited to only 'free' surfaces under UHV conditions, but can also be used with a great level of success on solid-solid interfaces, solid-liquid interfaces and gas-solid interfaces under varying pressure and temperature environments. This is important for understanding surface geometry in technologically relevant environments, for example, in heterogeneous catalysis reactions where the role of the catalyst can be studied under real (or near real) working conditions [8].

In the following section the theoretical basis upon which SXRD is built will be outlined. The kinematical theory of X-ray scattering is presented, and the difference between diffraction from two and three dimensional crystal structures is highlighted alongside key concepts. For further details the reader is referred to the excellent reviews by Als-Nielson and McMorrow [7], Feidenhans'l [3] and Robinson and Tweet [4].

2.2.1. Theoretical Considerations

The elastic scattering cross section of X-rays is very small compared to that of an electron. Consequently, the elastic scattering of X-rays is adequately described by the kinematical theory of diffraction and the total scattering amplitude is the sum of all the individual single-scattering events (i.e. multiple scattering is not important) [4].

It should be noted that Compton (or inelastic scattering) is incoherent, as there is no phase relationship between the incoming and scattered radiation, and so does not contribute to diffraction. Accordingly, Compton scattering just simply contributes to the background of the diffraction pattern and so can be largely ignored [4, 7].

In order to calculate the total scattering intensity/amplitude of an X-ray incident on a crystal surface, viewed from various angles at a distance R (large compared with the dimensions of the scattering center) it is necessary to build up to scattering from a crystal in stages, starting from the scattering of an incident plane wave of known wavelength from a single particle. The following section is derieved from references [4, 7].

2.2.1.1. Scattering from an Electron

The scattering of a monochromatic linear plane polarized electromagnetic wave (Amplitude = A_0) by an electron is given by the *Thompson scattering Formula* [9], which describes the amplitude of the scattered spherical wave, A_1, emerging from a scattering electron located at some distance defined by position vector r from the origin O (Figure 2.1), as a function of the amplitude of the incoming plane wave, A_0:

$$A_1 e^{(ik_f r)} = A_0 \frac{e^2}{mc^2 R_0} e^{i(k_i r)} \tag{2.1}$$

The scattering is observed at distance R_0 from the electron, where e is the electron charge, m its mass, and c is the speed of light.

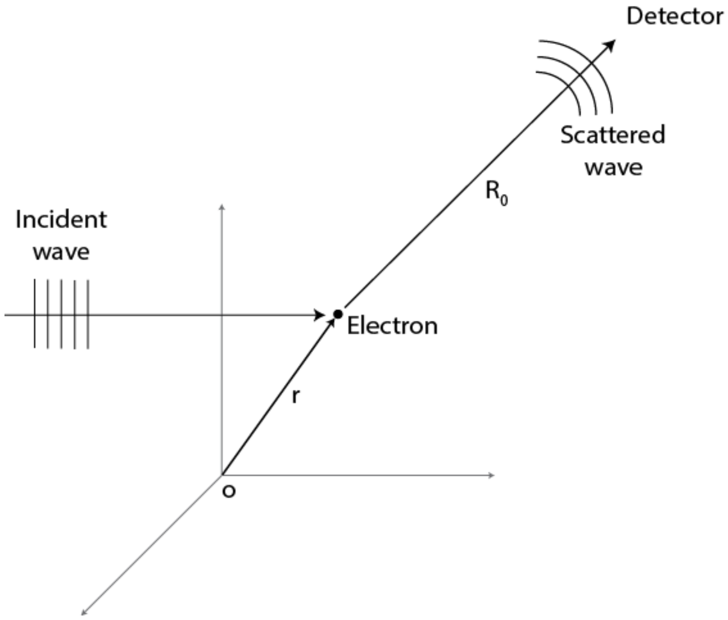

Figure 2.1: A schematic showing the scattering of a plane monochromatic electromagnetic wave from an electron at position r. Reproduced from [10].

In Equation 2.1 k_i represents the wave vector of the incoming wave in momentum space, and k_f represents the wave vector of the scattered wave. For elastic scattering:

$$|k_i| = |k_f| = |k| = \frac{2\pi}{\lambda} \tag{2.2}$$

and so it follows that the momentum transfer or wave vector transfer, depicted in Figure 2.2, is defined by a scattering vector, Q, such that:

$$Q = k_f - k_i \tag{2.3}$$

Given this definition of momentum transfer, it is then possible to rearrange Equation 2.1 yielding the following equation for the scattering amplitude of an elastically scattered wave by a single electron in momentum space:

$$A_1 = A_0 \frac{e^2}{mc^2 R_0} e^{iQr} \tag{2.4}$$

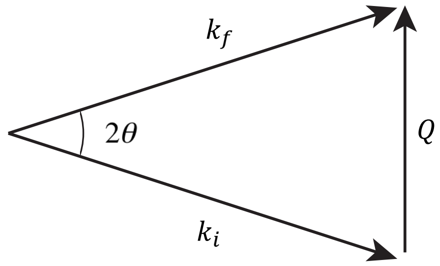

Figure 2.2: Schematic definition of momentum transfer, valid for elastic scattering.

2.2.1.2. Scattering from a Single Atom

An atom is essentially a dense nucleus surrounded by a cloud of Z electrons, and so the scattering amplitude from a single atom is the sum of the amplitudes scattered from each of the electrons within this atom, Figure 2.3.

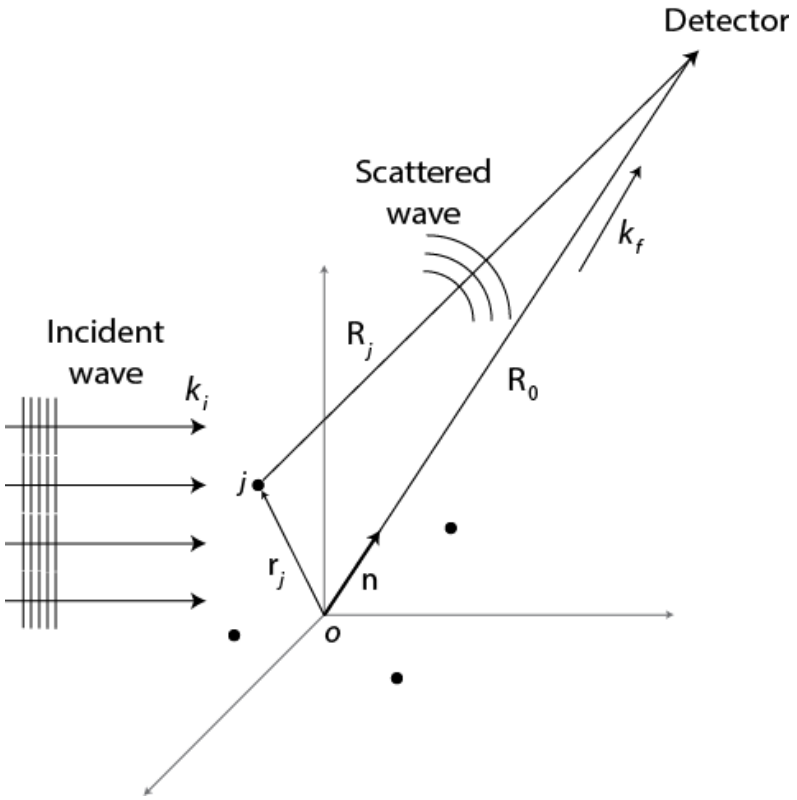

Figure 2.3: Scattering of a plane monochromatic electromagnetic wave from an assembly of j electrons in atom. The atomic nucleus is placed at the origin. Reproduced from [10].

Positioning the nucleus at the origin of the coordinate system and the electrons at positions $\{r_{e,j}\}$ it follows from Equation 2.4 that the scattering amplitude of an atom, A_{atom}, is defined by:

$$A_{atom} = A_0 \frac{e^2}{mc^2} \sum_{j=1}^{z} \frac{e^{iQr_j}}{R_{e,j}} \tag{2.5}$$

Where $R_{e,j}$ is the distance between electron j and the detector. The summation is over the total number of electrons in the atom. Given that the detector is positioned such that is it at distance R_0 from the origin of the coordinate system, namely the nucleus, along the direction indicated by the unit vector $\boldsymbol{n} \equiv {\boldsymbol{R_0}}/{R_0}$ it is possible to approximate $R_{e,j}$:

$$R_{e,j} \approx R_0 - \boldsymbol{n} \cdot \boldsymbol{r}_{e,j} \tag{2.6}$$

On this basis, one may replace $R_{e,j}$ in Equation 2.5 by R, yielding:

$$A_{atom} = A_0 \frac{e^2}{mc^2 R_0} \sum_{j=1}^{z} e^{iQr_{e,j}} \tag{2.7}$$

Thus far the electrons of an atom have been treated classically as point charges at positions $\{r_{e,j}\}$. However a quantum mechanical treatment dictates that each electron is observed as a spatially extended wave packet. On this basis the normalised probability density of an electron wave packet, $\rho_j(\boldsymbol{r})$, is given by:

$$\int \rho_j(\boldsymbol{r})\, d^3\boldsymbol{r} = 1 \tag{2.8}$$

Thus the contribution from the sum of electron wave packet $\int \rho_j(\boldsymbol{r})\, d^3\boldsymbol{r}$ is then:

$$\sum_{j=1}^{z} e^{iQr_{e,j}} \Rightarrow \int \rho_j(\boldsymbol{r})\, e^{iQr} d^3\boldsymbol{r} \tag{2.9}$$

and so,

$$A_{atom} = A_0 \frac{e^2}{mc^2 R} \int \rho_j(\boldsymbol{r}) e^{iQr} d^3 r = A_0 \frac{e^2}{mc^2 R} f(Q) e^{iQr} \tag{2.10}$$

The distance between scattering electrons within the atom and the fact that the X-ray wavelength is of the order of atomic dimensions [11], there will be path differences between the scattered waves. This is known as the atomic form or scattering factor, $f(Q)$, defined by the Fourier transform of the electron scattering density for a single electron:

$$f(Q) = \int \rho(r) e^{iQr} d^3 r \tag{2.11}$$

Provided that the wavelength of the incident X-ray is very short compared to the energies of any absorption edges in the atom, then when $Q = 0$ all the electrons in the atom scatter in phase and $f(Q)$ will be equal to the number of electrons surrounding the atom i.e. $f(Q = 0) = Z$. At all non-zero values of momentum transfer electrons start to scatter out of phase and $f(Q)$ decreases such that $f(Q \to \infty) = 0$. Values of $f(Q)$ for different elements have been compiled in the *International Tables for Crystallography* [12].

2.2.1.3. Scattering from a Crystal (One Unit Cell)

The scattering amplitude of a unit cell of a crystal is a summation of the scattering amplitudes of all the atoms inside the unit cell. If there are N atoms in a unit cell of a crystal at position $\{r_j\}$, then:

$$A_{unit\ cell} = A_0 \frac{e^2}{mc^2 R_0} \sum_{j=1}^{N} f_j(Q) e^{iQr_j} = A_0 \frac{e^2}{mc^2 R_0} F(Q) \tag{2.12}$$

In order to distinguish between the atoms in the unit cell that may not all be of the same chemical element it is necessary to assign separate form factors, $f_j(Q)$, describing the jth atom defined by position vector r_j, the complex quantity:

$$F(Q) = \sum_{j=1}^{N} f_j(Q) e^{iQ \cdot r_j} \tag{2.13}$$

is known as the structure factor, this contains all the information about the atomic arrangement within the unit cell and is defined as the sum of the scattering contribution of individual atoms in a unit cell.

Until now it has been assumed that atoms are bound or fixed at definite positions in the crystal, but in reality atoms will undergo thermal vibrations about their equilibrium position. These temperature effects reduce intensity of diffraction features on the basis that they give rise to thermal diffuse scattering present in the 'background' in reciprocal space. This phenomenon is conveniently taken into account by the introduction of the Debye-Waller factor in the expression for the structure factor i.e.:

$$F(Q) = \sum_{j=1}^{N} f_j(Q) e^{-B_j \left(\frac{Q}{4\pi}\right)^2} e^{iQ \cdot r_j} \tag{2.14}$$

For isotropic vibration, the Debye-Waller parameter, B_j is given by:

$$B_j = \frac{8\pi^2}{3} \langle \mu_j^2 \rangle \tag{2.15}$$

where $\langle \mu_j^2 \rangle$ is the mean square thermal vibration amplitude.

Additionally, in real crystals some atomic positions may only be partially occupied, this is accounted for by including an occupancy parameter, θ_j, in the expression for the structure factor. It then becomes:

$$F(Q) = \sum_{j=1}^{N} \theta_j f_j(Q) e^{-B_j(\frac{Q}{4\pi})^2} e^{iQ\cdot r_j} \tag{2.16}$$

2.2.1.4. Scattering from a 3D crystal

A defining property of crystalline materials is their periodicity in space, and in its simplest form a crystal can be assumed to be block defined by the real space lattice vectors (a_1, a_2, a_3) and the position from the origin of (N_1, N_2, N_3) unit cells along the three crystal axes is given by the lattice vector R_n:

$$R_n = n_1 a_1 + n_2 a_2 + n_3 a_3 \tag{2.17}$$

where n_j take integer values. The total scattering amplitude from a crystal is thus given by adding up the individual contributions from the identical unit cells multiplied with its appropriate phase factor:

$$A_{Crystal} = A_0 \frac{e^2}{mc^2 R_0} F(Q) \sum_{n_1=0}^{N_1-1} \sum_{n_2=0}^{N_2-1} \sum_{n_3=0}^{N_3-1} e^{iQ\cdot R_n} \tag{2.18}$$

This is a summation over the lattice defined by the vector R_n and will only take a value of significance when scattering amplitude contributions from the crystal add in phase i.e. when the condition:

$$Q \cdot R_n = 2n\pi \tag{2.19}$$

is satisfied. Alternatively in reciprocal space:

$$Q = 2\pi G \tag{2.20}$$

G is the reciprocal space lattice vector such that any lattice site in reciprocal space is defined by:

$$G = hb_1 + kb_2 + lb_3 \tag{2.21}$$

(h, k, l) are integer value Miller indices. The reciprocal space lattice vectors b_j, which are orthogonal to a_i, defined such that:

$$a_i \cdot b_j = 2\pi\delta_{ij} \tag{2.22}$$

δ_{ij} is known as Kronecker's delta which is a piecewise function defining two integer variables:

$$\delta_{ij} = \begin{cases} 0, & if\ i \neq j \\ 1, & if\ i = j \end{cases} \tag{2.23}$$

Taking scalar product of lattice vectors in real space, R_n, and reciprocal space, G, leads to:

$$GR_n = 2\pi(hn_1 + kn_2 + ln_3) = 2\pi \times integer \tag{2.24}$$

Since all the terms on the Right Hand Side of this expression take integer values then it follows that Equation 2.19 is satisfied if:

$$G = Q \tag{2.25}$$

This equality shows that X-rays will scatter with considerable intensity, and thus $F(Q)$ is non vanishing, if and only if the momentum transfer, Q, coincides with the reciprocal lattice vector, G. This is known as the Laue condition. Scattering from a crystalline material is therefore confined to distinct points in reciprocal space.

The Laue condition is often written as three conditions that all satisfy Equation 2.24 and that need to be true simultaneously for diffraction to take place:

$$Q \cdot a_1 = 2\pi h \tag{2.26}$$

$$Q \cdot a_2 = 2\pi k \tag{2.27}$$

$$Q \cdot a_3 = 2\pi l \tag{2.28}$$

Given a momentum transfer, Q, that satisfies the Laue conditions outlined above the diffracted intensity for a lattice with Miller indices (h, k, l) is given by the squared modulus of the scattering amplitude:

$$I_{hkl} = \left| A_0 \frac{e^2}{mc^2 R_0} F(hb_1 + kb_2 + lb_3) N_1 N_2 N_3 \right|^2 = \left| A_0 \frac{e^2}{mc^2 R_0} F_{hkl} N_1 N_2 N_3 \right|^2 \tag{2.29}$$

F_{hkl} is the structure factor evaluated at the reciprocal lattice point (h, k, l). The diffracted intensity is therefore zero except at discrete sites that lie on a lattice in the space of momentum transfer vector Q i.e.

$$I_{hkl} = \begin{cases} 0, & Q \neq hb_1 + kb_2 + lb_3 \\ \left| A_0 \frac{e^2}{mc^2 R_0} F_{hkl} N_1 N_2 N_3 \right|^2, & Q = hb_1 + kb_2 + lb_3 \end{cases} \tag{2.30}$$

When the position of an atom in the unit cell is defined by the fractional coordinates $r_j = x_j a_1 + y_j a_2 + z_j a_3$ in real space then structure factor, Equation 2.12, can be rewritten as:

$$F_{hkl} = F(hb_1 + kb_2 + lb_3) = \sum_j \theta_j f_j(Q) e^{-B_j(\frac{Q}{4\pi})^2} e^{2\pi \cdot i(hx_j + ky_j + kz_j)} \tag{2.31}$$

2.2.1.5. Surface Diffraction

Atoms at the surface, defined as the top few layers of a crystal, may be displaced from the bulk positions or missing from certain sites or even different atoms types may be present. Consequently, the surface is said to have undergone either a *relaxation* or *reconstruction*. The difference between the surface and bulk unit cell is then that the surface unit cell is repeated only in the surface plane and not along the surface normal. Accordingly, the Laue condition along the surface normal is relaxed and the component of momentum transfer perpendicular to the surface becomes a continuous variable where the Miller index l is no longer required to be an integer value but indeed can assume any value. This results in streaks of intensity along the surface normal, as scattering is no longer isotropic i.e. scattering is sharp along the two in-plane directions and diffuse along the surface normal. These diffuse streaks that pass through the Bragg points are termed 'Crystal Truncation Rods' (*CTR*'s) as they arise from the crystal structure being truncated (owing to the two dimensional nature of surfaces). Diffraction from a surface does not occur at discrete points in reciprocal space but rather along rods, this is depicted by the schematic figure 2.4.)

An expression for the diffracted intensity from a surface is derived by taking into account the two dimensional character of a surface such that the surface lattice is described by only two lattice vectors (a_1, a_2) lying along the surface plane and a third r_n which describes the atomic position within the unit cell along the surface plane and the position in the direction of the surface normal. Therefore the nth atom in the surface is defined by the vector R_n such that:

$$R_n = n_1 a_1 + n_2 a_2 + r_n \tag{2.32}$$

with only two Laue conditions:

$$Q \cdot a_1 = 2\pi h \tag{2.33}$$

$$Q \cdot a_2 = 2\pi k \tag{2.34}$$

As Q_z the component of the Q normal to the surface is a continuous variable the scattering from the surface may arise at any position along z between two Bragg peaks and the diffracted intensity is therefore given by:

$$I_{hk} = \left| A_0 \frac{e^2}{mc^2 R_0} F(Q_z) N_1 N_2 \right|^2 \tag{2.35}$$

Robinson has derived an expression for the intensity distribution of a CTR in which the scattering amplitude, $A(Q)$, from one layer of atoms is summed over an infinite stack of layers by a suitable phase factor. If the absorption effects are neglected then the scattered amplitude from an infinite stack of such layers is given by:

$$F^{CTR} = A(Q)\sum_{j=0}^{\infty} e^{iQ_z a_3 j} = \frac{A(Q)}{1 - e^{iQ_z a_3}} \tag{2.36}$$

Q_z the momentum transfer along the surface normal is taken as:

$$Q_z = \frac{2\pi l}{a_3} \tag{2.37}$$

where l is continuous variable and not an integer Miller index. So:

$$F^{CTR} = \frac{A(Q)}{1 - e^{i2\pi l}} \tag{2.38}$$

The intensity distribution along a *CTR* is thus given by:

$$I^{CTR} = |F^{CTR}|^2 = \left|\frac{A(Q)}{1 - e^{i2\pi l}}\right|^2 = \frac{|A(Q)|^2}{4\sin^2(\pi l)} \tag{2.39}$$

In a kinematic approximation the total scattered amplitude is given by a phase sum of bulk and surface scattering:

$$F_{hk}^{CTR}(l) = F_{hk}^{Bulk}(l) + F_{hk}^{Surface}(l) \tag{2.40}$$

Scattering is divided into contributions from the bulk and from the surface region, taken as an arbitrary number of atomic layers above the bulk. At integer points in l, scattering from both the bulk and surface structure contribute to the overall intensity however is dominated by the bulk contribution.

At equidistant between integer points, known as the anti-Bragg region, bulk scattering is largely out of phase and so this region is more sensitive to surface structure and thus CTR's can be used to determine the atomic coordinates of atoms in the surface layers with high precision.

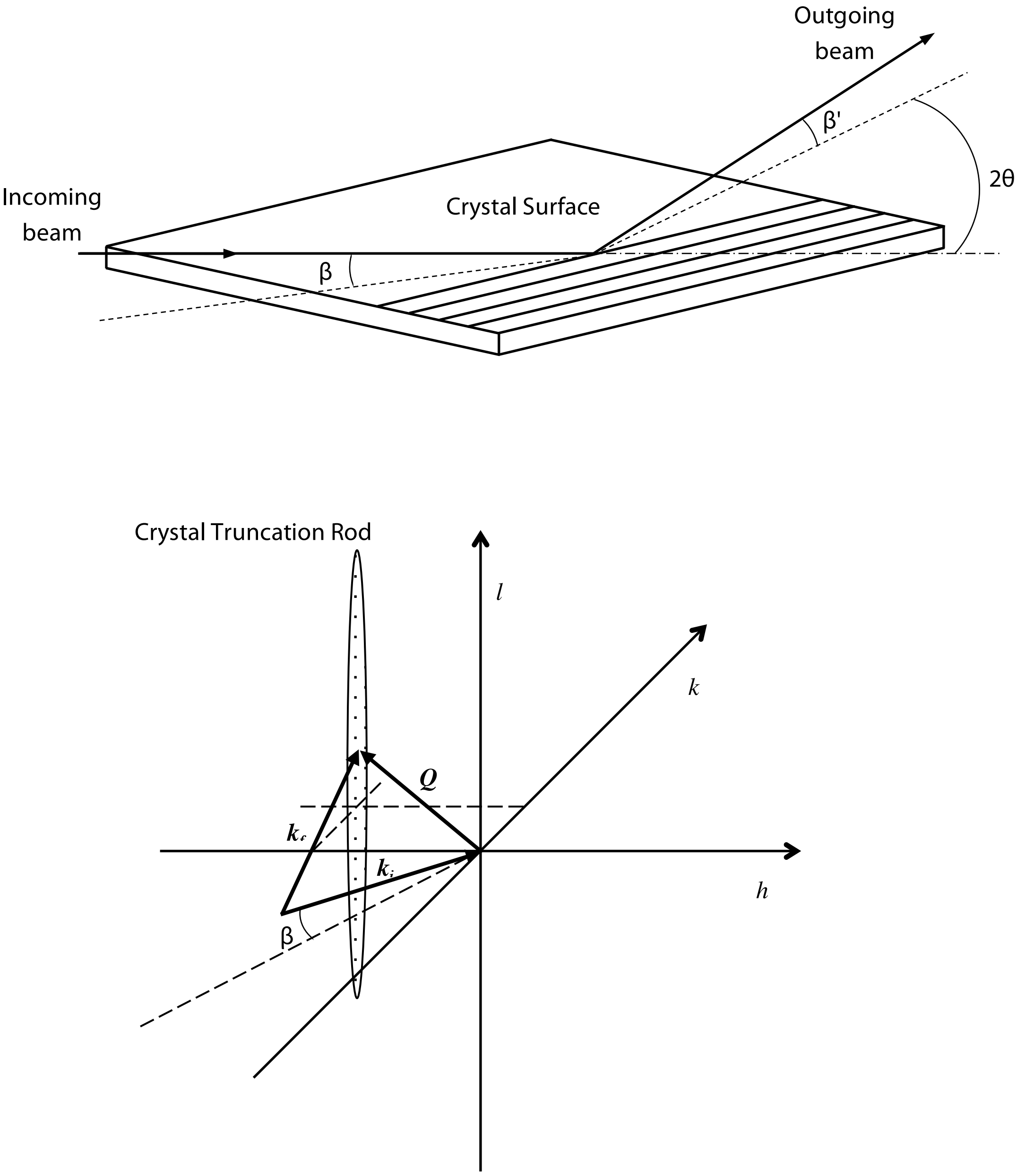

Figure 2.4: Schematic of the typical geometry for an SXRD experiment in real space (top) and reciprocal space (bottom). β is the angle of incidence, β' is the outgoing angle and 2θ is the projection of the scattering angle on to the surface. The 2D nature of surfaces is what gives rise to the crystal truncation rods in reciprocal space. Reproduced from [6].

2.2.2. SXRD Instrumentation

All of the SXRD data for this thesis were collected at the Surface and Interface Diffraction (I07) beamline, located at the Diamond Light Source facility, UK. The following sections will include a discussion as to why synchrotron radiation is needed for SXRD experiments, a description of the I07 beamline and its components including details of the diffractometer and the portable UHV chamber used for measurements. Lastly X-ray detectors are discussed, and data collection and analysis methodology is presented.

2.2.2.1. Synchrotron Radiation

A high intensity X-ray source is essential to the success of any SXRD experiment, primarily because the intensity of X-rays scattered from a surface will typically be ~10^5 times smaller than that scattering from the bulk [13]. Synchrotron sources provide high intensity radiation over a broad spectrum of wavelengths, ranging from infrared ($\lambda = 1\ \mu m$) to hard X-rays ($\lambda = 0.1\ nm$) [14]. Synchrotron radiation, the electromagnetic radiation generated by relativistic electrons (i.e. electrons traveling at speed of light or a significant proportion of) travelling in curved paths, is a highly collimated photon beam which is 10^{12} times brighter than most powerful lab sources [7], with well defined linear and circular polarization properties. The reader is referred to [6, 7, 15] for a detailed description of synchrotron radiation.

At a typical synchrotron radiation facility electrons, generated by thermionic emissions from an electron gun and then caused to bunch up using an alternating electric field to form a beam, are accelerated by a synchrotron to almost the speed of light using linear accelerators. These electrons are then injected into a storage ring, in which the charged particles circulate (using a system of bending and focusing magnets to tailor their path), producing synchrotron radiation. The synchrotron radiation beam is projected at a tangent to the electron storage ring and captured by the beamlines [15]. Radio Frequency (RF) cavities are used replenish the energy emitted as synchrotron radiation, and thus maintain the electron beam circulating around the 'storage ring' at a specific energy. Figure 2.5 shows schematically the main components of a synchrotron as described above.

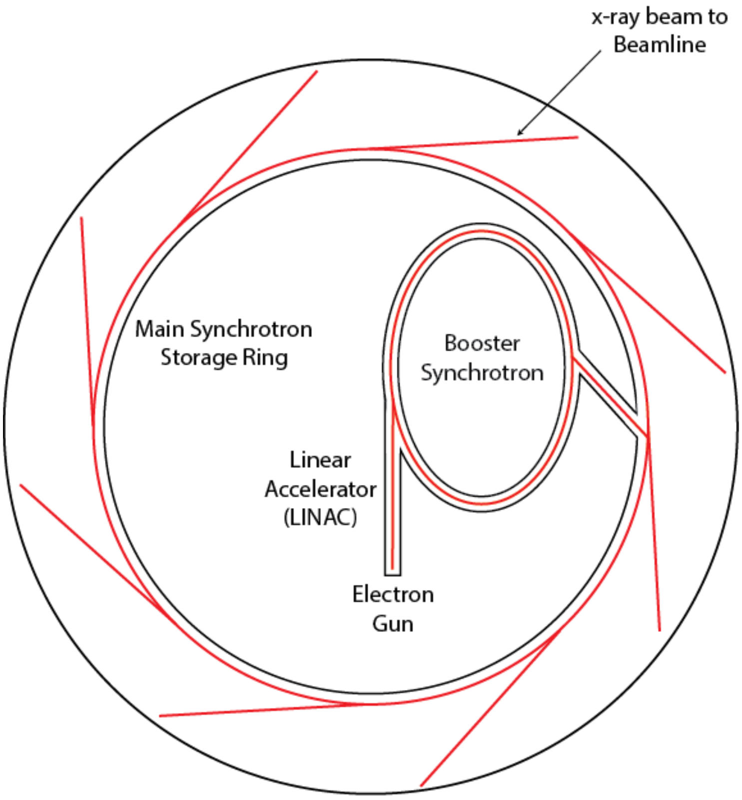

Figure 2.5: Schematic of the main components of a Synchrotron

Diamond is the UK's national purpose built third generation synchrotron radiation science facility, and was opened to its first users in February 2007. Operating at an electron energy of 3 GeV and a circulating current of 300 mA. Diamond is optimised to produce X-rays with energies ranging from 100 eV up to 30 keV [16]. Figure 2.6 shows an aerial view photograph of the Diamond Light Source.

At Diamond, a pre-injector linear accelerator (Linac) accelerates electrons to 100 MeV [17], and a booster synchrotron is used to increase the electron energy up to a final extraction energy of 3 GeV. The electrons are then injected into the ~560 m circumference storage ring consisting of twenty four straight sections connected together to form a closed loop. The synchrotron light emitted by the storage ring is transmitted to the beamlines.

Figure 2.6: Photograph of Diamond Light Source synchrotron radiation facility. Taken from [16]

2.2.2.2. Beamline and Experimental End-station

The Surface and Interface Diffraction beamline, I07, is a high-resolution X-ray diffraction beamline for investigating the structure of surfaces and interfaces under different environmental conditions, including harsh and real-world environments. I07 capabilities include surface X-ray diffraction (SXRD), X-ray reflectivity (XRR), grazing incidence X-ray diffraction (GIXRD) and grazing incidence small angle X-ray scattering (GISAXS) [16].

The beamline is setup such that it includes an optical hutch, two independently operating experimental hutches and a control room. Experimental hutch 1 (EH1) is equipped with a diffractometer of (2+3) geometry for *in situ* surface diffraction experiments with removable environmental chambers, including a small UHV ('baby') chamber for surface science studies. Experimental Hutch 2 (EH2) houses a UHV chamber with integral surface preparation/characterisation and deposition facilities mounted on a large, heavy-duty (2+3) circle diffractometer. The standard X-ray detector system used in both hutches is the 2-dimensional solid-state PILATUS II 100k detector, although other detectors are available, including a PILATUS 2M large area detector, a Cyberstar scintillation Point detector and an avalanche photodiode (APD) Point detector.

I07 utilizes a 2m long, in-vacuum cryo-cooled undulator to produce synchrotron radiation. The undulator produces a high flux of hard X-rays in the energy range 8-

30keV, which travels under near UHV conditions throughout the length of the beamline to the sample located in EH1/2. Wavelength selection is achieved using a pair of perfect Si(111) crystals in a cryo-cooled double-crystal monochromator (DCM), which is placed at 25.7m from the source. For all of the work presented in this study an X-ray beam energy of 17.7 keV (λ = 0.7 Å) was used. The monochromator is liquid nitogen cooled so as to counter the high heat load transferred from the white beam generated by the undulator. Beam focusing is achieved using a pair of Kirkpatrick Baez focusing mirrors [18] that independently focus the beam vertically and horizontally. The vertical focusing mirror is placed upstream of the horizontal focusing mirror at distances of 30m and 31.8m from the source, respectively. The beamline is terminated by a set of horizontal and vertical slits that define the dimensions and angular divergence of the beam that is projected onto the sample. Table 2.1 gives a summary of the beamline details.

Table 2.1: I07 beamline details [16]

Beamline name	I07 - Surface and Interface Diffraction beamline at Diamond Light Source.
Source type	2 m long cryo-cooled undulator with 17.7 mm Magnet period. White beam size (theoretical): 122.9 μm (h) × 6.4 μm (v) Beam divergence (theoretical): 24.2 μrad (h) × 4.2 μrad (v)
Monochromator	Cryo-cooled Double-crystal monochromator with two Si-111 crystals.
Mirrors	Two Kirkpatrick Baez (Bimorph) focusing mirrors (one vertically focusing, one horizontally focusing). Beam size at sample position 210 μm (h) × 115 μm (v) FWHM.
Energy range	8 keV – 30 keV

For this current work only EH1 was used to collect *SXRD* data. The diffractometer, UHV environment and detector system used for this study are discussed in further detail in subsequent sections.

2.2.2.3. Diffractometer

The design of a diffractometer for surface diffraction experiments needs to allow for accurate control of the incoming and outgoing angles. Consequently, many diffractometer types of varying geometries have been designed and are in use that fulfill these requirements, including z- axis [19], 6-circle [20], 5-circle [21] and (2+3) circle [22]. An overview of the different types of diffractometers used for SXRD experiments and the relative advantages and disadvantages of each is given by Bunk and Neilsen [23].

SXRD data acquired for this study was performed using the computer-controlled diffractometer of the (2+3) geometry located in EH1, a photograph of the diffractometer is shown in Figure 2.7.

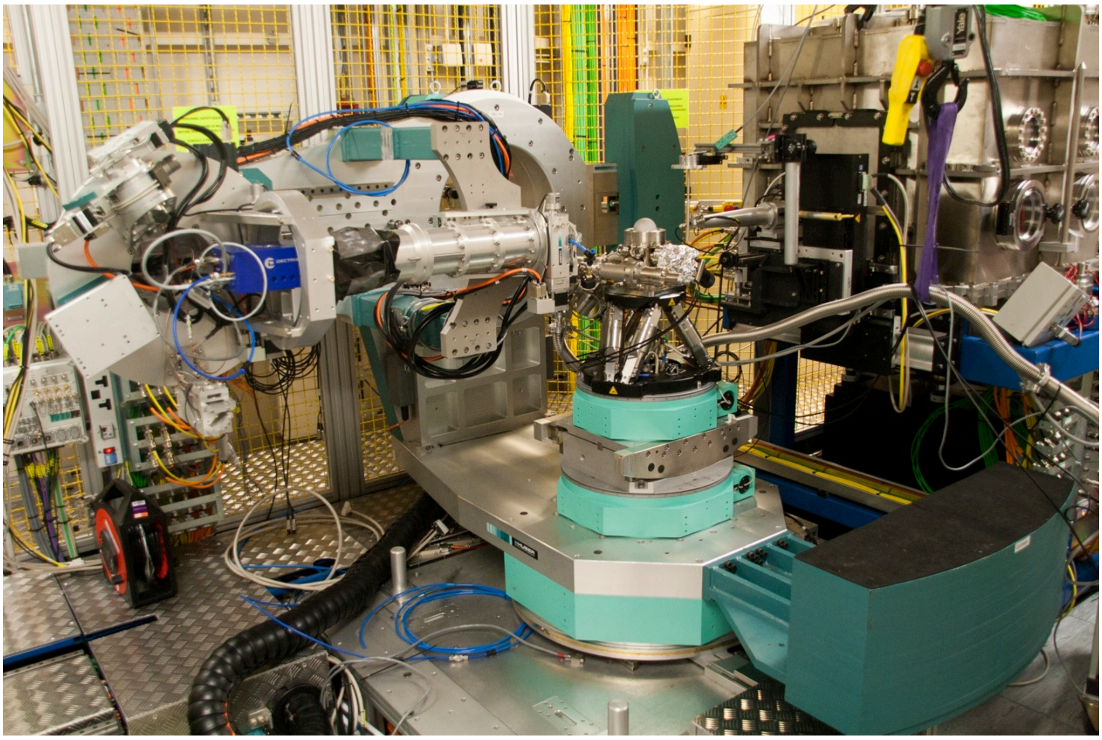

Figure 2.7: Photograph of the I07 EH1 (2+3) diffractometer with a hexapod and baby chamber mounted, employing a horizontal sample configuration. Also shown is the PILATUS 100K *X-ray* detector and flight tube mounted on the δ arm of the diffractometer.

A (2+3) circle diffractometer provides two degrees of freedom for the sample motion and three degrees of freedom for the detector motion. The addition of a hexapod mounted either vertically or horizontally allows the flexibility of mounting the sample either in a vertical or horizontal scattering geometry, as well providing six additional degrees of freedom – three translational and three rotational. The use of the hexapod also allows flexibility in the exact positioning of the sample, a position that is no longer dictated by the rotation centre of conventional circles. All the data presented in Chapters 4 and 5 were collected with the sample mounted horizontally such that the sample surface plane is horizontal, and the surface normal points upwards. Figure 2.8 shows a schematic of a (2+3) circle diffractometer, the naming convention for the instrument circles follow those used at the I07 beamline and are as per those used by Vlieg [22]. The detector circles δ and γ are used to position the detector in the direction of the diffracted beam whilst ν allows rotation of the detector around this direction. With the hexapod in the 'horizontal geometry' the grazing incidence angle of the incoming *X-ray* beam onto the sample is the ω circle, for this work the incidence angle of the X-ray beam was fixed at 1°. The sample circle φ is used to provide rotation around the surface normal.

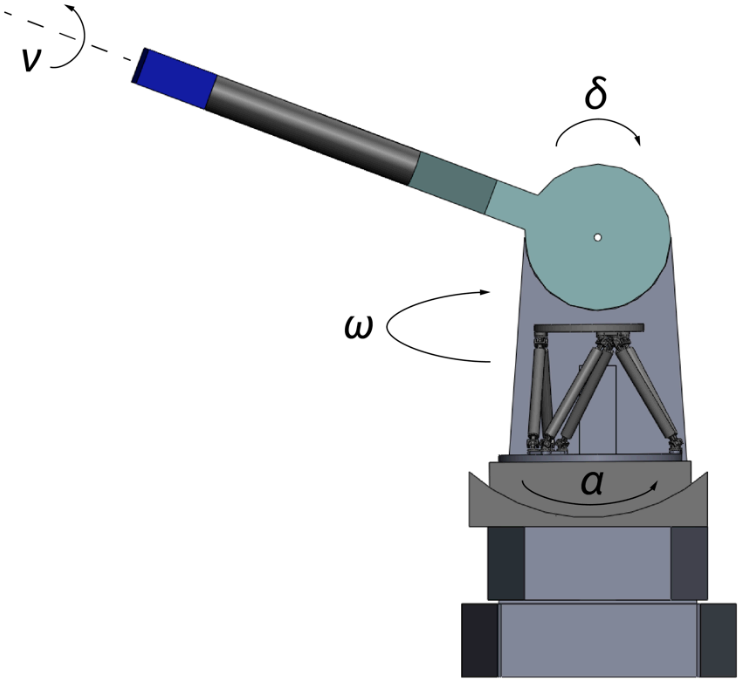

Figure 2.8: Schematic of a (2+3) circle diffractometer, the naming convention for the instrument circles follow those used at the I07 beamline at Diamond and are as per those used by Vlieg [22].

All the diffractometer movements are controlled by a *Linux* workstation running the *Generic Data Acquisition (GDA) software* [24]. GDA is an open source program designed to control synchrotron experiments and collect data developed by the *Data Acquisition and Scientific Computing Group* at *Diamond*.

2.2.2.4. Ultra High Vacuum (UHV) Instrumentation

SXRD requires a combination of an accurate diffractometer and often a surface science UHV environment, achievement of which is certainly not a trivial task. Over the years various solutions have been proposed, of these, two obvious solutions have been the most widely adopted for collecting SXRD measurements. The first of these is to reduce the size of the vacuum chamber and ensure that the diffractometer is able to carry the load. Here the sample is kept fixed inside the chamber and the entire chamber is rotated by the diffractometer. The second is to keep the UHV chamber, with integral surface preparation/characterisation and deposition equipment, fixed and allow for the rotary motion of the sample inside the chamber through a series of bellows and sliding seals. Various chamber designs have been reviewed in some detail by Feidenhans’l [3].

The first of these two approaches is employed for the SXRD experiments performed as part of this thesis. The sample is contained with in a small portable UHV transfer chamber (‘Baby chamber’) weighing approximately 50 kg with a hemispherical X-ray transparent beryllium (Be) window. Figure 2.9 shows an annotated photograph of a baby chamber. Beryllium is used as it allows the X-ray beam to enter and exit with little loss of intensity through absorption. A turbo pump is used to maintain the chamber at approximately UHV (typically 10^{-9} mbar or less).

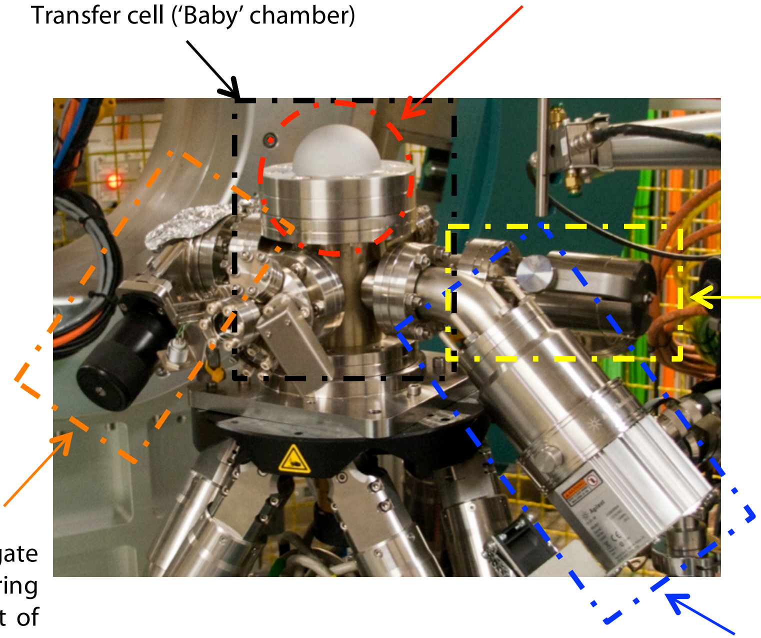

Figure 2.9: Annotated photograph of a ‘Baby’ chamber.

Sample transfer from the main off-line UHV preparation chamber into the portable UHV chamber, and visa versa, is a two-step procedure. First the sample must be transferred into a transfer chamber that can be connected and disconnected to and from the main UHV preparation chamber housed in the offline surface characterisation laboratory. Once transferred, the transfer chamber is disconnected from the offline UHV chamber and connected to the portable UHV 'baby' chamber via a T-connector with a turbo-molecular pump attached allowing pumping of the two cells. The sample can be inserted in (or out of) the 'baby chamber' by the transfer arm. The gate valve between the two chambers is then closed and the transfer chamber disconnected and the 'baby' chamber is left pumping on the turbo.

During *SXRD* data collection the baby chamber is mounted on the hexapod and kept in place by a series of mounting brackets, a photograph of which is shown in Figure 2.10.

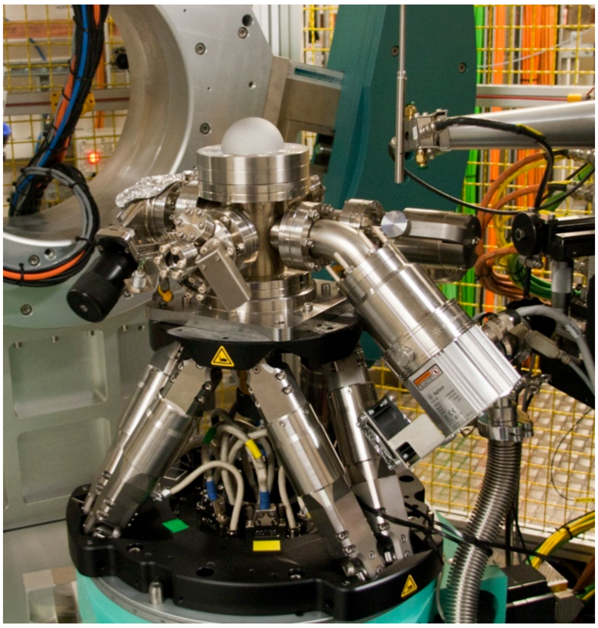

Figure 2.10: Picture showing the I07 beamline 'baby' chamber mounted on the hexapod.

2.2.2.5. X-ray Detector

SXRD experiments require a detection system with a high-count rate capability, high detection efficiency, a large dynamic range in order to process signals spanning several orders of magnitude in intensity, a fast readout time, high signal to noise ratio, and single photon counting capabilities; single photon counting capability results in a direct conversion from X-rays to counts and so reduces background noise and thus data quality is improved.

Until more recently SXRD experiments used point detectors as a means of collecting diffracted X-ray intensities. This is because they tend to be simple to operate, not very costly and are very light weight, thus reducing the load on the diffractometer arm and facilitating high-precision movements. Nevertheless it can not be ignored that it was ultimately the only technology available at the time. Collimating slits provide the means to adjust the detector's angular acceptance, thereby controlling the reciprocal space resolution. However, as it is a point detector each measurement provides one single intensity measurement, so it is necessary to scan either the detector position or the sample orientation for a given set of detector angles in order to record meaningful diffraction features, including the background signal in so-called 'rocking scans'. The development, in 1997, of a large area hybrid detector, the PILATUS (**Pi**xe**l** Appara**tu**s for the **S**wiss Light Source) detector, at the Paul Scherrer Institute (PSI) in collaboration with the Spring8 synchrotron radiation facility, has overcome the limitations of the point detectors [25]. To date PILATUS has several variations and the detector used to measure diffracted intensities in this thesis is the PILATUS 100K detector. The PILATUS 100K is an X-ray single photon counting silicon hybrid-pixel detector with an energy range of 3-30 keV.

At I07 the detector is mounted on the diffractometer 'δ' arm, refer to Figure 2.8, at the end of a flight tube typically at a distance 1 meter from the center of the diffractometer, with the detector center along the nu (ν)-rotation axis. The detector can, however, be shifted laterally both up/down and sideways using positioning screws on the detector holding bracket.

2.2.2.6. Sample Alignment and Data Collection

Sample alignment procedure involves several steps. Firstly the entire diffractometer is aligned such that its centre lies in the path of the incoming X-ray beam, which typically involves adjustment of the diffractometer's lateral position, height and tilt. Once accomplished, the next step is to zero the detector and sample motors. The final step is the alignment of the sample surface, both the physical surface and crystallographic (orientation matrix, UB). The former involves aligning the surface normal along the axis of the diffractometer.

Surface diffraction measurements are carried out at very small incident beam angles with respect to the sample surface, ideally below the critical angle for total external reflection (typically 1° or less). Such a grazing incidence angle is used so as to avoid too much background scattering from the bulk crystal.

In this thesis two types of scans have been used to collect data; namely rocking scans and l (or Rod) scans [26]. In a rocking scan the sample is rotated about its surface normal while scattered X-ray intensities are measured by orientating the sample and detector in the direction where the diffraction rod cuts the Ewald sphere to fulfil the (h, k, l) diffraction condition, diffracted intensity for a selected (h, k) are measured as a function of l. In the case of an l scans the detector is no longer fixed but rather moving through the range of l values, l_{start} to l_{End} and detector image of the intensity is taken; using an area detector the full range of the CTR's intersection with the Ewald sphere can be captured, a visual depiction of this is shown in Figure 2.11.

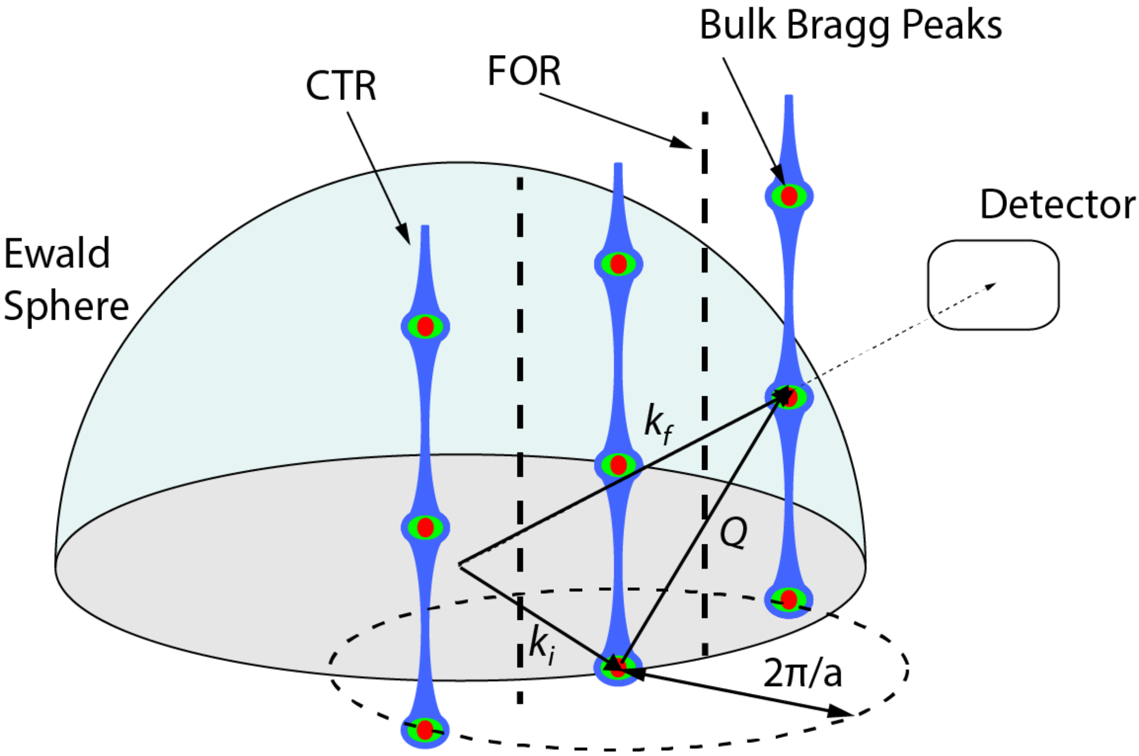

Figure 2.11: Representation of the Ewald sphere's relation to the reciprocal lattice, also depicted are the Crystal Truncation Rods (CTRs) and Fraction Order Rods (FORs). Diffraction conditions are only satisfied at the edge of the Ewald sphere.

2.2.3. Data Analysis

The road from experimental data to a structural solution involves two major data analysis steps. In the first instance structure factor amplitudes are calculated by extracting measured intensity data from the PILATUS images collected during the experimental beamtime, and applying the appropriate correction factors. Analysis of the data proceeds by comparison of the corrected experimental structure factors with generated simulated SXRD data for a potential structural solution. The corrections applied depend on the experimental geometry and the surface diffractometer used. Through iterative refinement of the geometry of this structure the best fit between experiment and theory may be reached. The latter of these steps is performed using ROD [27] a C-program written by Elias Vlieg for surface structure refinement on the basis of SXRD data. However, in the case of the former the use of 2D area X-ray detectors, in this particular case a PILATUS 100K area detector, for collecting scattered X-ray intensities as opposed to previous used point detectors has lead to many recent modifications in the procedure by which data is extracted and corrected. Consequently meaning the addition of important steps to the previously employed analysis procedure [28]. The first and most tasking of the data analysis steps is extracting meaningful X-ray intensity information from a detector image, indeed the main difficulty lies in correctly distinguishing between real signal and background noise. The rejection of surplus intensities measured by the area detector such as noise and Bragg peaks that passes close to the desired CTR depends very much on the selection of an appropriate 'region of interest (ROI)' containing the diffraction signal. Figure 2.12 show an annotated PILATUS image with the CTR close to a bragg peak, in this case extra care must be taken; in choosing a ROI that encloses and contains the diffracted signal as tightly as possible without cutting into it and compromising intensity signal, and whilst tracking the CTR to ensure that only the intensity from the CTR is extracted as they overlap. The shape, position, and orientation of a diffracted signal as seen in the PILATUS image may change considerably within a single *l* scan [29].

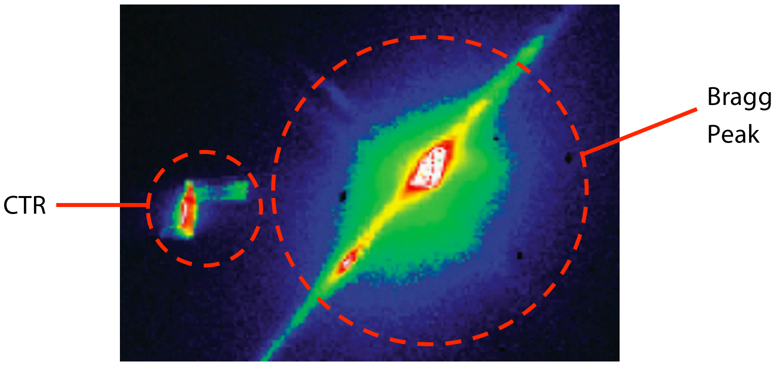

Figure 2.12: An annotated PILATUS image of a CTR in the vicinity of a Bragg peak [29].

To date researchers have developed their own analysis routines and procedures to facilitate the extraction and analysis of intensity images recorded using pixel area detectors. These have typically been written in programs such as MATLAB® (The MathWorks Inc., Natick, Massachusetts, USA) and IGOR Pro (Wavemetrics, Lake Oswego, OR, USA). All the work presented within the framework of this study has used a macro for intensity extraction written by J. Treacy in IGOR Pro. This program converts the experimentally collected scattered X-ray intensities to structure factors by integrating and applying the necessary corrections through facilitating ROI-based extraction of integrated intensities from the detector images including background subtraction.

The background signal is accounted for and subtracted from the overall intensity of the CTR in this extraction macro by considering a background ROI surrounding the primary ROI as shown in Figure 2.13 from which the background component is calculated by considering the counts within the background ROI. Figure 2.14 shows stepwise the extraction a CTR from a series of PILATUS images, only images at key values in l along the CTR are displayed in this illustrative representation as in reality there may be hundreds of images (depending on the number of data points) taken per rod.

Once the diffracted intensities have been extracted and integrated, it is necessary to apply several geometrical correction factors to the data convert the measured integrated intensities into Structure Factors before the data can be exported into ROD and any quantitative analysis begins.

$$F_{h,k,l} = Scaling\ Factor \times \sqrt{I_{int} \times \frac{P\ L\ C_{Int}}{C_{area}\ C_{beam}}} \tag{2.41}$$

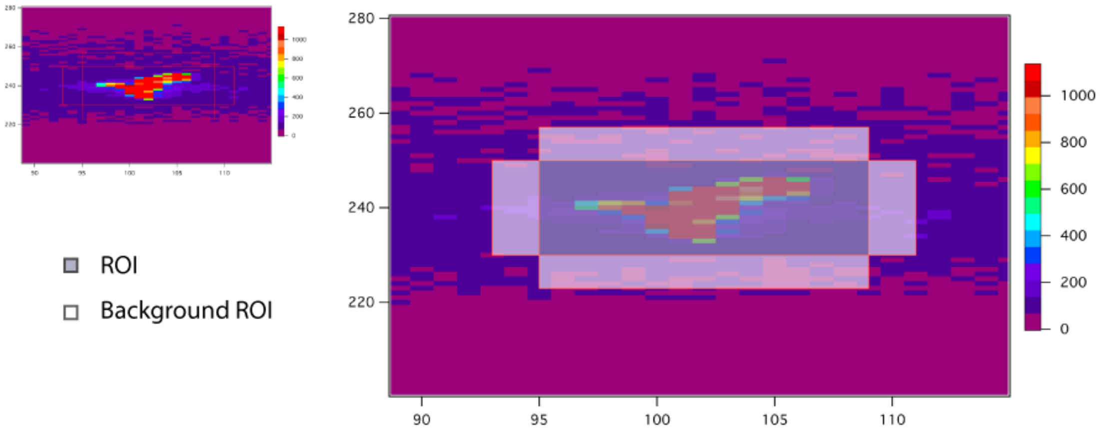

Figure 2.13: PILATUS image of scattered X-ray intensity (top left) as seen in the Igor PRO extraction macro. (right) Highlighted is the primary ROI and background-ROI.

I_{int} describes the measured integrated intensity, P is the polarisation factor, L is the Lorentz factor, C_{Int} the rod interception correction factor, C_{area} determines the variation in the active sample area, and C_{beam} is the correction factor for the beam profile. The scaling factor is usually an arbitrary constant, of say 100, applied to all corrected intensity values in order to make the data more workable in the case where the corrected intensities take small or very close to zero values i.e. less than unity. All these corrections are applied and accounted for within the extraction macro. The reader is referred to the paper by Vlieg [22] for a detailed derivation of the correction factors for a (2+3) diffractometer.

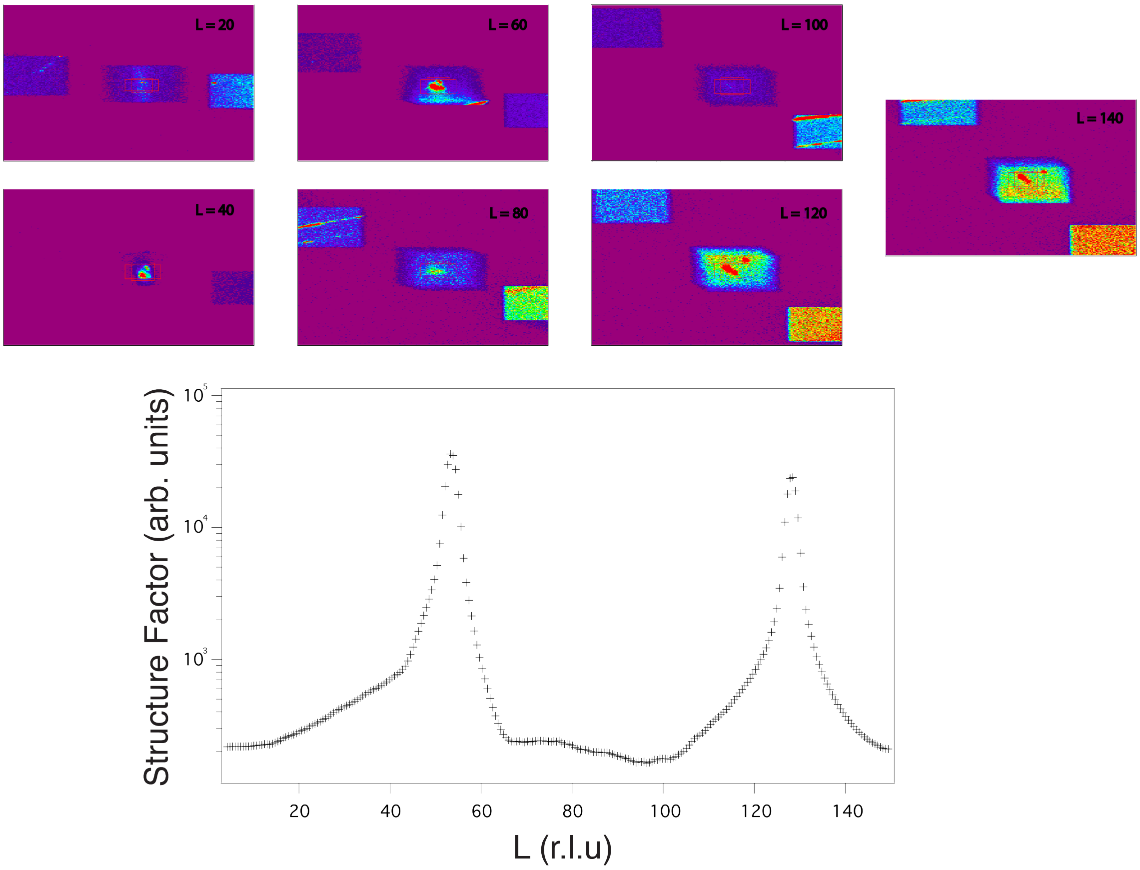

Figure 2.14: The stepwise extraction of a CTR from a series of PILATUS images. Images at key locations in *l* only are shown (namely *l*= 20, 40, 60, 80, 100, 120 and 140).

2.2.3.1. Experimental Errors and Uncertainties

For a given calculated structure factor, the associated uncertainty arises from the statistical uncertainty due to errors coming from counting statistics, $\sigma_{i,stat}$, and the systematic uncertainties, ε. These errors have to be estimated for structure factors calculated both by directly integrating data acquired stationary mode measurements and by integrating cross-sectional images generated from a rocking scan. As given by Robinson [6] the statistical error for a linear background is:

$$\sigma_{i,stat} = \left(I_{i,s} + \frac{N_{i,s}}{N_{i,B}} I_{i,B} \right) \tag{2.42}$$

Where $I_{i,s}$ is the integrated measured intensity within the region of interest (ROI), $N_{i,s}$ is the number of data points (in pixel counts) in the ROI, $N_{i,B}$ is the number of data points used for background estimation (Background ROI) and $I_{i,B}$ is the integrated background intensity of these points.

In order to minimise the associated experimental errors and improve the quality of a dataset $\{I_{hk}\}$ symmetry equivalent reflections and repeat measurements of as many reflections as possible are often performed. The level of agreement between these symmetry equivalent reflections or repeat measurements is a measure of the systematic errors in the dataset arising from small misalignments, precision of motor positions, sampling over different areas of the surface, etc. the systemic error, ε, is taken as a fixed proportion of the measured integrated intensity, typically this is in the region of 10%. Often due to experimental time limitations or surface symmetry constraints the number of equivalent reflections sampled is too small for their standard deviation to be an accurate measure of the of the error, and so as proposed by Vlieg [6] the square sum of the weighted statistical error of the available equivalent reflections $(j_1, j_2, \dots, j_n)$, $\sigma_{j,stat}$,and the overall systematic error, ε, is often used as a good estimation of the experimental uncertainty:

$$\sigma_j = \left(\sigma_{j,stat}^2 + \varepsilon^2\right)^{\frac{1}{2}} \tag{2.43}$$

2.2.3.2. Structure Determination - ROD

Once the data have been integrated, corrected and structure factors calculated the next step is to solve for a structural solution. However, as the structure factor is a Fourier transform of the spatial distribution of electron density, it is not possible to just simply determine the surface structure by calculating the inverse Fourier transform. This is as a result of the fact that during X-ray diffraction experiment only the intensity of the scattered wave is measured directly and thus the lack of the phase information makes it very difficult to recover the atomic-scale structure by direct inversion of the measured amplitudes, this is known as the 'Phase Problem'. Despite this apparent lack of phase information, atomic structures are regularly solved using SXRD conventionally through a trial-and-error method. Determination proceeds with an educated 'guess' for a trial model from which simulated structure factors can be compared with the experimental data. Through refinement a model giving the best fit of experimental data with simulated data is pursued. Figure 2.15 shows a schematic of the iterative optimisation of surface geometries to find and overall best fit between theory and experiment.

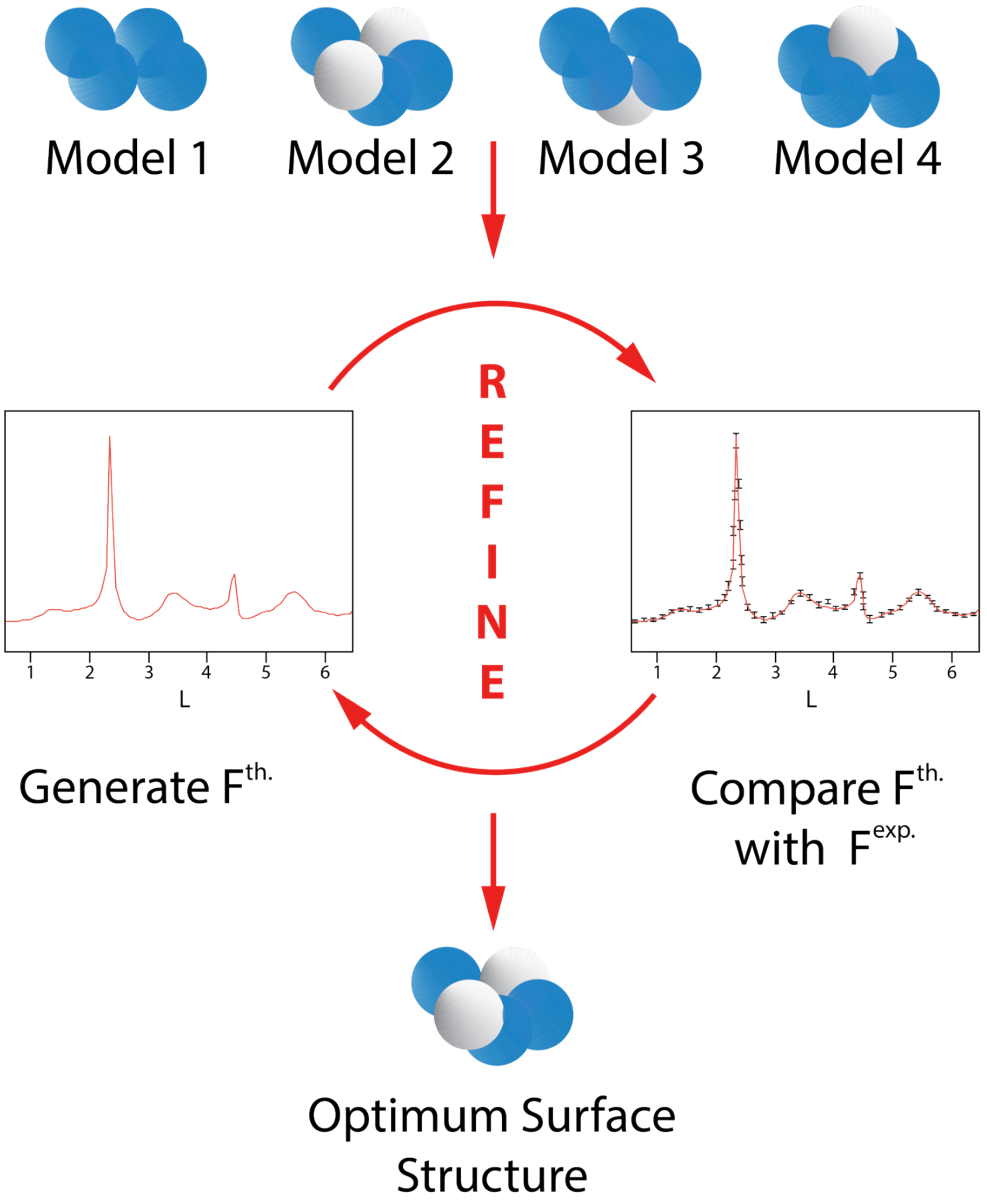

Figure 2.15: Schematic of the optimisation of surface geometries to find and overall best fit between theory and experiment through the iterative refinement of different models.

The 'goodness' of the fit is analysed in the model refinement software ROD using an optimisation of the structure model parameters using a χ^2 least squares minimisation employing the Levenberg-Marquard algorithm [30]. It should be noted that the simulated SXRD data is generated within and by ROD. χ^2, or strictly speaking the normalized/reduced χ^2, is calculated for each model and is defined by:

$$\chi^2 = \frac{1}{\sqrt{N-p}}\,\Sigma\left(\frac{\left|F^{exp}_{h,k,l}\right|^2 - \left|F^{th}_{h,k,l}\right|^2}{\sigma_{h,k,l}}\right)^2 \tag{2.44}$$

Where N is the number of measured structure factors, p is the number of independent parameters optimized during the fitting process, $F^{exp}_{h,k,l}$ are the experimentally measured structure factors, $F^{th}_{h,k,l}$ are the theoretically calculated structure factors, and $\sigma_{h,k,l}$ corresponds to the experimental uncertainties i.e. associated with $F^{th}_{h,k,l}$.

A χ^2 value ~1 is taken as an empirically validated indication of a good agreement between the experiment and simulated structure i.e. the ideal structure is taken as the one that minimises this measure of discrepancy, since the difference between experiment and simulated data should be equal to the error in the data $\sigma_{h,k,l}$. The agreement decreases with increasing χ^2 and a χ^2 of less than 1 suggests that the uncertainty in the experimental data has been over estimated.

ROD uses a command-line interpreter for interactive work and in order to do a structure refinement various types of input files need to be read into the program. These are the data file (default extension .dat), the bulk model file (default extension .bul) and the fit model file (default extension .par). The format of these files must be ASCII and can be generated in any standard text editor.

The data file contains the experimentally generated corrected data in a list including the diffraction indices (*hkl*), structure factors and the standard error on the structure factor. An example of a data file is shown in Figure 2.16 and the file takes the following format:

First line: Comments e.g. filename

Other lines: h k l F_{data} σ

The bulk model file contains information about the coordinates of the atoms in the bulk unit cell. The bulk model file takes the following structure:

First line: Comments e.g. filename

Second line: **a** **b** **c** α β γ (*lattice parameters*)

Other lines: A x y z N_{DW}

A denotes the standard chemical symbol given for each element, (x, y, z) give the position of each atom and should be given in fractional coordinates, N_{DW} is the serial number for the Debye-Waller for each respective atom, Figure 2.17 shows an example of a bulk file.

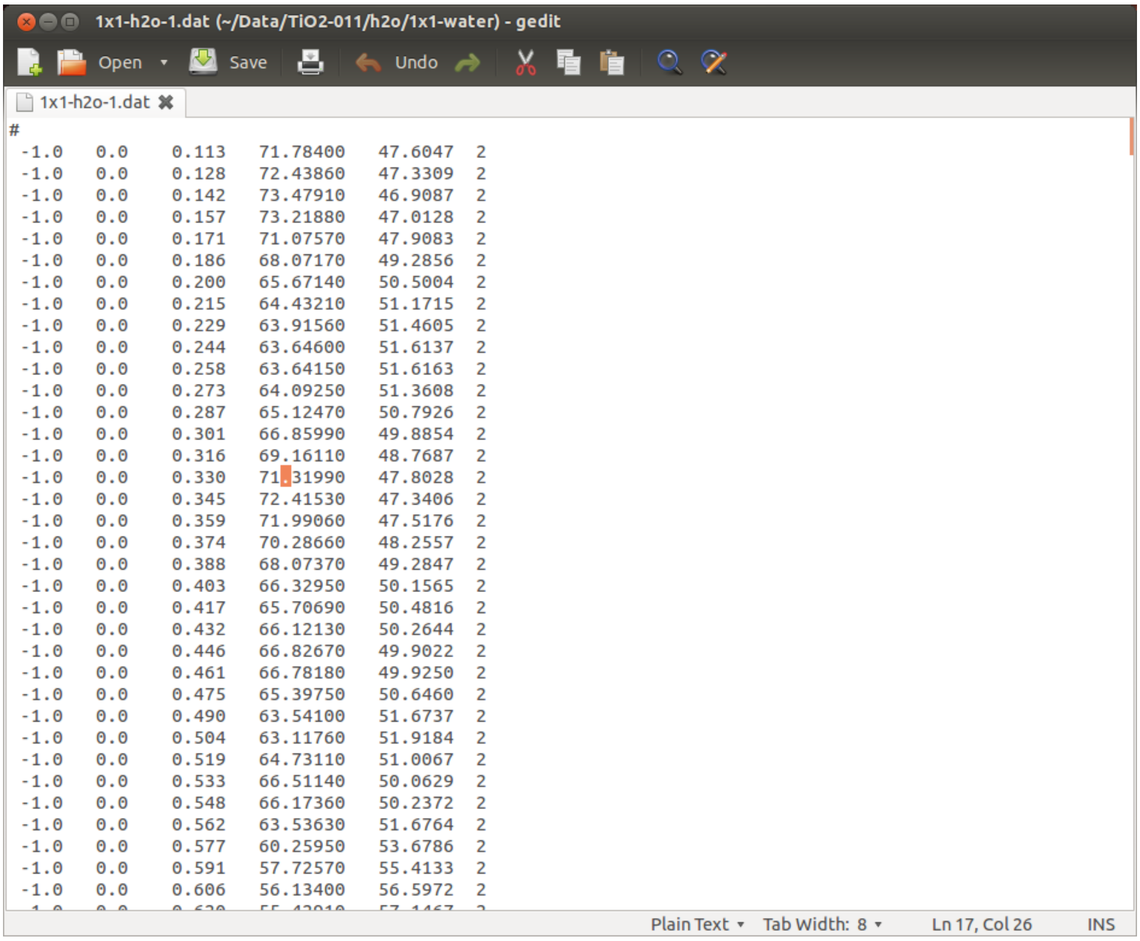

```
#
 -1.0   0.0    0.113   71.78400   47.6047  2
 -1.0   0.0    0.128   72.43860   47.3309  2
 -1.0   0.0    0.142   73.47910   46.9087  2
 -1.0   0.0    0.157   73.21880   47.0128  2
 -1.0   0.0    0.171   71.07570   47.9083  2
 -1.0   0.0    0.186   68.07170   49.2856  2
 -1.0   0.0    0.200   65.67140   50.5004  2
 -1.0   0.0    0.215   64.43210   51.1715  2
 -1.0   0.0    0.229   63.91560   51.4605  2
 -1.0   0.0    0.244   63.64600   51.6137  2
 -1.0   0.0    0.258   63.64150   51.6163  2
 -1.0   0.0    0.273   64.09250   51.3608  2
 -1.0   0.0    0.287   65.12470   50.7926  2
 -1.0   0.0    0.301   66.85990   49.8854  2
 -1.0   0.0    0.316   69.16110   48.7687  2
 -1.0   0.0    0.330   71.31990   47.8028  2
 -1.0   0.0    0.345   72.41530   47.3406  2
 -1.0   0.0    0.359   71.99060   47.5176  2
 -1.0   0.0    0.374   70.28660   48.2557  2
 -1.0   0.0    0.388   68.07370   49.2847  2
 -1.0   0.0    0.403   66.32950   50.1565  2
 -1.0   0.0    0.417   65.70690   50.4816  2
 -1.0   0.0    0.432   66.12130   50.2644  2
 -1.0   0.0    0.446   66.82670   49.9022  2
 -1.0   0.0    0.461   66.78180   49.9250  2
 -1.0   0.0    0.475   65.39750   50.6460  2
 -1.0   0.0    0.490   63.54100   51.6737  2
 -1.0   0.0    0.504   63.11760   51.9184  2
 -1.0   0.0    0.519   64.73110   51.0067  2
 -1.0   0.0    0.533   66.51140   50.0629  2
 -1.0   0.0    0.548   66.17360   50.2372  2
 -1.0   0.0    0.562   63.53630   51.6764  2
 -1.0   0.0    0.577   60.25950   53.6786  2
 -1.0   0.0    0.591   57.72570   55.4133  2
 -1.0   0.0    0.606   56.13400   56.5972  2
```

Figure 2.16: Example data file.

The fit file contains a trial model, which is to be used in the refinement. The fit model file takes the following format:

First line: Comments e.g. filename

Second line: **a** **b** **c** α β γ (*lattice parameters*)

Other lines:

A x_{Bulk} C_{x1} N_δ C_{x2} N_δ y_{Bulk} C_{y1} N_δ C_{y2} N_δ z_{Bulk} N_δ N_{DW1} N_{DW2} N_{occ}

Where C represents a set of constants giving the magnitude of the displacement, N_δ are serial numbers of displacement parameters, N_{DW1} is the serial number of the in-plane Debye-Waller parameter, N_{DW2} is the serial number of the out-of-plane Debye-Waller parameter and N_{occ} is the serial number of the occupancy parameter. Figure 2.18 shows an example fit file from which a model structure maybe generated.

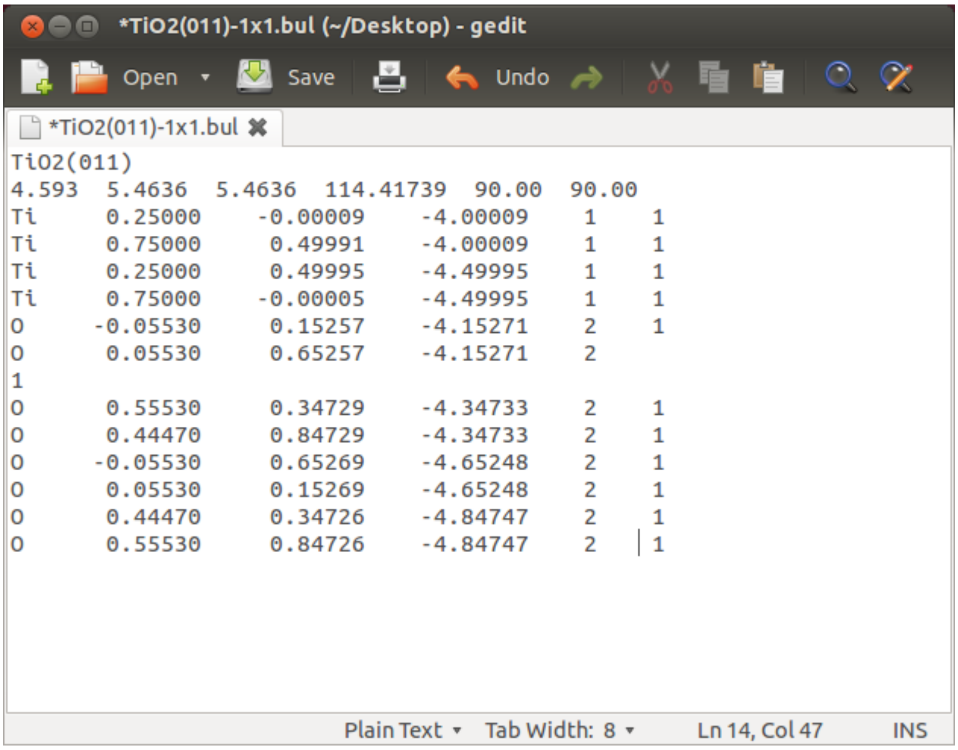

```
TiO2(011)
4.593  5.4636  5.4636  114.41739  90.00  90.00
Ti      0.25000     -0.00009     -4.00009     1     1
Ti      0.75000      0.49991     -4.00009     1     1
Ti      0.25000      0.49995     -4.49995     1     1
Ti      0.75000     -0.00005     -4.49995     1     1
O      -0.05530      0.15257     -4.15271     2     1
O       0.05530      0.65257     -4.15271     2
1
O       0.55530      0.34729     -4.34733     2     1
O       0.44470      0.84729     -4.34733     2     1
O      -0.05530      0.65269     -4.65248     2     1
O       0.05530      0.15269     -4.65248     2     1
O       0.44470      0.34726     -4.84747     2     1
O       0.55530      0.84726     -4.84747     2     1
```

Figure 2.17: Example bulk file.

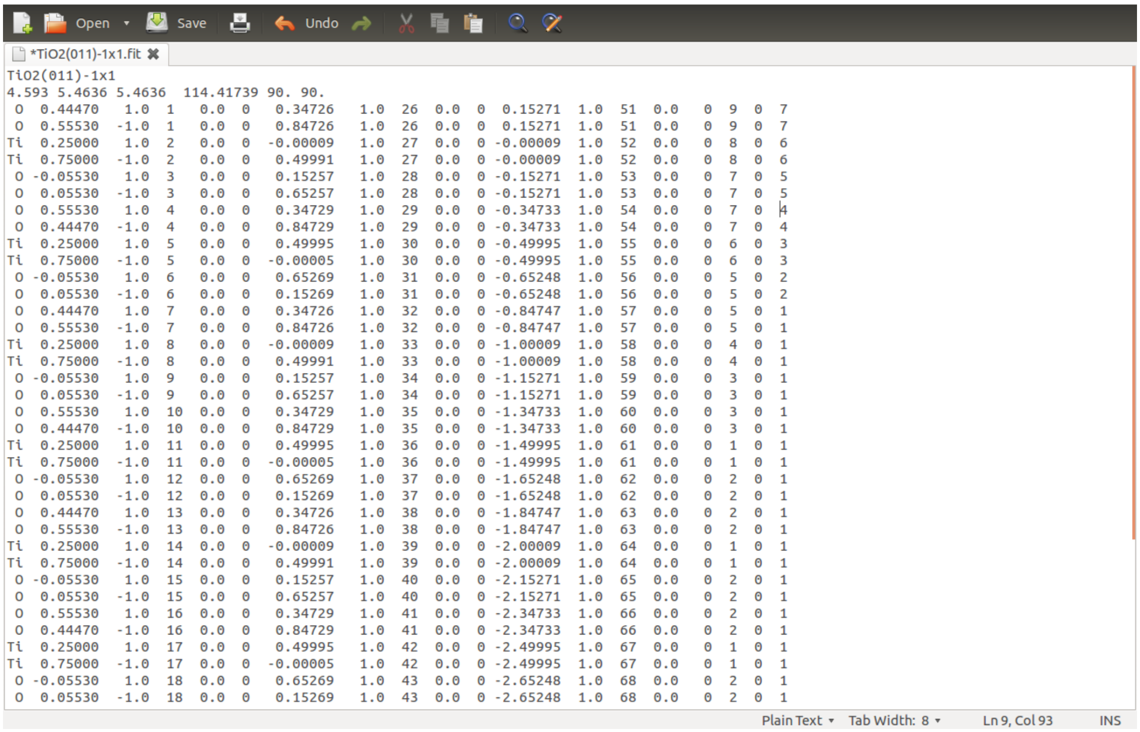

```
TiO2(011)-1x1
4.593 5.4636 5.4636  114.41739 90. 90.
 O  0.44470   1.0  1   0.0  0   0.34726   1.0  26  0.0  0  0.15271  1.0  51  0.0   0  9  0  7
 O  0.55530  -1.0  1   0.0  0   0.84726   1.0  26  0.0  0  0.15271  1.0  51  0.0   0  9  0  7
Ti  0.25000   1.0  2   0.0  0  -0.00009   1.0  27  0.0  0 -0.00009  1.0  52  0.0   0  8  0  6
Ti  0.75000  -1.0  2   0.0  0   0.49991   1.0  27  0.0  0 -0.00009  1.0  52  0.0   0  8  0  6
 O -0.05530   1.0  3   0.0  0   0.15257   1.0  28  0.0  0 -0.15271  1.0  53  0.0   0  7  0  5
 O  0.05530  -1.0  3   0.0  0   0.65257   1.0  28  0.0  0 -0.15271  1.0  53  0.0   0  7  0  5
 O  0.55530   1.0  4   0.0  0   0.34729   1.0  29  0.0  0 -0.34733  1.0  54  0.0   0  7  0  4
 O  0.44470  -1.0  4   0.0  0   0.84729   1.0  29  0.0  0 -0.34733  1.0  54  0.0   0  7  0  4
Ti  0.25000   1.0  5   0.0  0   0.49995   1.0  30  0.0  0 -0.49995  1.0  55  0.0   0  6  0  3
Ti  0.75000  -1.0  5   0.0  0  -0.00005   1.0  30  0.0  0 -0.49995  1.0  55  0.0   0  6  0  3
 O -0.05530   1.0  6   0.0  0   0.65269   1.0  31  0.0  0 -0.65248  1.0  56  0.0   0  5  0  2
 O  0.05530  -1.0  6   0.0  0   0.15269   1.0  31  0.0  0 -0.65248  1.0  56  0.0   0  5  0  2
 O  0.44470   1.0  7   0.0  0   0.34726   1.0  32  0.0  0 -0.84747  1.0  57  0.0   0  5  0  1
 O  0.55530  -1.0  7   0.0  0   0.84726   1.0  32  0.0  0 -0.84747  1.0  57  0.0   0  5  0  1
Ti  0.25000   1.0  8   0.0  0  -0.00009   1.0  33  0.0  0 -1.00009  1.0  58  0.0   0  4  0  1
Ti  0.75000  -1.0  8   0.0  0   0.49991   1.0  33  0.0  0 -1.00009  1.0  58  0.0   0  4  0  1
 O -0.05530   1.0  9   0.0  0   0.15257   1.0  34  0.0  0 -1.15271  1.0  59  0.0   0  3  0  1
 O  0.05530  -1.0  9   0.0  0   0.65257   1.0  34  0.0  0 -1.15271  1.0  59  0.0   0  3  0  1
 O  0.55530   1.0  10  0.0  0   0.34729   1.0  35  0.0  0 -1.34733  1.0  60  0.0   0  3  0  1
 O  0.44470  -1.0  10  0.0  0   0.84729   1.0  35  0.0  0 -1.34733  1.0  60  0.0   0  3  0  1
Ti  0.25000   1.0  11  0.0  0   0.49995   1.0  36  0.0  0 -1.49995  1.0  61  0.0   0  1  0  1
Ti  0.75000  -1.0  11  0.0  0  -0.00005   1.0  36  0.0  0 -1.49995  1.0  61  0.0   0  1  0  1
 O -0.05530   1.0  12  0.0  0   0.65269   1.0  37  0.0  0 -1.65248  1.0  62  0.0   0  2  0  1
 O  0.05530  -1.0  12  0.0  0   0.15269   1.0  37  0.0  0 -1.65248  1.0  62  0.0   0  2  0  1
 O  0.44470   1.0  13  0.0  0   0.34726   1.0  38  0.0  0 -1.84747  1.0  63  0.0   0  2  0  1
 O  0.55530  -1.0  13  0.0  0   0.84726   1.0  38  0.0  0 -1.84747  1.0  63  0.0   0  2  0  1
Ti  0.25000   1.0  14  0.0  0  -0.00009   1.0  39  0.0  0 -2.00009  1.0  64  0.0   0  1  0  1
Ti  0.75000  -1.0  14  0.0  0   0.49991   1.0  39  0.0  0 -2.00009  1.0  64  0.0   0  1  0  1
 O -0.05530   1.0  15  0.0  0   0.15257   1.0  40  0.0  0 -2.15271  1.0  65  0.0   0  2  0  1
 O  0.05530  -1.0  15  0.0  0   0.65257   1.0  40  0.0  0 -2.15271  1.0  65  0.0   0  2  0  1
 O  0.55530   1.0  16  0.0  0   0.34729   1.0  41  0.0  0 -2.34733  1.0  66  0.0   0  2  0  1
 O  0.44470  -1.0  16  0.0  0   0.84729   1.0  41  0.0  0 -2.34733  1.0  66  0.0   0  2  0  1
Ti  0.25000   1.0  17  0.0  0   0.49995   1.0  42  0.0  0 -2.49995  1.0  67  0.0   0  1  0  1
Ti  0.75000  -1.0  17  0.0  0  -0.00005   1.0  42  0.0  0 -2.49995  1.0  67  0.0   0  1  0  1
 O -0.05530   1.0  18  0.0  0   0.65269   1.0  43  0.0  0 -2.65248  1.0  68  0.0   0  2  0  1
 O  0.05530  -1.0  18  0.0  0   0.15269   1.0  43  0.0  0 -2.65248  1.0  68  0.0   0  2  0  1
```

Figure 2.18: Example fit file.

When performing a structure refinement, ROD cyclically optimises individually the values of all variable parameters including position, vibrational amplitude (Debye-Waller factor) and occupancy of each of the surface atoms in the trial model. The cyclic refinement of the structure is stopped when a physically reasonable structure with χ^2 value as close as possible to 1 is achieved.

2.2.3.4. Error Calculation – Derived Parameters

For the Levenberg-Marquardt least squares minimisation employed in ROD there are two ways in which errors are estimated for the individual fitting parameters. The first of which is the covariance matrix. However this does take into account the correlation between parameters and derives an error corresponding to an increase in the non-normalised χ^2 of 1. If the normalised χ^2 value is larger than 1, the errors is be multiplied by the square root of the normalised χ^2 (the same is true when this value is smaller than 1). The second method used to estimate the errors in ROD is to find the true increase in χ^2 by doing full fits with all parameters free except the one for which the error is being estimated for, this is then repeated for all free parameters in a fit.

Table 2.2: Common functions and their derivatives used to calculate to bond length errors

$f(a)$	$f'(a)$	
$a = b + c$	$\delta(a) = \sqrt{(\delta b)^2 + (\delta b)^2}$	(2.45)
$a = b - c$		
$a = \lambda bc$	$\left(\frac{\delta a}{a}\right)^2 = \lambda\left[\left(\frac{\delta b}{b}\right)^2 + \left(\frac{\delta c}{c}\right)^2\right]$	(2.46)
$a = \lambda \frac{b}{c}$		
$a = \lambda b^{\mu}$	$\delta(a) = \mu\lambda b^{\mu-1}\delta b$	(2.47)

Often the surface structure solution is expressed as the displacement in (x, y, z) of each atom from the associated bulk lattice position. As mentioned above the atomic coordinate errors are deduced from the individual displacement parameter errors deduced from ROD, however when considering the errors in atomic bond lengths extra care needs to be taken. The bond length is often the best indication of the nature of adsorbed species and so is of critical importance. Below, the methodology for determining bond length errors is outlined, it is assumed the errors of the individual atomic coordinates is known and follows standard error propagation. Error propagation is the means by which the uncertainty in a calculated result is determined, since all measurements have an uncertainty, and thus the results of calculations made using these measurements must also have an uncertainty; Table 2.2 outlines the mathematical functions and their derivatives used in bond length error calculation.

Let $r(A-B)$ be the distance (bond length) between two atoms located at points $A=(x_1,y_1,z_1)$ and $B=(x_2,y_2,z_2)$ defined relative to a common origin, and let the associated error in atomic coordinates in A and B be represented by $(\delta x_1,\delta y_1,\delta z_1)$ and $(\delta x_2,\delta y_2,\delta z_2)$ respectively. $r(A-B)$ can be thus calculated from:

$$r(A-B)=\sqrt{(x_2-x_1)^2+(y_2-y_1)^2+(z_2-z_1)^2} \qquad (2.48)$$

Using the standard error propagation formula, Equation 2.45, the atomic displacement error for each axis is given as (example (x_2-x_1)):

$$\delta(x_2-x_1)=\sqrt{(\delta x_2)^2+(\delta x_1)^2} \qquad (2.49)$$

Thus calculating using $\delta(x_2-x_1)^2$ Equation 2.47:

$$\delta(x_2-x_1)^2=2(x_2-x_1)\sqrt{(\delta x_2)^2+(\delta x_1)^2} \qquad (2.50)$$

Similar expressions can be written for y and z axes, and thus the overall expression for the bond length error, $\delta r(A-B)$, is written as:

$$\delta r(A-B)=\frac{1}{2\cdot r(A-B)}\times\begin{Bmatrix}4(x_2-x_1)^2[(\delta x_2)^2+(\delta x_1)^2]+\\4(y_2-y_1)^2[(\delta y_2)^2+(\delta y_1)^2]+\\4(z_2-z_1)^2[(\delta z_2)^2+(\delta z_1)^2]\end{Bmatrix} \qquad (2.51)$$

2.3. UHV Techniques and Instrumentation

A number of UHV dependent experimental techniques were employed to achieve the objectives of this thesis. In the following sections the theoretical background, experimental practicalities and instrumentation are discussed. The UHV systems that house the instrumentation needed for such techniques are also described alongside an introduction into why a UHV environment is needed.

2.3.1. UHV Systems

A key requirement for studying atomically clean surfaces and for such surfaces to be maintained in a contamination-free state throughout the duration of the experiment is an Ultra High Vacuum (UHV) environment, this is commonly defined as a pressure of 1×10^{-9} mbar or lower [8]. The following calculation demonstrates why such low pressures are necessary. The concentration of atoms on the surface of a solid material is typically on the order of 1×10^{15} cm^{-2}. To keep the surface 'clean' for say, 1 hour (3600 s), the flux of molecules, assuming a unity sticking coefficient, incident on the initially clean surface resulting in monolayer coverage must naturally be less than 1×10^{12} molecules/cm^2/sec. From the kinetic theory of gases, the flux, F, of molecules incident on a surface of unit area at ambient pressure, P, is given by:

$$F = \frac{N_A P}{\sqrt{2\pi MRT}} = 3.51 \times 10^{22} \frac{P}{\sqrt{MT}}\ atoms/cm^2 \cdot sec \qquad (2.52)$$

where N_A is Avogadro's number, T is the temperature and M is the average molecular weight. Taking the example of H_2O, a common constituent in vacuum systems at low pressures [31], then $M = 18\ g/mole$ at room temperature, $T = 273\ K$, and assuming a sticking coefficient of unity the pressure required to maintain a clean surface for about 1 hour is $P = 2 \times 10^{-9}$ mbar. So at $P = 2 \times 10^{-9}$ it takes 1 hour to have monolayer coverage of H_2O on a 1 cm^2 surface. Although an approximation and for one specific case, such an estimate nevertheless demonstrates the need for UHV conditions in order to ensure that the time required for contaminant build-up on the clean sample surface is substantially greater than that required to conduct the experiment i.e. of the order of hours. The need for very good vacuum conditions in order to carry out reliable surface science experiments is clearly evident, in the following pages the vacuum systems used as part of this study are described and discussed in some detail.

Primarily two UHV systems have been used i.e. an Omicron UHV low temperature STM located in the Photon Science Institute (PSI), University of Manchester to collect the STM data found in chapter 6 and the VG Microtech Multilab with RHK variable temperature combined UHV STM/AFM located in the Williamson Research Centre, School of Earth and Atmospheric Sciences at the University of Manchester, to prepare the Cr_2O_3 crystals prior to SXRD experimentation at the synchrotron forming the basis of Chapter 4 and to collect the LEED and AES data presented in chapter 6.

Each of these two vacuum systems consists of a sample preparation chamber and STM chamber separated by a manual gate valve. In each system the isolation of the two chambers from each other by gate valve permits the higher pressures required for sample preparation in the preparation chamber without contaminating the STM chamber. A load-lock pumped by a turbo-molecular pump is found on both systems, facilitating for the introduction of samples into the UHV system without the need to break vacuum.

Following a bake out, typically at ~120°C for approximately 2-3 days, base pressures in the low 10^{-10} mbar regime are routinely obtained for both chambers. Baking the chambers permits for the removal of residual gas molecules that are adsorbed on the inner surfaces walls of the chamber preventing UHV pressure; these are predominantly H_2, CO_2 and H_2O.

2.3.1.1. Omicron UHV low temperature STM

Figure 2.19 shows a schematic view of the Omicron UHV low temperature STM vacuum system described below. The pressure in the chamber is monitored through a hot cathode ion gauge located in the center of the preparation chamber. The preparation chamber is equipped with an ion gun connected to an argon cylinder (scientific grade – 99.9999% purity) for samples to be sputtered by argon ion bombardment; samples are annealed by means of an electron beam filament heater. An ion gauge allows for the pressure to be monitored at all times. The STM side of the UHV chamber houses an Omicron low temperature STM capable of operation at sample temperatures ranging from room temperature down to 5 K (liquid helium temperature). However, all STM data presented here has been collected at room temperature. Precision leak valves on both sides of the chamber; namely preparation (for *ex situ* dosing) and STM (for *in situ* dosing), allow for the introduction of gases or liquid vapour through an inlet manifold.

The piezotube and thus STM tip are controlled by a commercial software program called Scala, which is integrated with a Matrix STM control unit from the Omicron.

Samples are mounted onto Omicron tantalum sample plates, Figure 2.20, and held in place with spot welded 0.15 mm thick tantalum strips. Samples with maximum dimensions of 10 × 10 mm^2 maybe mounted using this configuration. The plates are introduced via the load lock and placed on the heating stage manipulator. The manipulator allows lateral movement of the sample plate into the main preparation chamber. When mounted on the heating stage the sample plate may be heated by way of electron bombardment. The sample temperature during annealing cycles is monitored using a hand held optical IMPAC IGA 8 Pro pyrometer (LumaSense Technologies, Germany). A long magnetic transfer arm allows location of the sample within the preparation chamber, and transfer into the STM chamber. Sample plates are transferred between the transfer arm and STM stage with a pincer-grip 'wobble' stick.

Vacuum is maintained using a combination of pumps. The load lock and preparation chambers are pumped using a BOC Edwards EXT 255 H 250 l/s turbo-molecular pump backed by a BOC Edwards XDS 35i rotary/scroll pump. The turbo-molecular pump rapidly and easily handles the removal of a significant volume of gas from the system encountered when bringing the system down from atmospheric pressure and during high outgassing operations such as ion sputtering and annealing, and will bring the pressure down to ~10^{-8} mbar region. The preparation and STM chambers are maintained at UHV pressure by means of two 320 l/s ion pumps (one for the preparation chamber and one for STM chamber) and a titanium sublimation pump (TSP). During STM imaging vibration is minimised by employing only the ion pumps to maintain UHV pressures, all other sources of vibrational noise, namely turbo molecular pumps, backing pumps and cooling fans must be switched off in order to achieve atomic resolution imaging.

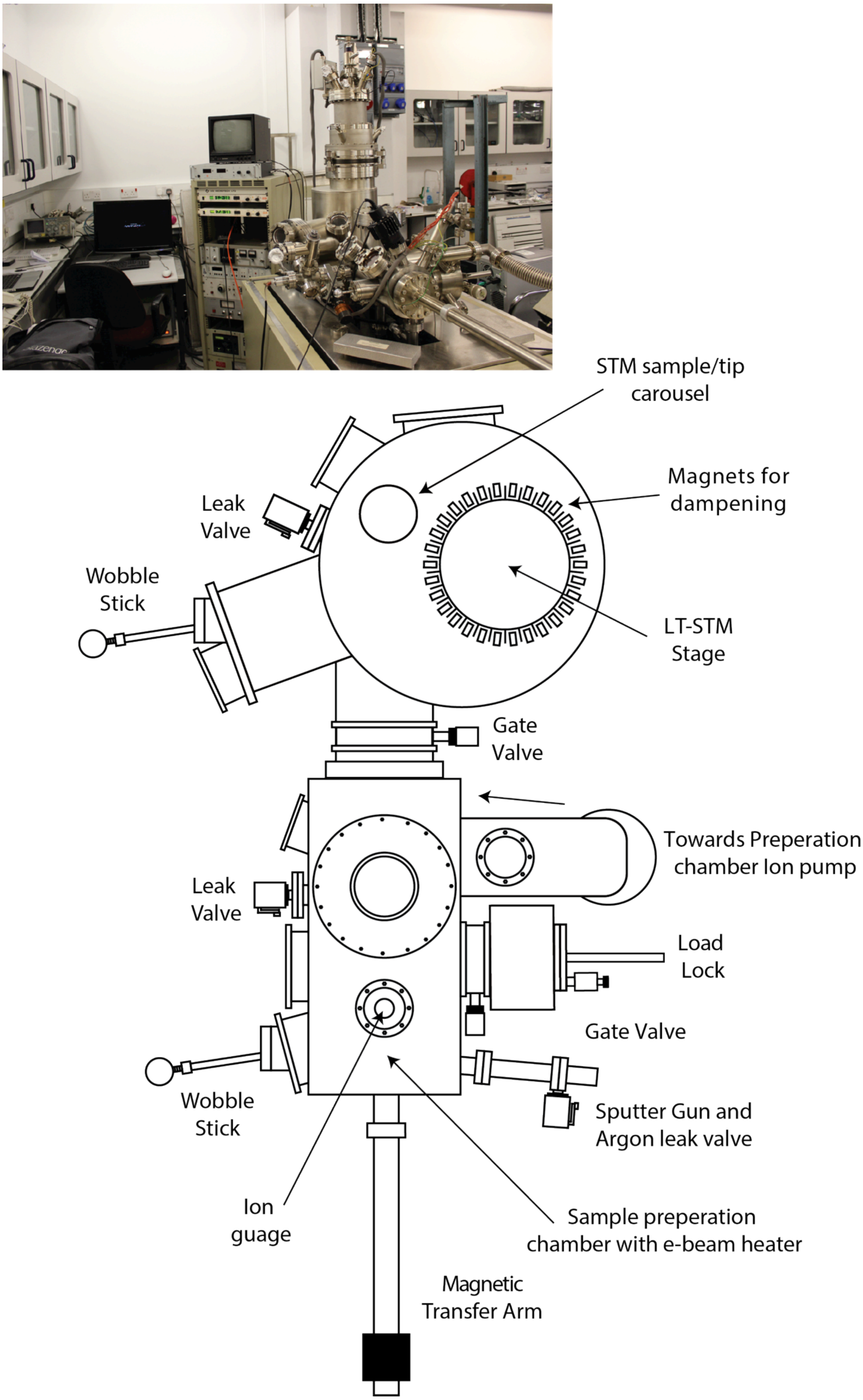

Figure 2.19: Schematic and photograph of the Omicron UHV low temperature STM

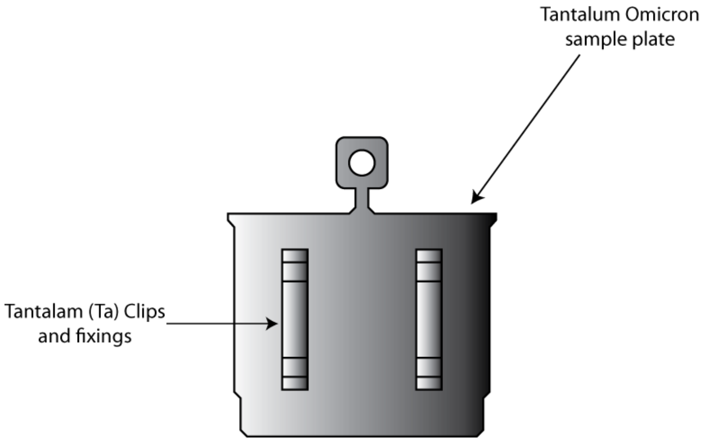

Figure 2.20: Illustration of the sample mount used in the Omicron Low Temperature STM.

2.3.1.2. VG Microtech Multilab with RHK Variable Temperature combined STM/AFM

The VG Microtech Multilab is a modular surface analysis instrument; the system consists of four main chambers, the preparation and analysis chamber, the load lock or fast entry air lock (FEAL) chamber, the RHK variable temperature combined UHV 300 VT STM/AFM and the sample-parking chamber connecting the other three chambers with gate valves to the FEAL and STM/AFM chambers. A schematic of the VG Mictrotech Multilab system is shown in Figure 2.21.

The sample preparation and analysis chamber is configured with an argon source for cleaning samples by argon ion bombardment; a quadropole mass spectrometer is used to check the purity of the argon used for sputtering as well as for leak checking the chamber using helium gas detection. Sample annealing is performed using an electron beam filament heater mounted on the manipulator stage. The chamber is also equipped with a reverse view *LEED* optics and hemispherical electron analyser for *AES* measurements. Several high precision leak valves are available for gas dosing.

The STM/AFM chamber is equipped with an RHK variable temperature combined UHV 300 VT STM/AFM capable of operation at sample temperatures ranging from 100 K up to 500 K. The STM scan head is based on the ''Walker type'' design [32, 33]. For a detailed description of the RHK UHV 300 VT STM/AFM the reader is referred to the user operating manual [34]. A sublimation system attached to the STM chamber allows the introduction of gas or vapor for *insitu* dosing via a high precision leak valve. The microscope is controlled by SPM 1000 electronics that are card interfaced to a data-acquisition computer, running RHK's data processing software SPM 32.

The entire UHV chamber is suspended on a Newport optical table with four Newport I-2000 High Performance Laminar Flow Isolators (air legs) providing pneumatic low frequency vibration isolation in the vertical direction combined with pendulum isolation in the horizontal plane. Viton loops supporting the STM stage coupled with the mass of the STM stage provides isolation against high frequency vibrations that maybe transmitted through the chamber.

Samples are mounted on an RHK sample carrier, consisting of a double grooved copper body and a helical molybdenum top ramp, each ramp has a height of 0.75 mm and covers an angle of 120°. An annotated schematic of the RHK sample carrier is shown in Figure 2.22. Disc type samples with a maximum diameter of 10 mm maybe mounted in between two sapphire washers and held in position by three leaf spring clips screwed into the ramps; other shaped samples maybe mounted so long as they fit within the 10 mm diameter sample opening. A tungsten filament (0.25 mm diameter wire) heater located on the manipulator stage underneath the sample holder is used to anneal samples by electron bombardment, temperatures in excess of 1273 K can be achieved; a built-in thermocouple allows measurement of the sample temperature.

For *insitu* sample transfer a wobble stick with a fork end is used to manipulate the sample holder. When transferring the sample holder the fork is inserted into the top groove of the sample holder body to manipulate them and permit exchange between various locations, the bottom groove is used by the fork on the long transfer arm fork or the sample stage fork. Sample transfer between chambers is achieved via the long magnetic transfer arm with a transfer fork at the end; the transfer folk holds the sample holder in place throughout the transfer procedure.

The preparation and analysis chamber and FEAL are pumped by a BOC Edwards EXT 250 H 250 l/s turbo pump, backed by a rotary pump. The sample-parking chamber is connected directly to the preparation and analysis chamber and so therefore also pumped by the same turbo pump. A 320 l/s ion pump and a titanium sublimation pump (TSP) pump the STM/AFM chamber. During sample transfer in and out of the UHV system the gate valve separating the preparation, analysis chamber and the sample-parking chamber from the STM/AFM chamber is opened so that the ion pump and TSP pump all three chambers.

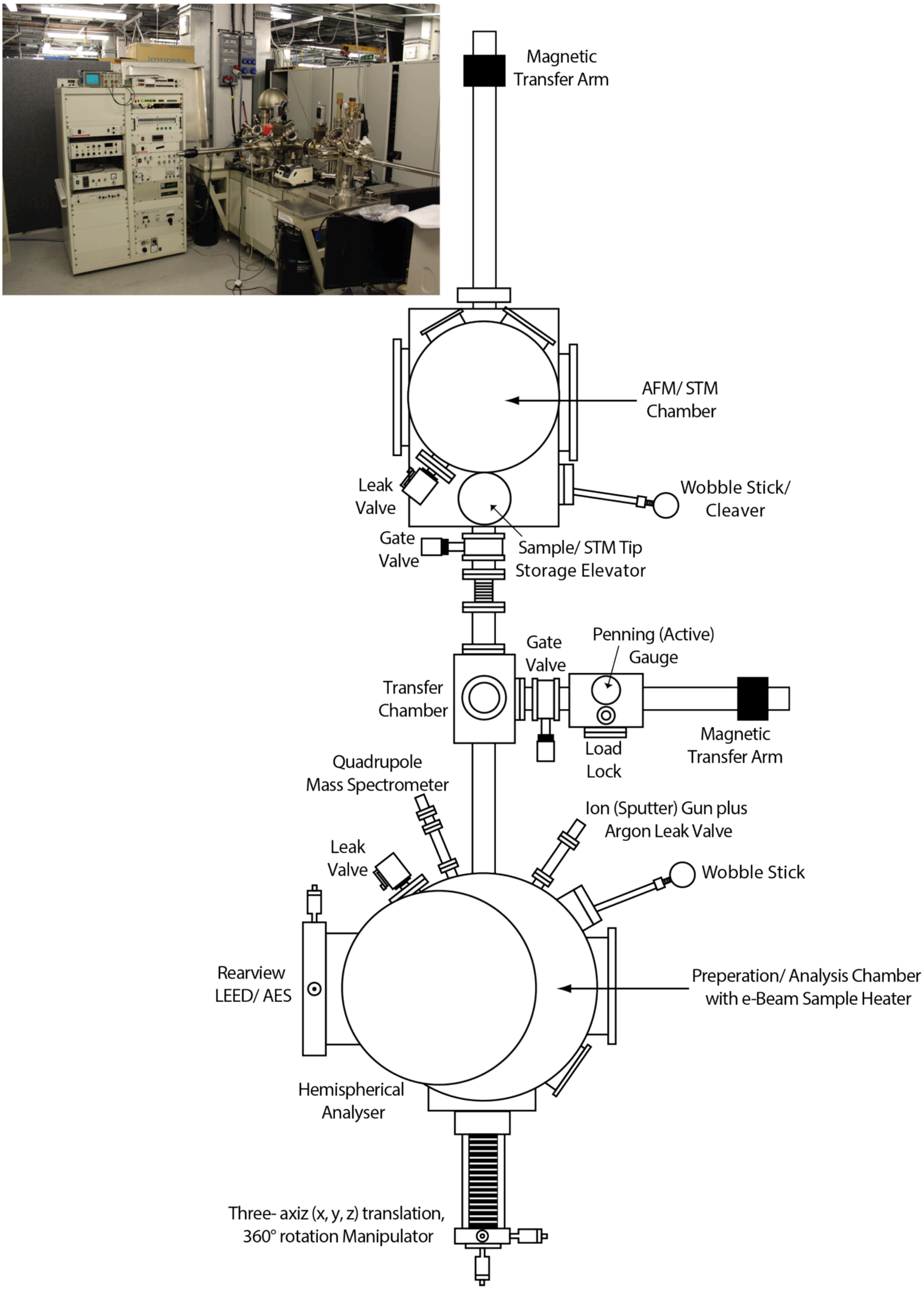

Figure 2.21: Schematic and photograph of the VG Microtech Multilab UHV System.

A series of gauges are used in combination to monitor the pressure taking into careful consideration the pressure limits to which each can accurately measure. For the higher pressures found in the load lock a Penning gauge (Edwards Active Gauage) is used allowing measurements from 10^{-2} down to $\sim 10^{-7}$ mbar, and a Pirani gauge monitors the backing pressure from atmosphere (1013.25 mbar) to $\sim 10^{-3}$ mbar. At lower gas pressures two hot cathode ion gauges, one for the preparation chamber and the other for the STM chamber, serve as a means of monitoring the pressure allowing accurate measurements down to 10^{-11} mbar.

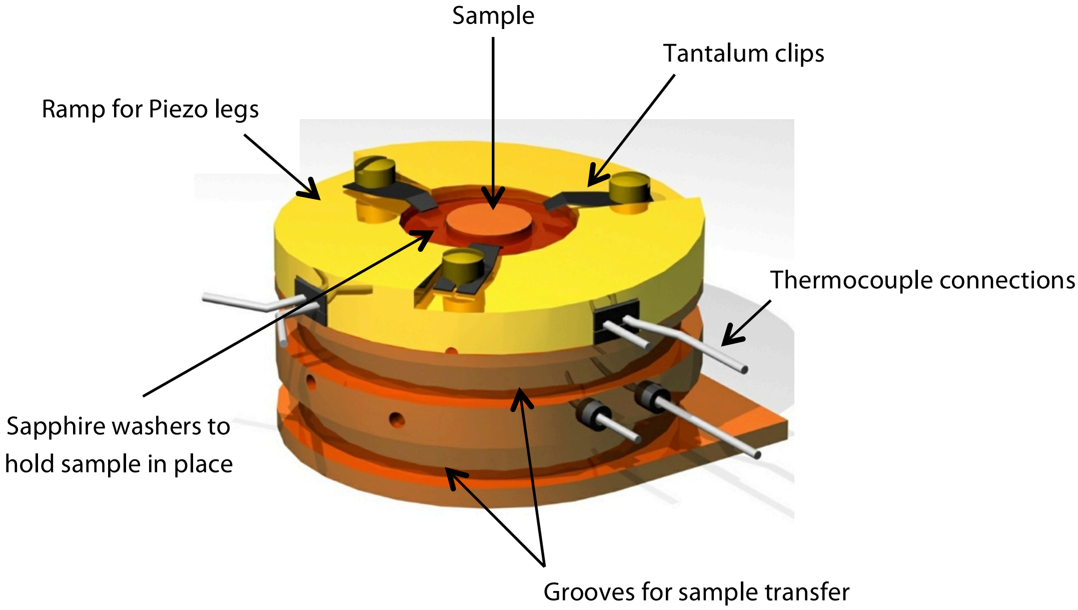

Figure 2.22: Schematic of the RHK sample Holder. Reproduced from [35].

Leak checking of the chamber is done with the mass spectrometer set to leak detection mode. Helium gas is sprayed around the flanges and areas that are suspected to be the cause of the leak. If any leaks are detected in the chamber or manifold the suspected flange is tightened or replaced to ensure a leak tight seal.

2.3.2. Scanning Probe Microscopy (SPM)

The invention of the scanning tunneling microscope (STM) by Binnig and Rohrer in 1981 [36, 37] revolutionised the fields of surface science and nanotechnology [38] triggering the development of many of today's scanning probe microscopy (SPM) techniques [39]. All scanning probe microscopes are designed on the principle that a sensor (probe) is raster scanned across a substrate surface by means of a piezoelectric translator coupled with a highly sensitive feedback system, while a certain signal of interest is recorded by the probe for every single image point, thus providing atomic scale (nm) detail of the substrate surface.

Although a large number of scanning probe microscopy techniques utilising various signal generation mechanisms have recently emerged, scanning tunneling microscopy and atomic force microscopy have been the most widely adopted of the scanning probe microscopy ‘family’ of techniques in the field of surface science, opening up many new areas of science and engineering at the atomic and molecular level.

All the SPM raw data displayed in this thesis has been analysed and processed using WSxM© (**W**indows **S**canning **x** = Force, Tunneling, Near Optical, ... **M**icroscope), a freeware Windows application from Nanotec Electronica for Scanning Probe Microscopy data acquisition and processing [40].

2.3.2.1. Scanning Tunneling Microscopy (STM)

STM revolves around the phenomena of quantum tunneling. When an atomically sharp metal tip (probe) is moved to within a few Angstroms (Å) of the surface of a conducting or semi-conducting substrate, and a small potential difference (bias), of the order of a few millivolts, is applied between the tip and sample a current of the order of a few nanoamperes is generated by the quantum mechanical tunneling of electrons between the two ‘electrodes’ i.e. tip and surface. The resultant tunneling current, which is a function of the tip-surface separation, is measured as the tip is raster scanned over the surface with the help of a piezoelectric scanner. The direction of the electron flow depends on whether a positive or negative bias is applied to the sample or tip. The tunneling current between the conductive sample and the tip is measured as a function of the distance traveled in the x and y directions, building up a topography map of the surface, or more accurately a contour plot of the local density of states near the Fermi level ($LDOS_{EF}$). With precision and refinement this technique is able to image with atomic resolution, as first demonstrated by Binnig *et al.* on the 7×7 reconstruction of the Si (111) surface [41]. Figure 2.23 depicts schematically the working principles of STM.

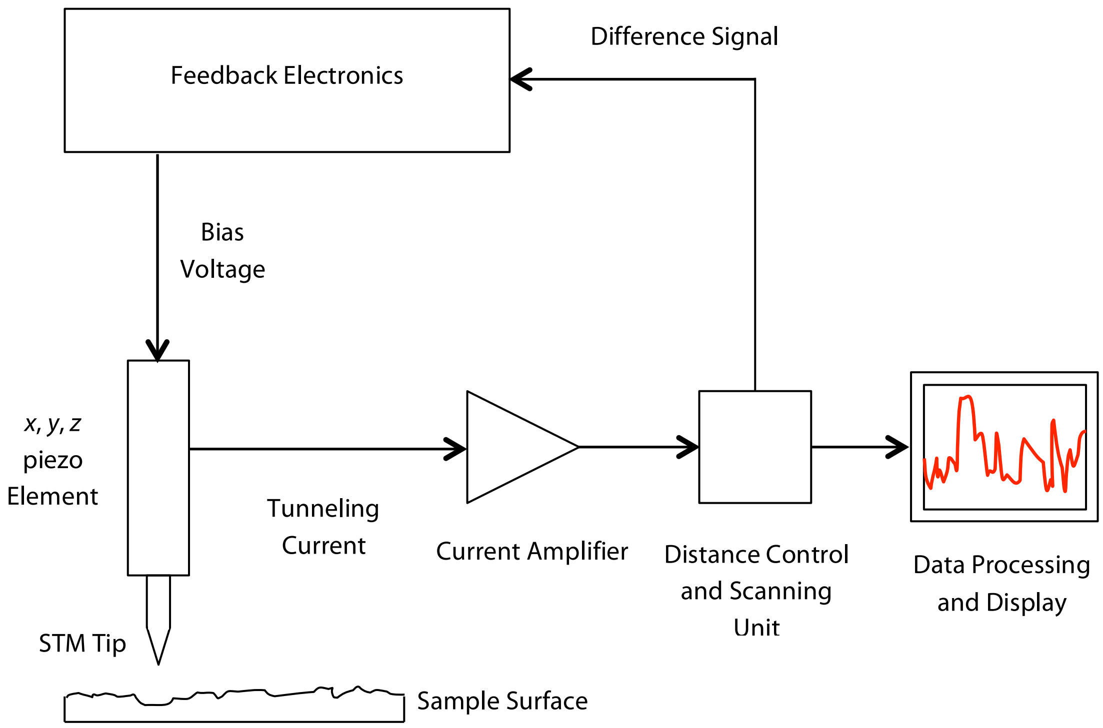

Figure 2.23: Block diagram highlighting the key elements of an STM System

2.3.2.2. Theoretical consideration

In its simplest form the vacuum gap between the tip and the sample surface can be modeled as a one-dimensional energy barrier [37]. Classical mechanics stipulates that a particle (electron) with energy less than the barrier height cannot cross the barrier. However in a quantum mechanical treatment, due to wave particle duality, the particle exists as a continuous wave function decaying exponentially across the energy barrier whose amplitude squared describes the probability of the particle being located at a given position at a given time, and therefore there is a finite probability of the particle tunneling through the barrier. This phenomenon is known as the *quantum mechanical tunneling effect*. Figure 2.24 shows an energy level diagram of a tunneling junction illustrating what happens when a voltage is applied between two metal electrodes separated by a very small distance. Electrons flow from occupied states on the negative electrode to unoccupied states on the positive electrode across the vacuum gap. At low voltage and low temperature under a simple model the tunneling current, I_T across a tunneling barrier width d (tip-sample separation distance) is given by [42]:

$$I_T \propto V_T exp(-2\left(\frac{\sqrt{2m_e\Phi}}{h}\right)d) \tag{2.53}$$

where V_T is the applied voltage, m_e is the mass of an electron, h is Planck's constant and Φ is the average work function of the tip and surface.

From Equation 2.53 it can be seen that the tunneling current has an exponential dependency on the tip-sample separation distance d. For a given work function in the range of a few eV variations of the separation by 0.1 nm changes the tunneling current by a factor of approximately 10. This exponential current-distance relationship is the origin of STM's atomic scale sensitivity to surface topography [36, 37].

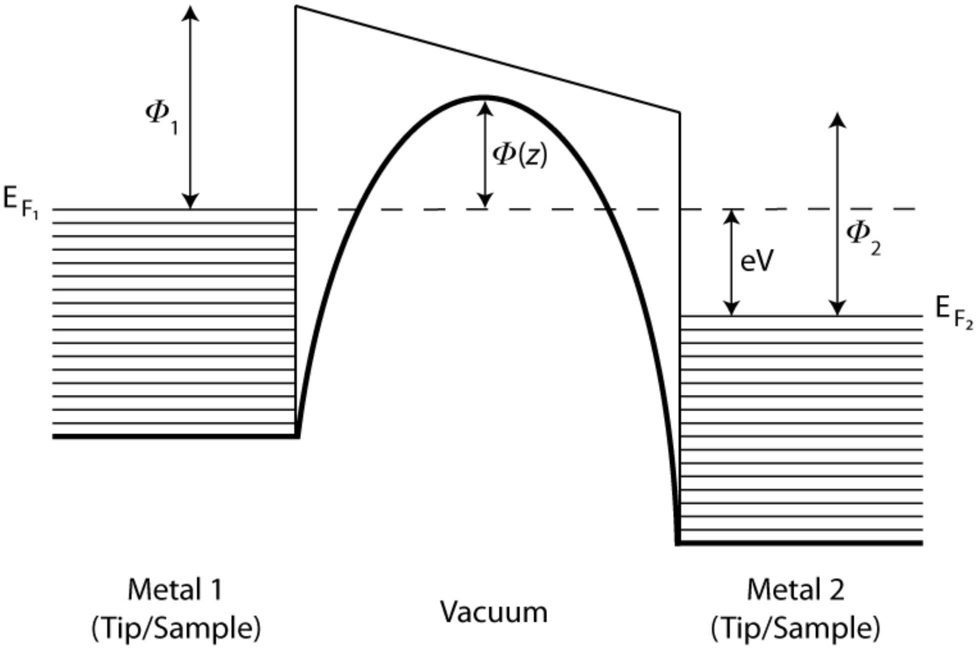

Figure 2.24: Energy Level diagram of a quantum mechanical tunneling junction. Reproduced from [43]

2.3.2.3. Experimental apparatus

STM measurements for this work were undertaken using an Omicron UHV low temperature STM, the ultra high vacuum system housing the microscope has been described in section 2.3.1. In the following sections the relevant experimental aspects of STM are discussed.

2.3.2.4. STM modes of operation

There are two ways of operating an STM, constant current mode and constant height mode [43]. In *constant current* mode, the mode of operation employed for this work, a feedback circuit is used to constantly readjust the tip-surface separation such that the tunnelling current is kept constant and the voltage applied to the *z*-piezo is recorded. In this mode, the STM image is a representation of z-voltage applied to the tube scanner with surface coordinates (x_i, y_i). However if the displacement of the piezoelectric crystal is known for a given change in the bias voltage, then the STM image may then be plotted such that it represents the tip displacement, z_i as a function of the surface coordinates (x_i, y_i), and thus a representation of the surface topography. The vertical displacement of the tip corresponds to a change in the surface height or at the atomic level, change in the local density of states. In this mode of operation the scan speed needs to be kept relatively slow to enable the feedback system to respond to changes in height.

In *constant height* mode, the potential between the tip and surface is kept constant and the varying tunnelling current with lateral position (x_i, y_i) is recorded. Whilst fast scanning, which is favorable in order to limit thermal drift in high resolution imaging, is possible, this method is best suited to atomically flat surfaces as otherwise there is a very high probability of destroying the tip and/or the sample surface (a 'tip crash'). Figure 2.25 shows a schematic of both constant current and constant height STM modes, indicating the evolution of tunnelling current and z-piezo displacement as the tip is rastered along the surface for each mode of operation.

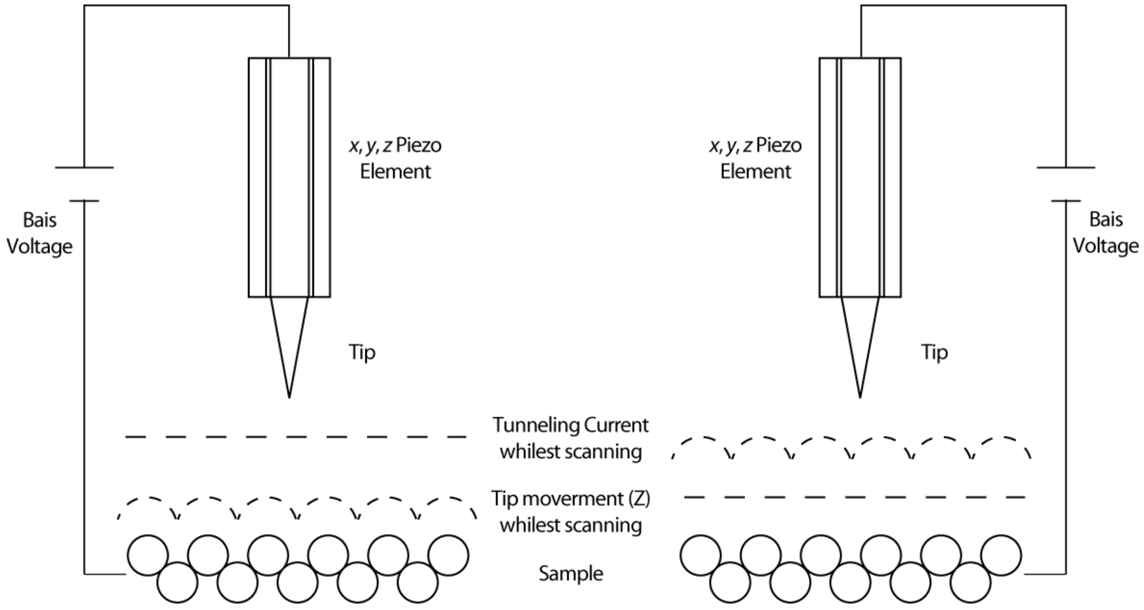

Figure 2.25: Schematic of both constant current (left) and constant height (right) modes of operation. The evolution of tunnelling current and z-piezo displacement for each mode of operation as the tip is rasterd along a solid surface.

2.3.2.5. Vibrational damping

The required isolation/decoupling from external vibrations, necessary for high resolution imaging, of an STM whilst scanning is achieved by the combination of a structurally rigid instrument and an effective vibration isolation system. The former is achieved by keeping the resonance frequency of the STM instrumentation as low as possible, such that other vibrations are so far above resonance that they couple very little. Vibration isolation systems are used to dampen low frequency noise and high amplitude shock vibrations, typically by mounting the entire UHV chamber on a vibration isolation mechanism, such as an air support table, and suspending the STM from the chamber using metal springs with eddy current dampers (consisting of copper elements and permanent magnets). Also as a final good measure ideally the instrument should located in a part of the building known to have the lowest structural vibrations such as the basement floor [39].

2.3.2.6. Piezo-electric materials and scanner

To generate STM images it is necessary to scan the tip back and forth across the surface with angstrom scale precision and repeatability. This three-dimensional motion is achieved by using piezoelectric drives typically a tripod scanner [37] (consisting of three piezoelectric bars perpendicular to each other), a tube scanner [44] or a bimorph made up of piezoelectric materials. Piezo-electric materials are certain crystals and ceramics that change dimensions in response to an applied voltage and conversely, they develop an electrical potential in response to mechanical pressure. This effect was first demonstrated in 1880 by Pierre and Jacques Curie and is known as the piezoelectric effect [45].

The STM used for this study employs a piezo-electric tube scanner; Figure 2.26 shows a schematic diagram of a tube scanner. A piezo-electric tube scanner consists of a thin walled tube made of lead zirconate titanate, PZT [44].

Electrodes are applied to the internal, for out of plane (z) motion, and external faces of the tube facilitating in plane (x and y) motion, with the external electrodes sectioning the outside of the tube into four equal areas parallel to the axis of the tube. By applying a bias to the inner electrode the tube extends or contracts, and if a bias is applied to only one of the outer quadrants the tube will bend.

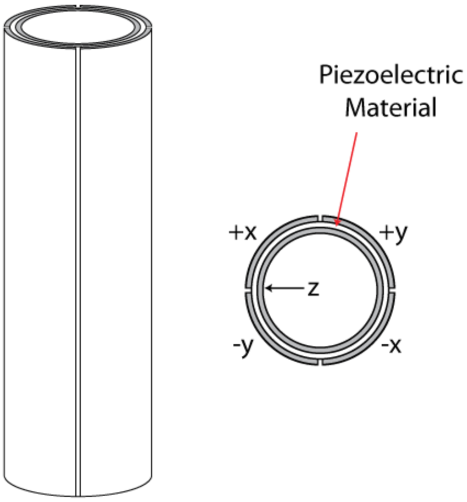

Figure 2.26: Diagram of a piezo-electric tube scanner

2.3.2.7. STM Tip fabrication

The tip (probe) used for STM experiments should be chemically stable and ideally have a single atom centred at its apex, so that it is atomically sharp [46]. However, in practice the tip needs to be sharp enough to generate an image that has atomic resolution fairly effortlessly. For these reasons alloys of Platinum-Iridium (typically 80% Pt - 20% Ir) or Tungsten are frequently used for the fabrication of STM tips. A number of techniques for tip preparation have been reported [39]; of which, two techniques are particularly popular amongst STM users. The first technique is mechanical sharpening by cutting the Platinum-Iridium alloy wire at an oblique angle with a sharp wire cutter [39, 47]. The second technique is to chemically etch Tungsten wire using a chemical agent, typically sodium hydroxide (NaOH) [48, 49] or potassium hydroxide (KOH) [46]. Figure 2.27 shows SEM Images of an STM tip sharpened by (left) mechanical sharpening and (right) chemical etching.

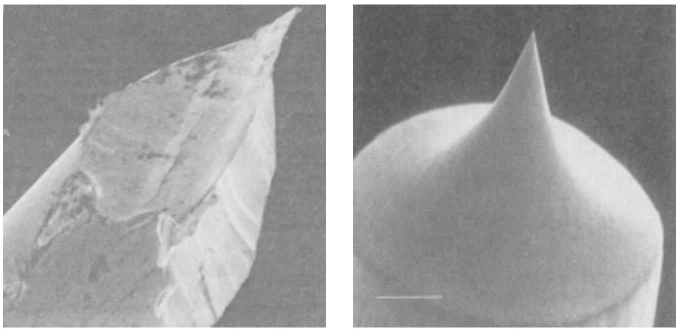

Figure 2.27: SEM images of an STM tip sharpened by mechanical sharpening (left) and chemical etching (right).

The STM tips used for this study are made through the electrochemical etching of a 0.25mm diameter tungsten wire (99.95% purity, purchased from Goodfellow Cambridge Ltd.) in 1 Molar sodium hydroxide (NaOH).

Figure 2.28 shows a schematic of the electrochemical etching cell used to etch the tungsten wire (anode) in NaOH solution to form a chemically etched STM tip, with an applied dc voltage between the cathode and anode that drives the etching process. A 5mm diameter gold ring placed around the anode serves as the cathode. Also depicted is the "flow" of the tungstate anion down the sides of wire in solution and the subsequent in flow of fresh electrolyte containing OH^- ions. Etching occurs at the air-electrolyte interface where a neck is formed and the immersed portion of the wire eventually drops off when the weight of the submerged region of the wire exceeds the tensile strength of the etched part leaving a sharp tip. The oxide layer coating the tip (WO_3), as a result of exposure to air, is immediately washed off with distilled water, and the tip quality is assessed using an optical microscope. To ensure the removal of any absorbates/contaminants that maybe present on the tip, it is often best practice that the tip is degassed by annealing in vacuum prior to use [47].

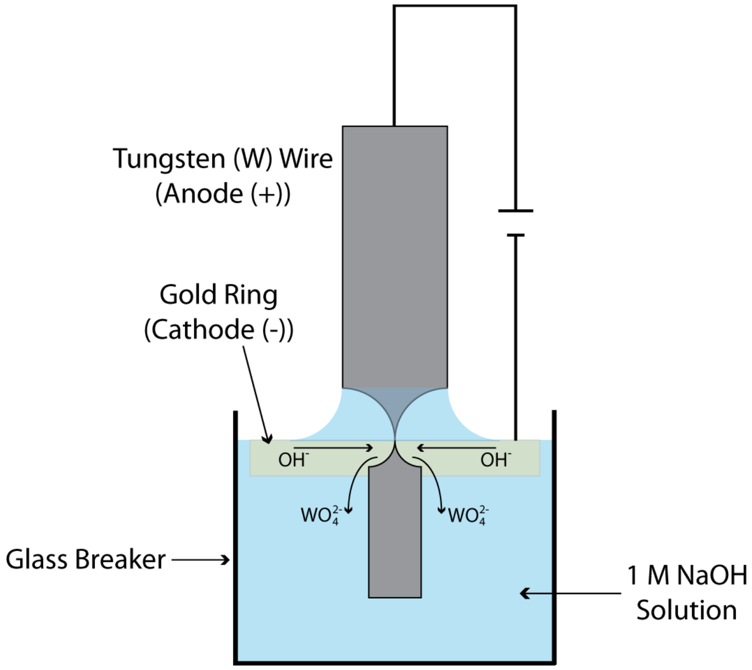

Figure 2.28: Schematic diagram of the electrochemical tip etching apparatus.

2.3.3. Low Energy Electron Diffraction (LEED)

Since the discovery, in 1927, by Davisson and Germer [50] that the elastic scattering of low energy electrons incident on a well ordered single crystal surface leads to distinct diffraction spots and the subsequent developments in vacuum technology, low energy electron diffraction (LEED) has become very important in elucidating single crystal surface structure and one of the standard techniques of modern surface crystallography. For a comprehensive treatment of the practical and theoretical aspects of LEED the reader is refereed to the excellent text by Clarke [51].

In *LEED*, a monochromatic electron beam of low energy (typically in the range of 20-500 eV) incident normal to a single crystal surface is back-scattered, and diffraction can be detected if the surface is sufficiently well ordered. The diffracted beams travel through a number of energy filtering grids to remove any inelastically scattered (secondary) electrons and form a pattern on a fluorescent screen whose symmetry reflects that of the underlying surface structure [51]. Figure 2.29 shows a typical LEED pattern acquired from TiO_2(110) surface at 100 eV following sample preparation in UHV.

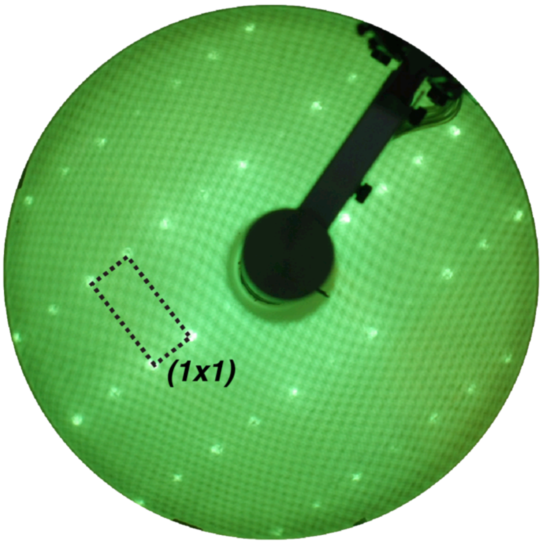

Figure 2.29: Typically LEED Pattern acquired from TiO_2(110) at 100 eV

Through the principle of wave-particle duality, a beam of electrons incident normal to a substrate surface may be regarded as a succession of electron waves, which may be scattered by regions of highly localised electron density, namely the surface atoms. The wavelength of the electrons is given by the de Broglie relationship [52]:

$$\lambda\,(\text{Å}) = {}^{h}/_{p} \tag{2.54}$$

where h is Planck's constant ($= 6.62\times10^{-34}\,\mathrm{J\cdot s}$) and p is the electron momentum given by:

$$p = m_e v = (2me \cdot V)^{\frac{1}{2}} = (2mE_{kin})^{\frac{1}{2}} \tag{2.55}$$

m_e is the electron mass, v is the velocity, e is the electronic charge, V is the acceleration voltage and E_{kin} is the kinetic energy of the electron. Substituting Equation 2.55 into Equation 2.54 yields a wavelength:

$$\lambda\,(\text{Å}) = ({}^{150.1}/_{E_{kin}})^{\frac{1}{2}} \tag{2.56}$$

Therefore for energies in range of 20 to 500 eV electrons will have de Broglie wavelengths of between 2.7 Å and 0.55 Å, which is comparable to the interatomic spacing of many crystalline materials. This coupled with the fact that low energy electrons have a very small inelastic mean free path, λ_m (the average distance traversed by an electron with kinetic energy E_{kin} in a solid matrix before it loses all or part of its energy due to inelastic collisions) of the order of a few Angstroms (typically less than 10 Å), electrons at this range of energies sample only the topmost atomic layers, renders the technique an excellent probe for the study of surface geometries [53].

LEED can be used to gather both quantitative and qualitative information for surface structure determination. Qualitative *LEED* involves the analysis of the spot positions, quality and sharpness can yield information on two dimensional surface lattice parameters and a means of qualitatively characterizing surface ordering. In quantitative *LEED* information about the position of the surface atoms is hidden in the energy dependence of the diffraction spot intensities, so-called I-V curves which, by comparison with theoretical curves much like SXRD structure determination, may provide accurate information on atomic positions within the surface by trial and error [43, 51].

2.3.3.1. Instrumentation

LEED data acquired as part of this thesis were collected using a VG Microtech Reverse View LEED optics with a four grid mesh assembly, employing a model 8011 power supply and controller. The mesh assembly consists of four hemispherical concentric grids and a spherical phosphor coated sector glass screen. The electron gun is located inside the gun mounting tube, which runs through the centre of the screen and meshes.

A mu-metal cylinder hood, that provides shielding from stray magnetic fields and electrons, surrounds the LEED optics and electron gun assembly. Images of the LEED pattern were recorded using a digital camera.

Conventional LEED optics are either 'front' or 'rear' view, although most modern LEED optic set-ups are of the 'rear' view type [43]. Figure 2.30 shows a schematic of a LEED optics. The optics assembly typically consists of two to four concentric grids and a fluorescent phosphor coated screen. In a four-grid assembly the first grid (nearest to the sample) is connected to the earth ground, as is the sample, to provide a field free region between this grid and the sample minimising electrostatic deflection of diffracted electrons. The next two grids, 'suppressor grids', are held at negative potentials, and act to filter out inelastically scattered electrons and only allow elastically (or near) scattered electrons to pass through to the screen. These two suppressor grids are usually connected together by an internal link and behave as one mesh. The fourth grid is earthed to reduce field penetration to the suppressor grids from the screen, which is held at a high voltage (on the order of a few kV) so as to accelerate the elastically scattered electrons onto the screen [51].

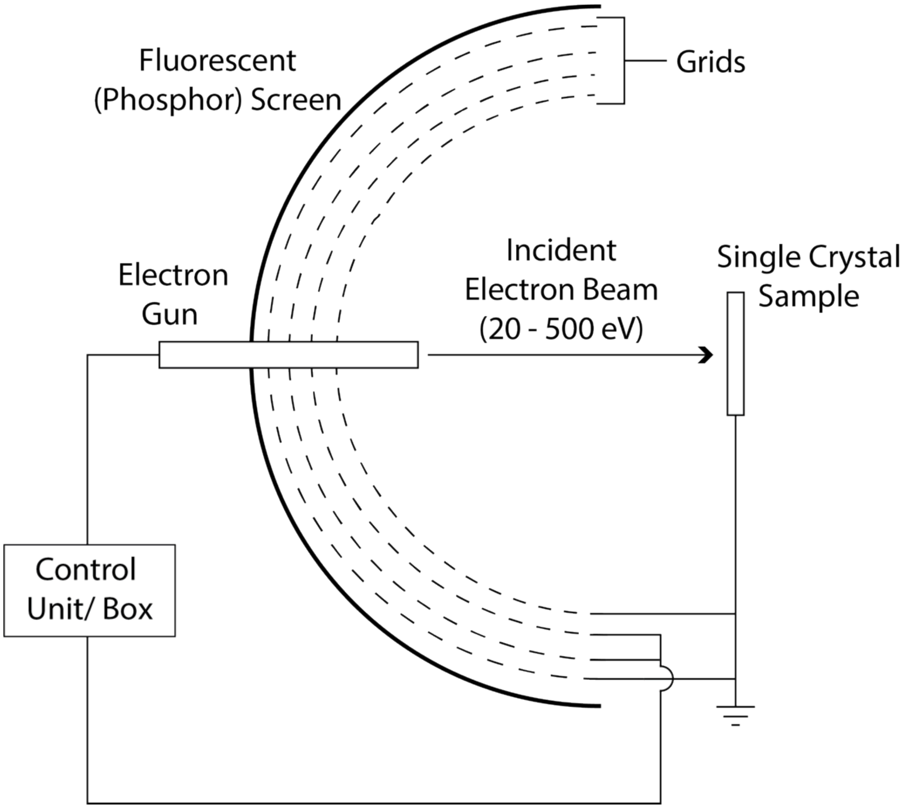

Figure 2.30: Schematic of a four-grid rear view LEED optics system.

2.3.4. Auger Electron Spectroscopy (AES)

Auger Electron Spectroscopy is a surface sensitive characterisation technique utilising the emission of low energy electrons to render information on the elemental (chemical) composition of approximately the top five atomic layers or so of a solid surface, depending upon the material and ionizing energy [54]. Underlying this spectroscopic technique is the *Auger effect*, first observed in 1925 by Pierre Auger [55], involving the inter and intrastate transitions of electrons in an excited atom. However the practicalities of the technique as known today were first described by Lender [56] in 1953. Figure 2.31 (top) illustrates sequentially the steps involved in the Auger process and (bottom) Illustrates the same using spectroscopic notation.

If a solid surface is irradiated by an electron beam (or X-ray) of sufficient energy typically in the range of 0.5 to 5 keV (however an initial ionisation energy of 3 keV is often used as this allows for comparison with published reference data [57] under UHV conditions) a core level electron is ejected from the inner shell of the surface atoms and an electron will drop from a higher energy level to fill this vacancy. The excess energy released in the transition is either emitted as an X-ray photon (fluorescence) or secondary Auger electron; this process is known as the *Auger effect*. This ejected secondary electron has a characteristic kinetic energy; E_{kin}, given by Equation 2.57 below, which forms a small peak in the total energy distribution function *N (E)*.

$$E_{kin}(KL_1L_{23}) = E_K - E_{L_1} - E_{L_{23}} - \varphi \tag{2.57}$$

The resultant kinetic energy is a function of atomic energy levels only and given that no two elements have the same set of atomic binding energies, analysis of the Auger energies provides a precise means of determining elemental composition. It is apparent that two energy states and three electrons must take part in an Auger process; therefore, hydrogen (H) and helium (He) atoms cannot give rise to Auger electrons. It is important to note that Auger peaks are overwhelmed by a large background of inelastically scattered electrons, and so it is common to plot the derivative of the Auger spectrum, *dN (E)/dE* vs. *E*, as opposed to *N (E)* vs. *E*.

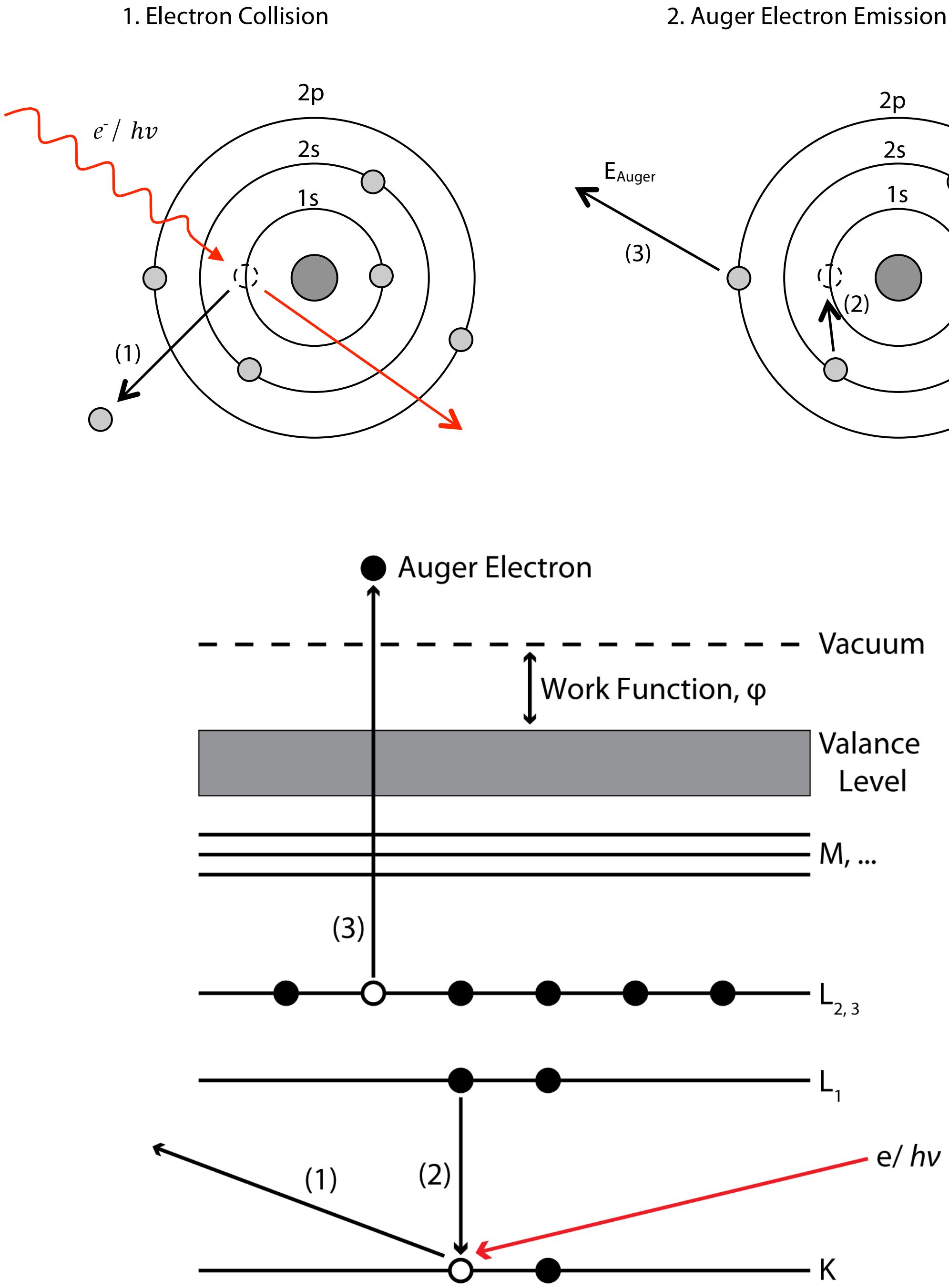

Figure 2.31: The Auger process. (top) Illustrates sequentially the steps involved in an Auger process. An incident electron (or photon) creates a core hole in the 1s level – Step 1. An electron from the 2s level fills in the 1s hole – Step 2, and the transition energy is imparted to a 2p electron which is emitted – Step 3. The final atomic state thus has two holes, one in the 2s orbital and the other in the 2p orbital. (bottom) Energy level diagram of the Auger process using spectroscopic notation.

The concentration of each element present can be estimated from the intensity of the Auger peaks, where the intensity is taken as the difference between the positive and negative peaks of the Auger double peak. Much like LEED the surface sensitivity of this technique arises from the short mean free path of the emitted Auger electrons [43].

2.3.4.1. Instrumentation

The standard equipment for *AES* consists of an electron gun and a combined detector and analyser system under UHV. The sample is irradiated with a focused electron beam from an electron gun. The secondary electrons emitted as result of the *Auger process* are transmitted through a set of electrostatic lenses to the analyser, typically a cylindrical mirror [59] or concentric hemispherical analyser [53] (CMA and CHA respectively). The analyser acts as a narrow band pass filter; passing only those electrons with a specific energy.

The AES system used for this study is housed in/forms parts of the RHK variable temperature combined STM/AFM UHV system described in section 2.3.2, which is maintained at a base pressure of approximately 1×10^{-10} mbar. The analyser used is a Thermo VG Microtech VG100AX CHA with a 100 mm (mean radius) surrounded in a Mu-metal housing. The analyser consists of thee main parts; two lenses in 3:1 magnification mode for AES, an analyser typically operated in constant retard ratio (CRR) energy analysing mode and a single channeltron detector. The electrons enter and exit the analyser through 4 mm wide slits. Figure 2.32 shows a schematic of a Hemispherical Analyser. Spectroscopy data is collected using the VGX900IC acquisition and processing software package.

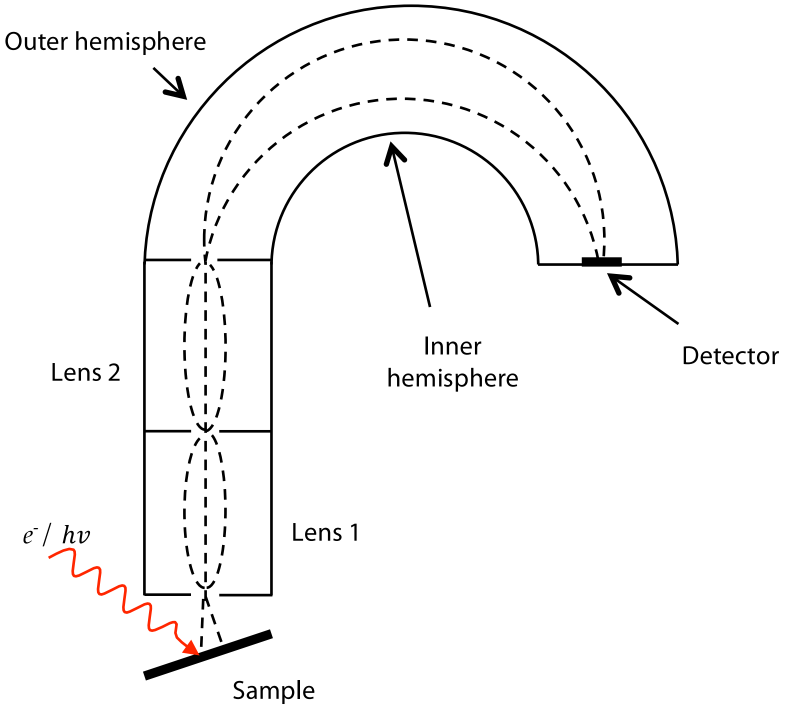

Figure 2.32: Schematic of a hemispherical analyser.

2.4. Non-UHV Techniques and Instrumentation

Several in air surface characterisation techniques, namely Atomic Force Microscopy and Contact Angle Goniometry, were employed to collect data for this thesis. Their theoretical and experimental background are described in the following sections.

2.4.1. Atomic Force Microscopy (AFM)

Atomic Force Microscopy (AFM), first developed in 1986 by Binnig, Quate and Gerber [60], is an SPM technique in which a sharp probe is raster scanned over the surface of a sample and the changes in the interaction forces (e.g. attractive, repulsive, van der Waals) between the probe tip and surface structure features are measured. Figure 2.33 shows a schematic of the working concepts of an AFM. By scanning the tip back and forth across the surface and recording the change in force as a function of position, a three-dimension map of surface topography and other properties can be generated [61].

Most commercially available AFM's, including the one used for this study, employ an optical laser detection system in which the tip is attached to the underside of a reflective cantilever [62]. In the most common scheme a laser beam is focused and positioned onto the rear of the reflective cantilever, and as the tip is scanned across the surface, the laser beam is deflected off the cantilever into a Position Sensitive Quad Photodiode detector. By calculating the difference signal (i.e. the difference in light intensity) in each of the photodiode quadrants, the amount of deflection [(A+B)-(C+D)] can be correlated with a height for each single data point and because the cantilever obeys Hooke's Law for small displacements, the interaction force between the tip and the sample can be determined. Feedback from the photodiode detector difference signal, through the feedback electronics, enables the probe to be maintained at either a *constant force* or a *constant height* above the surface [43]. In the constant force mode the cantilever deflection, and thus the force is kept constant by monitoring real time height deviation in the topographical features of the surface. In the constant height mode the vertical position of the sample is maintained constant and the varying deflection of the cantilever, and thus force on the sample, is recorded.

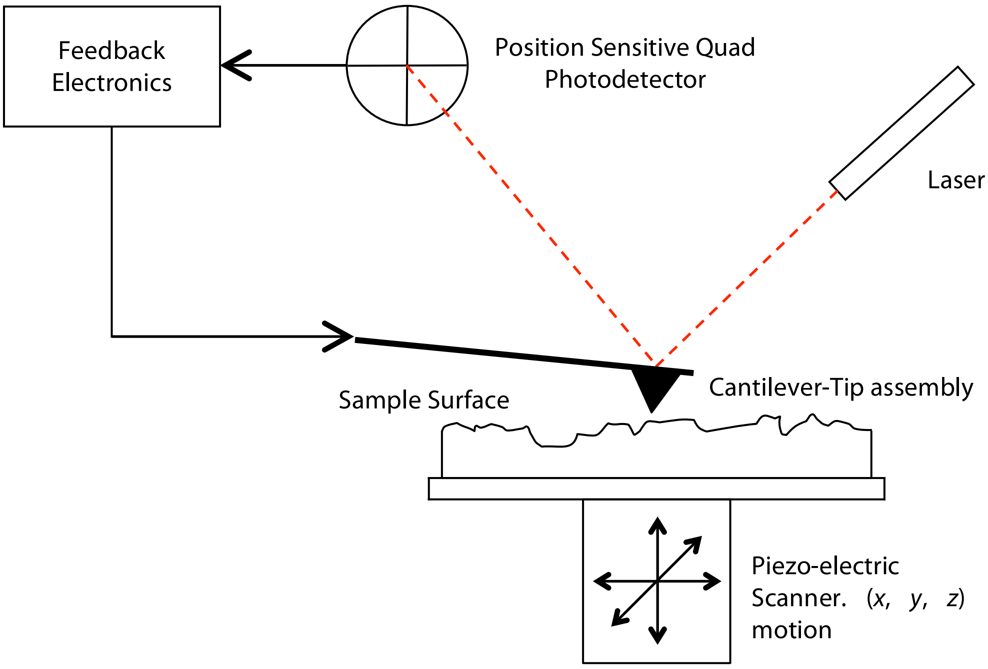

Figure 2.33: Schematic outlining the operating principle of AFM.

2.4.1.1. AFM Modes of Operation

AFM's are typically operated in one of three different imaging modes; *tapping mode* (TM-AFM), *contact mode* (C-AFM) and *non-contact mode* (NC-AFM) [45]. Figure 2.34 shows a schematic of each of these modes of operation. These modes of operation can be described as either *static* (*contact mode*) or *dynamic* (*non-contact and tapping mode*). In *static* mode the AFM tip is 'dragged' across the sample surface and the deflection of cantilever gives a direct measurement of surface topography. This mode of operation generally provides the highest resolution imaging of all the AFM modes of operation because of the direct contact that the tip makes with surface. However, as it is heavily dependent on frictional and adhesive forces it can cause a lot of damage to the surface/tip and in some cases result in removal/addition of material to/from the surface. In d*ynamic* mode the cantilever is oscillated at/near to its resonant frequency, or at a higher harmonic of it. Any changes to the oscillation amplitude, phase and resonance frequency as result of the tip's interaction with sample renders information on the surface topography. The difference between the two dynamic modes of operation, namely *non-contact and tapping mode*, is that in *non-contact mode* AFM the tip is maintained a set distance away from the sample surface typically in the region of 50-150 Å [63], such that it does not make surface contact. Imaging in this mode tends to be of lower resolution. In *tapping mode* the tip makes intermittent contact and moves completely away from the sample surface in each oscillation cycle. Tapping mode has the advantage that high-resolution imaging can be achieved without inducing destructive frictional forces and so soft or fragile samples can often be successfully imaged.

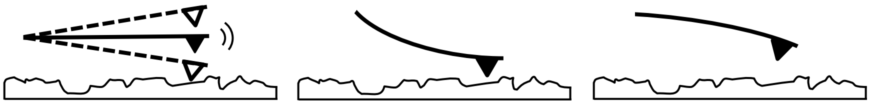

Figure 2.34: A diagram to illustrate the three modes of AFM operation - Tapping Mode (left), Contact Mode (middle) and Non-Contact mode (right).

2.4.1.2. Instrumentation

The AFM used for this study is an in-air *VEECO Multimode Scanning Probe Microscope*, (MM-SPM), employing Nanoscope III SPM software (Digital Instruments), as shown Figure 2.35 (left). The MM-SPM is mounted on an active vibration isolation table, which works by actively phase-cancelling any induced ambient vibrations through a detector-actuator feedback element. This MM-SPM is designed around a stationary probe such that the sample, mounted directly on top of the scanner, is raster-scanned underneath the probe. Motion of sample is performed by a single piezoelectric tube scanner made of lead zirconate titanate, PZT, which contracts and elongates when a voltage is passed through it for lateral translation (x and y) and tip-sample separation distance adjustment (z). The samples are fixed (using carbon sticky tabs) to a 1.5 cm diameter metal disk that magnetically adheres to the scanner tube.

The MM-AFM employs a laser detection system to measure and quantify the motion of the cantilever; Figure 2.35 (right) shows an expanded image of the AFM head.

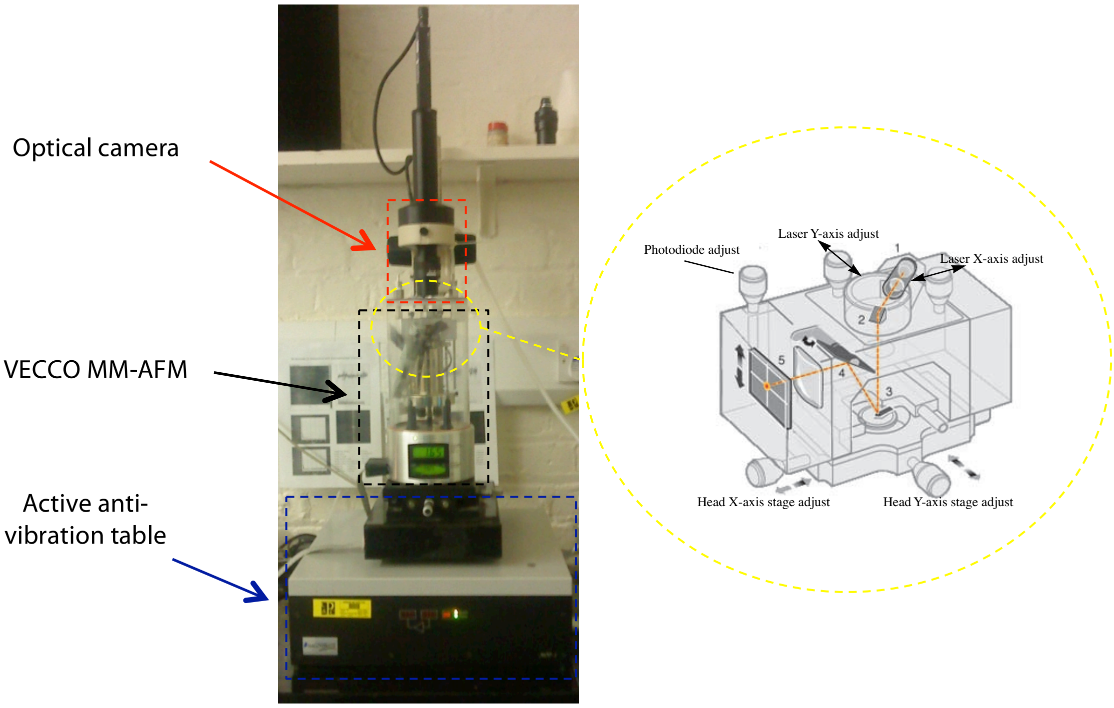

Figure 2.35: (left) Photograph of the VEECO Multimode Scanning Probe Microscope at the University of Manchester. Also shown (right) is a schematic view of the laser deflection AFM head used in the VECCO MM-SPM, image take from [64] .

2.4.1.3. AFM Tip

The properties and dimensions of the tip and cantilever assembly used in AFM play a very important role in the sensitivity and resolution of the AFM. The tip should be very sharp with a small radius of curvature and a high aspect ratio, so as to be able to trace fine details on the surface. The cantilever should have a low spring constant, so as to achieve a measurable deflection without destructive displacement of the surface atoms. It also requires a high resonant frequency to minimise noise resulting from coupling with low frequency noise from the surrounding environment. These characteristics are achieved by making the cantilever as short as possible, thus providing a high resonant frequency, and by making the cantilever thin, to provide a low spring constant. Commercially available probes are usually made of silicon nitride or single crystal silicon produced by etching techniques; the tip and cantilever are typically an integrated assembly [45]. The cantilever tips used for this work are TESPA model wafer tips (Purchased from Bruker) made of 0.01 – 0.025 ohm-cm antimony (n) doped silicon. They are approximately 110-140 μm in length with resonant frequencies between 281 – 355 kHz and spring constants in the range of 20 – 80 N/m.

2.4.2. Contact Angle Goniometry

The contact angle provides microscopic information about surface chemistry through assessing surface wettability. The nature of the surface bonds will dictate the wettability of a surface [65]. The contact angle is thus a quantitative measure of the wettability of a solid surface by a liquid, described geometrically as the angle formed by a liquid with a solid surface at the three phase boundary where a liquid, gas and solid intersect [66].

Figure 2.36 shows schematically three classes of contact angles formed by a liquid droplet on a smooth homogeneous solid surface used to quantify wettability. A small contact angle, $\theta < 90°$, corresponds to high wettability indicating that the liquid will spread over a large area of the surface. In contrast a large contact angle, $\theta > 90°$, corresponds to low wettability and so the liquid will try to minimise its contact with the surface and forms a compact liquid droplet. A contact angle of zero represents complete wetting of the surface by the liquid [67].

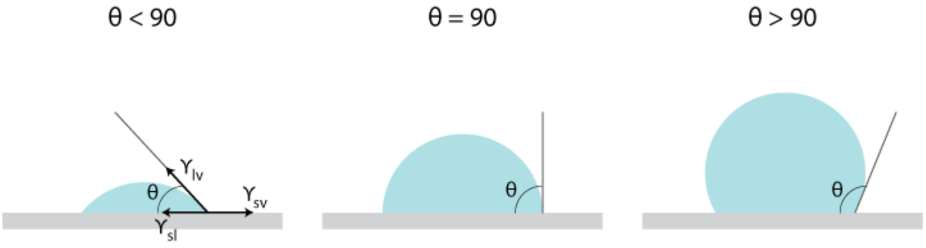

Figure 2.36: Illustration of classes of contact angles formed by liquid drops on a smooth homogeneous solid surface used to quantify wettability. Reproduced from [67]

First described by Thomas Young in 1805 [66], the contact angle for a liquid droplet on an ideal homogeneous solid surface is a measure of the equilibrium form of the droplet under the action of three opposing interfacial energies/tensions:

$$\cos\theta = \frac{\gamma_{sv} - \gamma_{sl}}{\gamma_{lv}} \tag{2.58}$$

where γ_{lv}, γ_{sv} and γ_{sl} are the interfacial energies/tensions for the liquid-vapour, solid-vapour and solid-liquid interfaces respectively and θ is the contact angle. Equation 2.58 is referred to as *Young's Equation*.

Several techniques for measuring contact angle have been developed over the years [68, 69]. The selection of which very much depends on the geometry and material composition of the sample (i.e. shape and size), the desired degree of accuracy, convenience and relative practical ease of the technique. The method used to acquire contact angle data for this thesis is the *static sessile drop method* in which a droplet of known volume of liquid (deionised water in this case) is gently dispensed onto the sample surface from above using a manually operated micrometer syringe and allowed to sit freely. Several static 'snapshot' images are taken and thus the profile of the drop is captured digitally using a high-resolution camera, from which the average contact angle and the associated error can be measured using one of a number of different image analysis algorithms. Figure 2.37 shows a snapshot image of a contact angle measure using the static sessile drop method. An accuracy of ±2° between successive contact angle measurements is reported by Fox and Zisman [70], who are credited with popularising the static sessile drop method. However, the accuracy of contact angle measurement in reality is often a matter of precision and depends on the accuracy of the instrument used, the level of care taken by the investigator and the image fitting technique used [71].

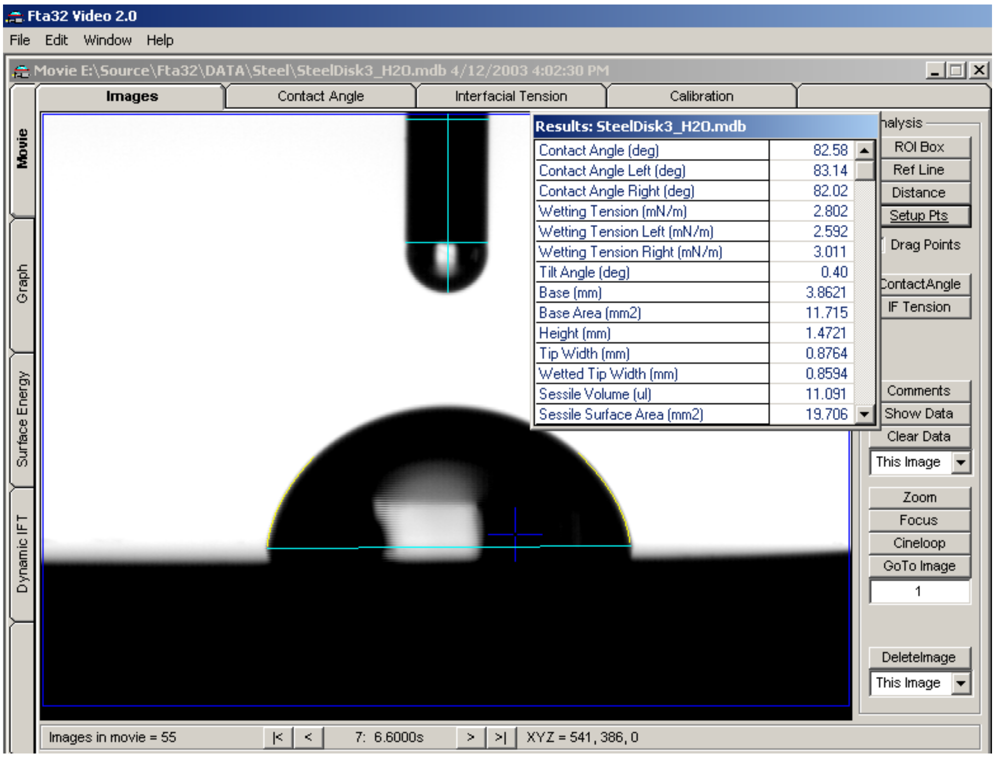

Results: SteelDisk3_H2O.mdb

Contact Angle (deg)	82.58
Contact Angle Left (deg)	83.14
Contact Angle Right (deg)	82.02
Wetting Tension (mN/m)	2.802
Wetting Tension Left (mN/m)	2.592
Wetting Tension Right (mN/m)	3.011
Tilt Angle (deg)	0.40
Base (mm)	3.8621
Base Area (mm2)	11.715
Height (mm)	1.4721
Tip Width (mm)	0.8764
Wetted Tip Width (mm)	0.8594
Sessile Volume (ul)	11.091
Sessile Surface Area (mm2)	19.706

Figure 2.37: Print screen of a typically contact angle measurement using Fta32 software. Contact angle measured employing the static sessile drop method.

2.4.2.1 Instrumentation

The contact angle goniometer used for this study is the FTÅ 188 Contact Angle and Surface Tension Analyzer (First Ten Angstroms Inc., USA). The sample is mounted on a rack and pinion stage, which allows X, Y and Z positioning of the sample with respect to the microscope. A manually operated micrometer syringe is used to control the rate of liquid addition and removal. Figure 2.38 shows an image of a FTÅ 188 Contact Angle and Surface Tension Analyzer. Static images or dynamic videos are taken using the microscope mounted CCD camera, and are analysed using the Fta32 Video software in which the user defines the droplet baseline and the software picks out the droplet radius of curvature and subsequently calculates the contact angle.

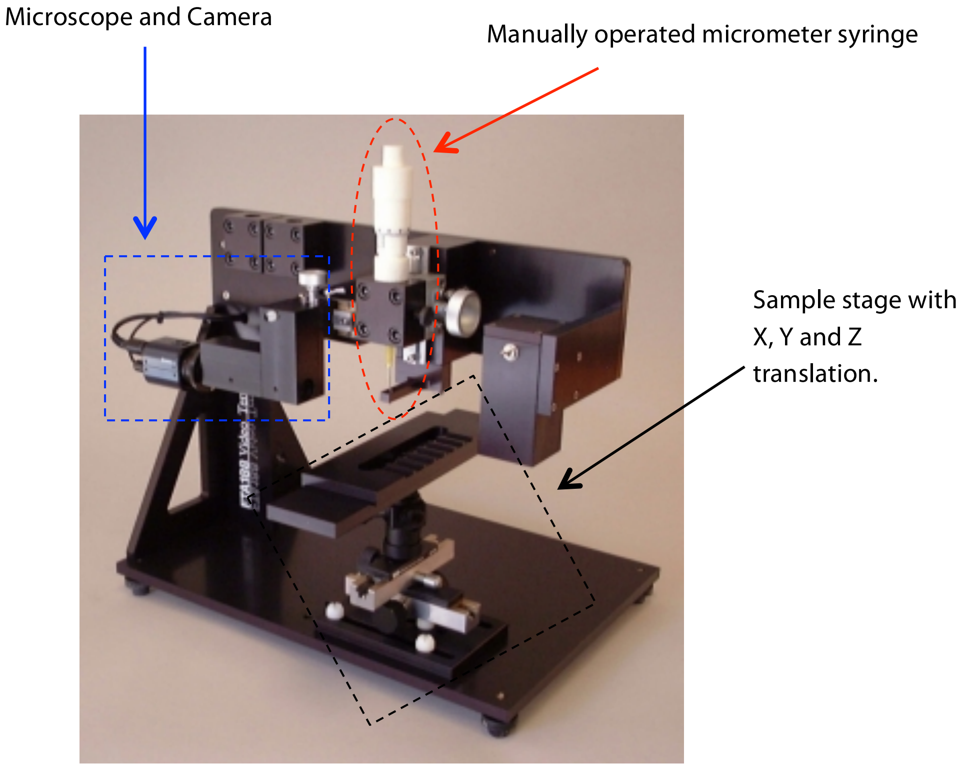

Figure 2.38: The FTÅ 188 Contact Angle and Surface Tension Analyzer. Photograph taken from [72].

2.5. Sample Preparation

One of the main factors governing the quality of the data collected for the study of surface crystallography is the preparation and preserving of a well-defined surface i.e. a well-ordered, atomically flat and contaminant-free surface. The latter is often maintained by carrying out studies under UHV conditions. However there is no general recipe for surface preparation, and it very much depends on the material and surface orientation as to the specific methodology. Preparation is either done typically under vacuum (*in situ*) or outside vacuum (*ex situ*) and then later the sample is transferred into the chamber for further studies. Specific, to metal oxides the main methods for surface preparation include *in situ* ion sputtering/bombardment and annealing, *in situ* cleaving, and *ex situ* 'wet chemical' preparation methods [1].

2.5.1. *In situ* ion sputtering/bombardment and annealing

Surface contamination is removed by bombarding the surface under UHV with a high flux of inert ions (commonly noble gas ions e.g. Ar^+) with energies typically in the range of 0.5 keV to 5 keV, which strike and destroy the surface at a rate of 0.1 to 10 atomic layers per second. This method leaves the surface, although clean, in a heavily roughened state [1]. The ion current and duration of bombardment depend on the material and the degree of contamination. Often due to the different removal rate of atoms during sputtering, bombardment may cause changes in the surface composition. However surface order can be regained through high temperature annealing under UHV. Annealing is also necessary for the removal of embedded ions. The anneal temperature is very much dependent on the material. Typical values for cleaning a polished 10 mm^2 $TiO_2(110)$ surface in UHV would be ion bombardment at a filament current of 1.25 mA, beam energy of 500 eV for 10 minutes and annealing at 750-850 °C for 30 minutes.

A clean, well-ordered surface is easily obtained with the alternation of ion sputtering and annealing, between each cycle the surface is checked using *AES* or *XPS* for cleanliness and *LEED* for crystallographic order. These repeated cycles of bombardment and annealing are stopped when satisfactory results are obtained for cleanliness and surface order. To obtain stable, reproducible results from metal oxide surfaces cycles of ion sputtering and annealing have to be repeated several times.

2.5.2. *In situ* cleaving

For brittle materials, clean, well-defined surfaces can be prepared in UHV by cleaving [73]. Cleavage of a single crystal surface in UHV is achieved by applying mechanical pressure to the substrate with a razor sharp blade along the desired crystallographic plane [74]. In most UHV systems the cleaving blade is commonly attached to the end of a wobble stick. Cleavage as a means of preparing single crystal surfaces for UHV studies is only possible with brittle materials such as oxides [73, 75] (ZnO, MgO, NiO $SrTiO_3$ etc…) and semiconductors [1] (Ge, Si, GaAs etc…), and along certain crystallographic directions that are determined by the geometry and nature of the chemical bonds. Although cleaved surfaces are often stoichiometric they can contain defects such as steps [1].

2.5.3. *Ex situ* 'wet chemical' preparation

Owing to recent technical and experimental developments a desire to study surfaces under more realistic 'real world' environments, such as ambient pressure and fluid/solid interfaces, in order to gain insight into the fundamental physics and chemistry of many surface processes [76]. However to date the main obstacle to the fulfillment of such an endeavor has concerned the preparation of well-ordered and largely contamination-free surfaces. In an effort to fill this gap and permit the exploration of a range of systems, some groups have sought to employ so called non-UHV wet chemical methods, focusing on the preparation of the TiO_2(110)(1×1) surface. Typically, non-UHV, or wet chemical, preparation of metal oxide surfaces involves annealing under atmospheric conditions, and etching with aqueous hydrofluoric acid (HF) [77, 78]. The purpose of the in-air annealing is analogous to that of the same process in UHV, i.e. to produce an atomically flat and well-ordered surface. Etching removes surface contamination from the sample surface, equivalent to ion sputtering in UHV sample preparation.

An alternative non-UHV 'wet chemical' technique for preparation of metal oxide surfaces forms the basis of chapter 6. Most importantly, the use of hydrofluoric acid (HF) is circumvented, which is difficult to handle owing to it being a contact poison, replacing it with Aqua Regia (3 part HCl, 1 part HNO_3). Ultra Violet (UV) light treatment is undertaken in a final step to regulate adventitious carbon contamination. A critical assessment of the utility of this methodology through characterisation of the surface structure and composition of the low index TiO_2 (110) and (011) surfaces with *AFM*, *STM*, *LEED*, *AES*, and contact angle goniometry is also presented showing the effectiveness of this technique in preparing clean, well-defined metal oxide surface reproducibly.

2.6. References

[1] D.P. Woodruff, T.A. Delchar, Modern Techniques of Surface Science Second ed., Cambridge University Press, 1994.

[2] S.R. Andrews, R.A. Cowley, Scattering of X-rays from crystal surfaces, Journal of Physics C: Solid State Physics, 18 (1985) 6427.

[3] R. Feidenhans'l, Surface structure determination by X-ray diffraction, Surface Science Reports, 10 (1989) 105-188.

[4] I.K. Robinson, D.J. Tweet, Surface X-ray diffraction, Reports on Progress in Physics, 55 (1992) 599.

[5] H. Winick, A. Bienenstock, Synchrotron Radiation Research, Annual Reviews, 1978.

[6] P. Coppens, D. Cox, E. Vlieg, I.K. Robinson, Synchrotron radiation crystallography, Academic Press 1992.

[7] J. Als-Nielsen, D. McMorrow, Elements of Modern X-ray Physics Wiley 2001.

[8] G.A. Somorjai, Introduction to surface chemistry and Catalysis, John Wiley & Sons, 1994.

[9] B.E. Warren, X-ray Diffraction, Dover Publications, 1969.

[10] J.F. van der Veen, B. Schonfeld, Materials Research using Synchrotron Radiation, in, Paul Scherrer Institut, Zürich, 2013.

[11] R. Santra, Concepts in X-ray physics, Journal of Physics B: Atomic, Molecular and Optical Physics, 42 (2009).

[12] C.H. MacGillavry, G.D. Rieck, International Tables for X-ray Crystallography, Volume 3 (Physical & Chemical Tables) Kynoch Press, Birmingham, 1969.

[13] J. Rius, X. Torrelles, C. Miravitlles, Progress in powder and surface X-ray diffraction crystallography, Contributions to Science, 2 (2001) 95-103.

[14] D. Attwood, Soft X-rays and Extreme Ultraviolet Radiation: Principles and Applications, Cambridge University Press, 2007.

[15] H. Winick, S. Doniach, Synchrotron Radiation Research, Plenum press, 1980.

[16] Diamond Light Source, http://www.diamond.ac.uk, Diamond Light Source, 20/06/2012.

[17] C. Christou, K. Dunkel, C. Piel, V. Kempson The Pre-Injector LINAC for the Diamond Light Source, in: EPAC 2004, Germany, 2004.

[18] P. Kirkpatrick, A.V. Baez, Formation of Optical Images by X-rays, J. Opt. Soc. Am., 38 (1948) 766-773.

[19] J. Bloch, Angle and index calculations for `z-axis' X-ray diffractometer, Journal of Applied Crystallography, 18 (1985) 33-36.

[20] M. Lohmeier, E. Vlieg, Angle calculations for a six-circle surface X-ray diffractometer, Journal of Applied Crystallography, 26 (1993) 706-716.

[21] E. Vlieg, J.F. Van der Veen, J.E. Macdonald, M. Miller, Angle calculations for a five-circle diffractometer used for surface X-ray diffraction, Journal of Applied Crystallography, 20 (1987) 330-337.

[22] E. Vlieg, A (2+3)-Type Surface Diffractometer: Mergence of the z-Axis and (2+2)-Type Geometries, Journal of Applied Crystallography, 31 (1998) 198-203.

[23] O. Bunk, M.M. Nielsen, Angle calculations for a z-axis/(2S+2D) hybrid diffractometer, Journal of Applied Crystallography, 37 (2004) 216-222.

[24] E.P. Gibbons, M.T. Heron, N.P. Rees, GDA and EPICS Working in Unison for Science Driven Data Acquisition and Control at Diamond Light Source, in: 13th International Conference on Accelerator and Large Experimental Physics Control Systems (ICALEPCS 2011), Grenoble, France, 2011.

[25] C. Ponchut, F. Zontone, H. Graafsma, Experimental comparison of pixel detector arrays and CCD-based systems for X-ray area detection on synchrotron beamlines, in: Nuclear Science Symposium Conference Record, 2004 IEEE, 2004, pp. 4676-4680 Vol. 4677.

[26] X. Torrelles, J. Rius, Faster acquisition of structure-factor amplitudes in surface X-ray diffraction experiments, Journal of Applied Crystallography, 37 (2004) 395-398.

[27] E. Vlieg, ROD: a program for surface X-ray crystallography, Journal of Applied Crystallography, 33 (2000) 401-405.

[28] E. Vlieg, From beam time to structure factors, in, IMM Solid State Chemistry, Radboud University Nijmegen, Nijmegen, 2009.

[29] C.M. Schleputz, R. Herger, P.R. Willmott, B.D. Patterson, O. Bunk, C. Bronnimann, B. Henrich, G. Hulsen, E.F. Eikenberry, Improved data acquisition in grazing-incidence X-ray scattering experiments using a pixel detector, Acta Crystallographica Section A, 61 (2005) 418-425.

[30] D.W. Marquardt, An Algorithm for Least-Squares Estimation of Nonlinear Parameters, Journal of the Society for Industrial and Applied Mathematics, 11 (1963) 431-441.

[31] A. Chambers, Basic Vacuum Technology, 2nd edition, Taylor & Francis, 1998.

[32] K. Besocke, An easily operable scanning tunneling microscope, Surface Science, 181 (1987) 145-153.

[33] J. Frohn, J.F. Wolf, K. Besocke, M. Teske, Coarse tip distance adjustment and positioner for a scanning tunneling microscope, Review of Scientific Instruments, 60 (1989) 1200-1201.

[34] RHK Technologies, UHV 300 User's Guide, in, Rochester Hills, Michigan USA, 1998.

[35] RHK Technology, www.rhk-tech.com, in, 2013.

[36] G. Binnig, H. Rohrer, C. Gerber, E. Weibel, Tunneling through a controllable vacuum gap, Applied Physics Letters, 40 (1982) 178-180.

[37] G. Binnig, H. Rohrer, C. Gerber, E. Weibel, Surface Studies by Scanning Tunneling Microscopy, Physical Review Letters, 49 (1982) 57-61.

[38] C. Gerber, H.P. Lang, How the doors to the nanoworld were opened, Nat Nano, 1 (2006) 3-5.

[39] R. Wiesendanger, Scanning Probe Microscopy and Spectroscopy: Methods and Applications, Cambridge University Press, 1994.

[40] I. Horcas, R. Fernandez, J.M. Gomez-Rodriguez, J. Colchero, J. Gomez-Herrero, A.M. Baro, WSXM: A software for scanning probe microscopy and a tool for nanotechnology, Review of Scientific Instruments, 78 (2007) -.

[41] G. Binnig, H. Rohrer, C. Gerber, E. Weibel, 7×7 Reconstruction on Si(111) Resolved in Real Space, Physical Review Letters, 50 (1983) 120-123.

[42] J. Frenkel, On the Electrical Resistance of Contacts between Solid Conductors, Physical Review, 36 (1930) 1604-1618.

[43] G. Friedbacher, H. Bubert, Surface and Thin Film Analysis: A Compendium of Principles, Instrumentation, and Applications, Wiley, 2011.

[44] G. Binnig, D.P.E. Smith, Single-tube three-dimensional scanner for scanning tunneling microscopy, Review of Scientific Instruments, 57 (1986) 1688-1689.

[45] K.S. Birdi, Scanning Probe Microscopes: Applications in Science and Technology, CRC Press, 2003.

[46] S.Ä. Park, C.F. Quate, Scanning tunneling microscope, Review of Scientific Instruments, 58 (1987) 2010-2017.

[47] A. Cricenti, E. Paparazzo, M.A. Scarselli, L. Moretto, S. Selci, Preparation and characterisation of tungsten tips for scanning tunneling microscopy, Review of Scientific Instruments, 65 (1994) 1558-1560.

[48] J.P. Ibe, J.P.P. Bey, S.L. Brandow, R.A. Brizzolara, N.A. Burnham, D.P. DiLella, K.P. Lee, C.R.K. Marrian, R.J. Colton, On the electrochemical etching of tips for scanning tunneling microscopy, Journal of Vacuum Science & Technology A: Vacuum, Surfaces, and Films, 8 (1990) 3570-3575.

[49] Y.-C. Kim, D. Seidman, An electrochemical etching procedure for fabricating scanning tunneling microscopy and atom-probe field-ion microscopy tips, Met. Mater. Int., 9 (2003) 399-404.

[50] C. Davisson, L.H. Germer, Diffraction of Electrons by a Crystal of Nickel, Physical Review, 30 (1927) 705-740.

[51] L.J. Clarke, Surface crystallography: an introduction to low energy electron diffraction, Wiley, 1985.

[52] L. de Broglie, Annales de Physique, 3 (1925) 22.

[53] J.C. Vickerman, I. Gilmore, Surface Analysis: The Principal Techniques, Wiley, 2009.

[54] C.C. Chang, Auger electron spectroscopy, Surface Science, 25 (1971) 53-79.

[55] Pierre Auger, The compound photoelectric effect - Sur l'effet photoélectrique composé, Journal de Physique et le Radium, 6 (1925) 205.

[56] J.J. Lander, Auger Peaks in the Energy Spectra of Secondary Electrons from Various Materials, Physical Review, 91 (1953) 1382-1387.

[57] L. E. Davis, N. C. MacDonald, P. W. Palmberg, G.E. Riach, R.E. Weber, Handbook of Auger Electron Spectroscopy, Physical Electronics Industries, 1976.

[58] O. Bikondoa, Structural properties of oxide thin films on alloys, in, Euskal Herriko Unibertsitatea 2003.

[59] P.W. Palmberg, G.K. Bohn, J.C. Tracy, High Sensitivty Auger Electron Spectrometer, Applied Physics Letters, 15 (1969) 254-255.

[60] G. Binnig, C.F. Quate, C. Gerber, Atomic Force Microscope, Physical Review Letters, 56 (1986) 930-933.

[61] G. Binnig, C. Gerber, E. Stoll, T.R. Albrecht, C.F. Quate, Atomic Resolution with Atomic Force Microscope, EPL (Europhysics Letters), 3 (1987) 1281.

[62] G. Meyer, N.M. Amer, Erratum: Novel optical approach to atomic force microscopy [Appl. Phys. Lett. 53, 1045 (1988)], Applied Physics Letters, 53 (1988) 2400-2402.

[63] N. Jalili, K. Laxminarayana, A review of atomic force microscopy imaging systems: application to molecular metrology and biological sciences, Mechatronics, 14 (2004) 907-945.

[64] Digital Instruments, Command reference Manual, Santa Barbara, California, USA, 1996.

[65] P.G. de Gennes, Wetting: statics and dynamics, Reviews of Modern Physics, 57 (1985) 827-863.

[66] T. Young, An Essay on the Cohesion of Fluids, Philosophical Transactions of the Royal Society of London, 95 (1805) 65.

[67] G. Bracco, B. Holst, Surface Science Techniques, Springer, 2013.

[68] R.J. Good, Contact angle, wetting, and adhesion: a critical review, Journal of Adhesion Science and Technology, 6 (1992) 1269-1302.

[69] A.W. Neumann, R.J. Good, Techniques of Measuring Contact Angles, in: R. Good, R. Stromberg (Eds.) Surface and Colloid Science, Springer US, 1979, pp. 31-91.

[70] H.W. Fox, W.A. Zisman, The spreading of liquids on low energy surfaces. I. polytetrafluoroethylene, Journal of Colloid Science, 5 (1950) 514-531.

[71] S. Srinivasan, G.H. McKinley, R.E. Cohen, Assessing the Accuracy of Contact Angle Measurements for Sessile Drops on Liquid-Repellent Surfaces, Langmuir, 27 (2011) 13582-13589.

[72] First Ten Angstroms, http://www.firsttenangstroms.com, in, 2013.

[73] H.-J. Freund, Introductory Lecture: Oxide surfaces, Faraday Discussions, 114 (1999) 1-31.

[74] B. Dupoisson, P. Dumas, A. Steinbrunn, J.C. Colson, Single crystal cleavage device adaptable to a UHV vessel, Journal of Physics E: Scientific Instruments, 9 (1976) 266.

[75] F.P. Netzer, M. Prutton, LEED and electron spectroscopic observations on NiO (100), Journal of Physics C: Solid State Physics, 8 (1975) 2401.

[76] C.L. Pang, R. Lindsay, G. Thornton, Structure of Clean and Adsorbate-Covered Single-Crystal Rutile TiO_2 Surfaces, Chemical Reviews, 113 (2013) 3887-3948.

[77] Y. Namai, O. Matsuoka, NC-AFM Observation of Atomic Scale Structure of Rutile-type TiO_2(110) Surface Prepared by Wet Chemical Process, The Journal of Physical Chemistry B, 110 (2006) 6451-6453.

[78] Y. Yamamoto, K. Nakajima, T. Ohsawa, Y. Matsumoto, H. Koinuma, Preparation of Atomically Smooth TiO_2 Single Crystal Surfaces and Their Photochemical Property, Japanese Journal of Applied Physics, 44 (2005) L511-L514.

Chapter 3

Metal Oxide Surfaces

3.1. Introduction

The technological and scientific importance of studying metal oxide surfaces has been discussed in some detail in Chapter 1. In the present chapter, an introduction is provided to the substrate materials studied and described in the experimental sections of this thesis, namely rutile TiO_2 and its (110) and (011) surfaces and α-Cr_2O_3 and its (0001) surface. The bulk structure, surface structure, and the pertinent physical and chemical properties of these materials are discussed. For more extensive reviews of the surface science of TiO_2 the reader is referred to References [1, 2]. However, due to the relative lack of comprehensive reviews on α-Cr_2O_3, the reader is referred to the references cited throughout the course of this chapter to provide further insight into the surface structure and properties α-Cr_2O_3.

3.2. Titanium Dioxide (TiO_2)

Given the great importance of the chemical and physical surface properties of titanium dioxide (TiO_2) to a variety of technologies and commercially significant applications, it comes as no surprise that there has been a tremendous drive towards further research into this material. The applications include photo-catalysts [3-5], solar cell devices, white pigmentation for paints, oxygen gas sensors to control the air/fuel mixture in automotive engines [6], and surface films on metallic titanium substrates such as medical implants to provide corrosion resistance and biocompatibility [7]. Research activity extends from development of novel TiO_2-based structures, such as nano-tubes, to fundamental studies of model single crystal surfaces with the aim of gaining a mechanistic insight into surface processes. The latter effort has typically been concerned with studies of model low Miller index single-crystal TiO_2 surfaces under ultra-high vacuum (UHV) conditions. To date, the vast majority of these types of studies have been conducted on the rutile $TiO_2(110)$ surface, which has become the prototypical substrate for fundamental UHV studies of metal oxides [2].

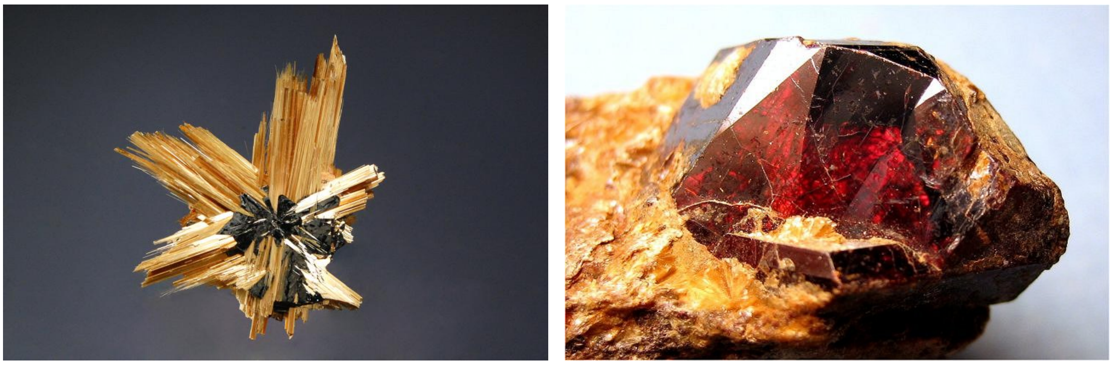

Figure 3.1: Examples of naturally occurring rutile (TiO_2), the colour of which can range from yellow or rusty yellow as inclusions or in thin slender needle like crystals to reddish brown or black with a submetallic lustre in large thick crystals.

Although naturally occurring crystalline TiO_2 is essentially pure titanium dioxide, it often appears coloured due to the presence of impurities, such as iron, chromium, or vanadium. Figure 3.1 shows images of naturally occurring TiO_2. Commercially available single crystal stoichiometric titanium dioxide is transparent.

3.2.1. Bulk Structure of TiO_2

Titanium dioxide exists in nature in one of three crystalline forms, namely rutile, anatase, or brookite. All three phases are stable at atmospheric pressure. In the work for this thesis, experiments were carried out on the rutile form of TiO_2. Figure 3.2 shows the bulk rutile unit cell. The bulk structure has a tetragonal unit cell with dimensions $a = b = 4.587$ Å and $c = 2.953$ Å, and $\alpha = \beta = \gamma = 90°$ [1]. The basic building block of the bulk structure consists of a titanium atom bonded to six neighbouring three-fold coordinated oxygen atoms to form a slightly distorted TiO_6 octahedron. This distorted octahedral structure results in two slightly longer Ti – O bonds, titanium is coordinated to four oxygen atoms at a bond length of 1.946 Å and to two oxygen atoms at the apices of the octahedron at a Ti – O bond length of 1.983 Å [1].

Stoichiometric TiO_2 is a large band gap (3 eV) insulator. However, high temperature annealing results in the creation of titanium interstitials, which in effect increases bulk conductivity thus providing the means of using surface science techniques that require conductive samples, such scanning tunneling microscopy, to study TiO_2.

TiO_2 surfaces in general and more specifically the low Miller index rutile TiO_2 surfaces have attracted much attention in the world of surface science over the years This is partly due to their suitability for many surface specific experimental techniques, the capacity to prepare a well-defined surface reproducibly and the fact that high-quality single crystals in varying sample sizes and thicknesses are readily available in cut and polished forms from a number of commercial companies across the world .

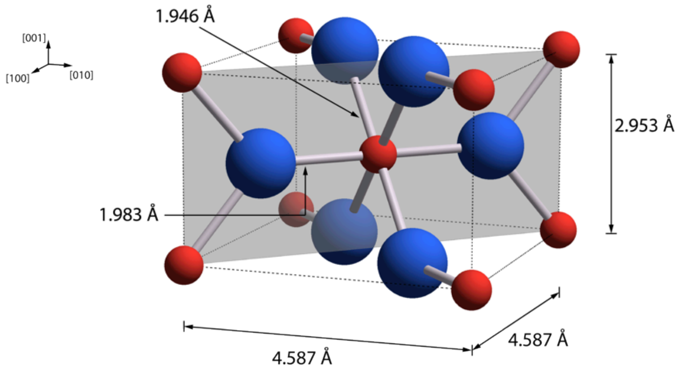

Figure 3.2: A ball and stick model of the bulk rutile TiO_2 unit cell. Large blue (small red) spheres represent oxygen (titanium) atoms. Also shown in shaded grey is the intersection of the (110) plane with the bulk unit cell.

3.2.2. TiO_2(110)-(1×1)

The bulk truncated rutile TiO_2 (110)-(1×1) surface is the most stable crystal face of TiO_2, and as indicated previously, is the most studied low Miller index single-crystal metal oxide surface [1, 2]. Figure 3.3 displays a space filling model of the ideal bulk terminated TiO_2(110)-(1×1) surface. The (110) 1×1 surface unit cell is denoted by the superimposed rectangle, measuring 6.495 Å by 2.959 Å. The surface structure at the solid-vacuum interface consists of a topmost layer of so-called 2-fold bridging oxygen atom (O_b) rows running along the [001] direction; titanium atoms underneath these bridging oxygen atoms are 6-fold coordinated. Within the main surface plane, parallel with, and equidistant between neighboring bridging oxygen rows is a row of 5-fold coordinated titanium atoms (Ti_{5c}). Both the 5 and 6-fold titanium atoms coordinate to 3-fold coordinated in-plane oxygen atoms.

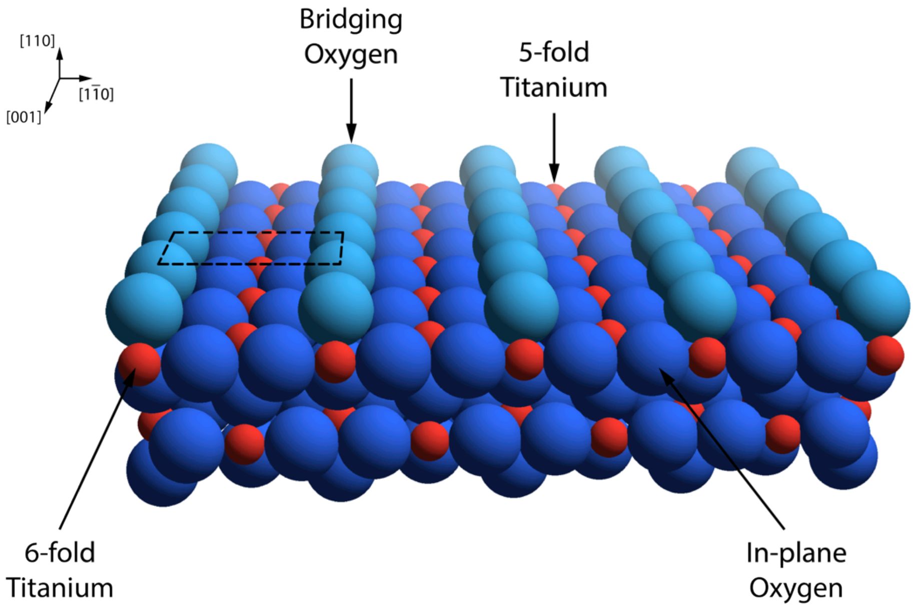

Figure 3.3: Space-filling model of ideal bulk-terminated TiO_2(110)-(1×1). Large blue (small red) spheres are oxygen (titanium) atoms. The dashed black rectangle indicates the (1×1) surface unit cell.

Typically, a very sharp well-defined (1×1) LEED pattern with a low background is easily observed following UHV surface preparation comprising of standard inert gas ion bombardment and annealing cycles [1, 2]. Fully quantitative surface structure determination studies employing various quantitative probing techniques [8-12] have found that the structure of this UHV prepared surface is very similar to the bulk truncated model depicted in Figure 3.3. However, the surface does undergo some relaxation. Table 3.1 lists the optimised atomic displacements away from the ideal bulk terminated TiO_2 (110)-(1×1) surface corresponding to the proposed surface structures from various recent experimental studies. Figure 3.4 shows a ball and stick model of the bulk truncated TiO_2 (110)-(1×1) surface, the numerical labeling of atoms is the same as that employed in Table 3.1. From the most complete fully quantitative structure determinations to date, employing LEED-IV by Lindsay *et al* [9] and SXRD by Cabailh *et al* [10], relaxation of surface atoms due to the loss of three-dimensional periodicity are reported. Indeed the optimized surface structures from the LEED-IV and SXRD studies are impressively consistent, with almost all atomic displacements being essentially identical. It is found, as expected from symmetry, that most relaxation occurs perpendicular to the surface. Lateral relaxations are observed only for the in-plane oxygen atoms, which move towards the 5-fold titanium atoms. A downward relaxation of the 5-fold titanium atoms (Ti(2)) is reported and the neighbouring 3-fold oxygen atoms (O(2) and O(2*)) move upwards, resulting in the rumpled appearance of the surface. The 6-fold titanium atoms (Ti(1)) are observed to displace outwards. Most notably the bridging oxygens (O (1)) are found, in these studies, to relax away from the bulk by 0.1 ± 0.05 Å (LEED-IV)/ 0.1 ± 0.04 Å (SXRD).

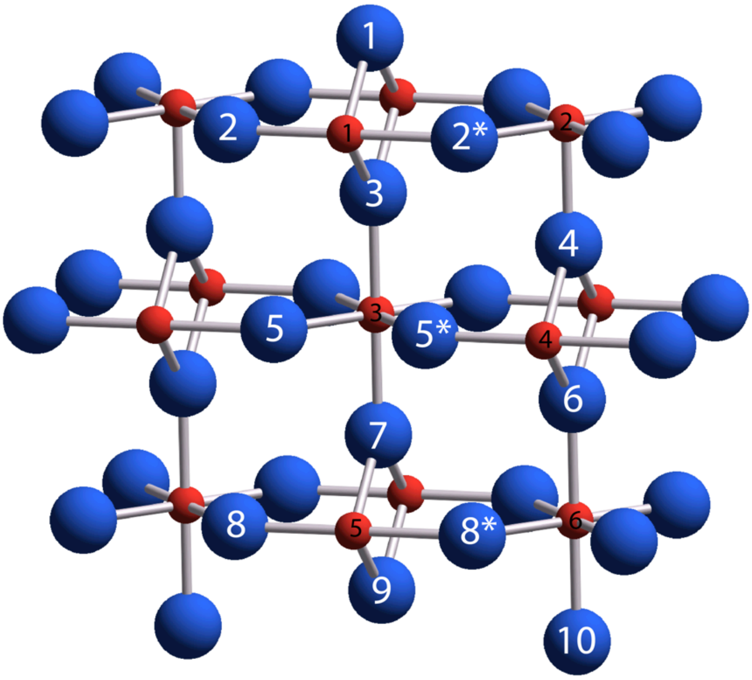

Figure 3.4: A ball and stick model of the bulk truncated TiO_2(110)-(1×1) surface. Large blue (small red) spheres are oxygen (titanium) atoms. Numerical labeling of the atoms is provided as a key for Table 3.1. All symmetry paired atoms are denoted by an asterisk (*).

Optimum structural information from other recent experimental determinations are also listed in Table 3.1, specifically from medium energy ion scattering (MEIS) measurements by Parkinson *et al* [11] and photoelectron diffraction (PhD) by Kroger *et al* [12]. These show generally good agreement with the optimum structures from LEED-IV and SXRD. The overall excellent level of quantitative agreement of the optimized atomic displacements between these recent studies has settled an ongoing uncertainty over the relaxation of the bridging oxygen (O(1)), now established to be a displacement of ~ 0.1 Å away from the bulk.

Table 3.1: Experimentally determined atomic displacements away from bulk-terminated $TiO_2(110)$-(1×1) obtained from analysis of SXRD [10], LEED-IV [9] , MEIS [11] and PhD [12] Studies. The numerical labelling of atoms corresponds to that in Fig. 4.4. The positive (negative) values define a movement away (toward) the bulk. The $[1\bar{1}0]$ direction defines the positive lateral movement.

	Atomic displacements (Å)			
Atom	SXRD [10]	LEED-IV [9]	MEIS [11]	PhD [12]
O(1)	0.10 ± 0.04	0.10 ± 0.05	0.13 ± 0.16	0.17 ± 0.15
O(2) [110]	0.17 ± 0.03	0.27 ± 0.08	0.05	0.00 (0.40/0.15)
O(2) $[1\bar{1}0]$	0.01 ± 0.05	0.17 ± 0.15	0.00	0.05 ± 0.15
Ti(1)	0.25 ± 0.01	0.25 ± 0.03	0.19 ± 0.07	0.19 (0.15/ 0.10)
Ti(2)	0.11 ± 0.01	0.19 ± 0.03	0.09 ± 0.09	0.26 ± 0.08
O(3)	0.07 ± 0.04	0.06 ± 0.10	0.10 ± 0.13	0.15 ± 0.15
O(4)	0.00 ± 0.03	0.00 ± 0.08	-	0.03 ± 0.08
O(5) [110]	0.04 ± 0.03	0.06 ± 0.12	-	-
O(5) $[1\bar{1}0]$	0.05 ± 0.05	0.07 ± 0.18	-	-
Ti(3)	0.08 ± 0.01	0.09 ± 0.07	0.09 ± 0.09	0.21 (0.40/0.15)
TI(4)	0.19 ± 0.01	0.14 ± 0.05	0.06 ± 0.06	0.15 (0.20/0.15)
O(6)	0.01 ± 0.04	0.00 ± 0.17	-	-
O(7)	0.01 ± 0.04	0.01 ± 0.13	-	-
O(8) [110]	0.01 ± 0.03	0.03 ± 0.11	-	-
O(8) $[1\bar{1}0]$	-0.03±0.05	-0.03 ± 0.26	-	-
Ti(5)	0.08 ± 0.01	0.06 ± 0.09	0.00 ± 0.07	-
TI(6)	-0.04 ± 0.01	-0.07 ± 0.07	-0.02 ± 0.08	-
O(9)	0.02 ± 0.04	0.13 ± 0.56	-	-
O(10)	-0.02 ± 0.04	-0.02 ± 1.70	-	-

3.2.3. $TiO_2(011)$

Given the tetragonal rutile TiO_2 bulk unit cell, the (011) and (110) faces are not identical [13]. Depicted in Figure 3.5 is a shaded region indicating the (011) plane within the bulk rutile TiO_2 unit cell.

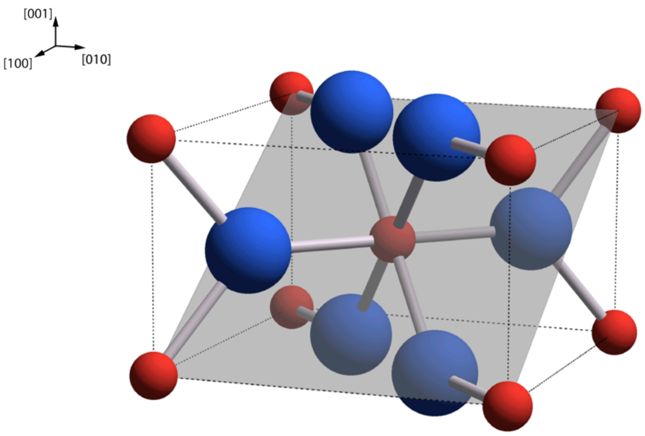

Figure 3.5: Schematic representation of the intersection of the (011) plane with the bulk rutile TiO_2 unit cell. Large blue (small red) spheres are oxygen (titanium) atoms.

The bulk terminated TiO_2(011)-(1×1) surface, shown in Figure 3.6 complete with labeling of the topmost atoms, consists of exposed 2-fold coordinated bridging oxygen atoms (O_{2c}) at the apices, 5-fold coordinated titanium atoms (Ti_{5c}) at each side and bulk-like 3-fold coordinated oxygen atoms (O_{3c}) in the valleys. However this surface termination has never been observed experimentally; instead, the surface atoms form a very stable 2×1 reconstruction in vacuum.

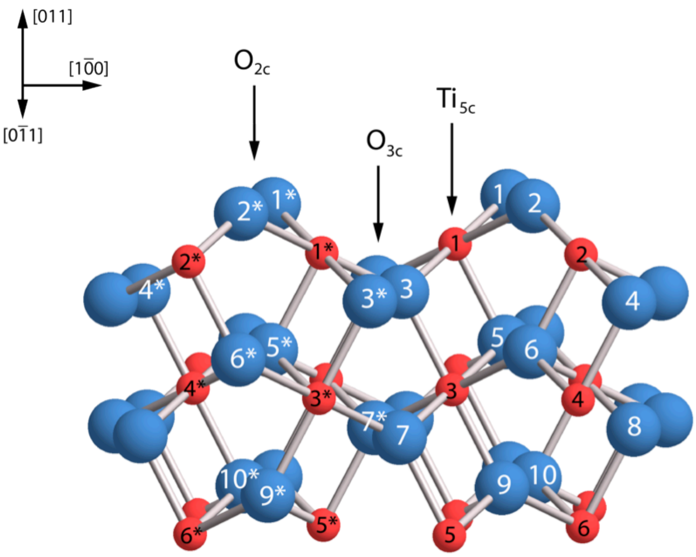

Figure 3.6: A ball and stick model of the ideal bulk truncated TiO_2(011)-(1×1) surface. Large blue (small red) spheres are oxygen (titanium) atoms. Numerical labeling of the atoms is provided as a key for Table 3.2. All symmetry paired atoms are denoted by an asterisk (*).

A number of experimental studies in combination with first-principles total energy calculations have been performed to explore both the structure and reactivity of this surface. Initially, on the basis of *ab initio* calculations alongside STM data, Beck *et al* [14] concluded that the surface reconstructed to a stoichiometric (2×1) unit cell terminated by titanyl (Ti=O) groups. In this study the titanyl group was presumed to appear as the zigzag pattern of bright spots apparent in high-resolution STM images. Interestingly, as this termination had never been seen on other TiO_2 surfaces, they suggested that the presence of these titanyl double bonds could provide an explanation for the enhanced photoactivity of the TiO_2(011) surface [15]. However, a more recent combined NC-AFM, STM and *ab initio* calculation study by Kubo *et al* [16] paints a completely different picture. Although they confirm a 2×1 reconstruction, the surface termination proposed is somewhat different, involving a 'microfaceted' missing-rows model where the removal of a pair of apex Ti_{5c}-O_{2c} gives rise to the 2×1 surface periodicity. Kubo *et al* on the basis of their own DFT calculations reject the solution of Beck *et al* suggesting that the unsaturated dangling bonds of the Ti atom in the titanyl group would bond with the nearest-neighbour bridging oxygen atoms inducing large distortions in the surface and subsurface layers, ultimately concluding that this type of bonding would result in an energetically less stable surface.

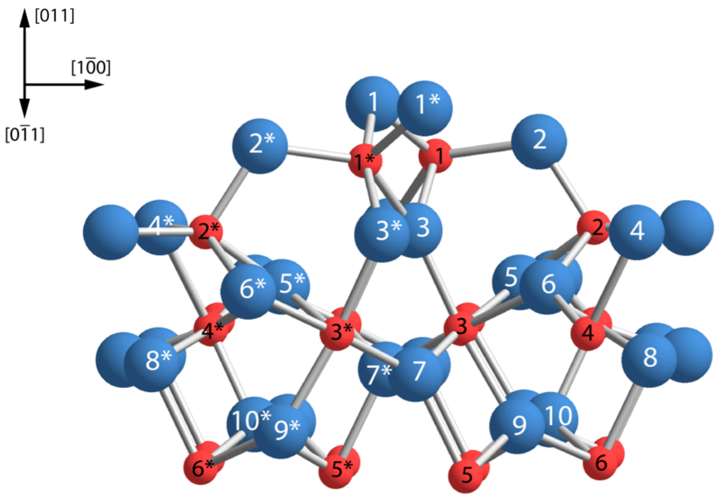

Figure 3.7: Ball and stick models depicting the optimum TiO_2(011)-(2×1) geometry as deduced from SXRD [17, 18] and LEED-IV [19]. Large blue (small red) spheres are oxygen (titanium) atoms. Numerical labeling of the atoms is provided as a key for Table 3.2. All symmetry paired atoms are denoted by an asterisk (*).

Table 3.2: Optimized atomic displacements for the TiO_2(011)-(2×1) reconstruction resulting from recent SXRD [17, 18] and LEED-IV [19] data, expressed as displacements away from the bulk-terminated TiO_2(011)-(1×1) surface. (x, y, z) atomic coordinates for the bulk-terminated structure of TiO_2(011)-(1×1) are also listed. A positive value for x, y, z indicates a displacement in the $[\bar{1}00]$, $[01\bar{1}]$ and [011] directions, respectively. Figures 3.6 and 3.7 provide keys to the identity of the individual atoms.

Atom	(1×1) bulk terminated (x, y, z) coordinates (Å)	Atomic displacements (Å)								
		SXRD [18]			SXRD [17]			LEED-IV [19]		
		Δx	Δy	Δz	Δx	Δy	Δz	Δx	Δy	Δz
O(1)	(2.04, 0.00, 0.76)	-2.52	2.90	0.62	-2.20	2.71	0.63	-2.61	2.99	0.82
O(2)	(2.55, 2.73, 0.76)	-0.15	-0.29	-0.06	-0.18	-0.28	-0.08	-0.18	-0.26	-0.21
Ti(1)	(1.15, 1.56, 0.00)	-0.56	0.32	0.43	-0.62	0.32	0.39	-0.47	0.39	0.36
Ti(2)	(3.44, 4.28, 0.00)	-0.09	-1.76	-0.80	-0.14	-1.77	-0.77	0.02	-1.75	-0.73
O(3)	(0.25, 3.11, -0.76)	0.00	0.27	-0.06	-0.27	0.27	-0.08	-0.09	0.31	-0.06
O(4)	(4.34, 5.84, -0.76)	-0.15	0.42	-0.01	0.20	0.58	-0.02	-0.27	0.35	-0.14
O(5)	(2.04, 1.61, -1.73)	0.00	-0.04	-0.06	-	-	-0.11	-	-	-0.09
O(6)	(2.44, 4.34, -1.73)	0.03	-0.27	-0.06	-	-	-0.03	-	-	-0.17
Ti(3)	(1.15, 3.16, -2.49)	-0.10	-0.05	-0.06	-	-	-0.12	-	-	-0.08
TI(4)	(3.44, 5.89, -2.49)	-0.12	-0.27	-0.07	-		-0.05	-	-	-0.05
O(7)	(0.25, 4.71, -3.25)	0.04	0.00	-0.05	-	-	-	-	-	-
O(8)	(4.34, 1.98, -3.25)	-0.02	0.07	0.12	-	-	-	-	-	-
O(9)	(2.04, 3.21, -4.22)	-0.02	-0.06	-0.04	-	-	-	-	-	-
O(10)	(2.55, 0.48, -4.22)	0.00	-0.03	0.00	-	-	-	-	-	-
Ti(5)	(1.15, 4.76, -4.98)	0.02	-0.06	-0.11	-	-	-	-	-	-
TI(6)	(3.44, 2.03, -4.98)	0.01	0.04	0.05	-	-	-	-	-	-

Given this apparent controversy over the TiO_2(011)-(2×1) surface geometry, fully quantitative surface structure determination studies, namely SXRD by Torrelles *et al* [18] and LEED-IV by Chamberlin *et al* [19], were carried out to settle the debate, concluding that neither of the previous combined SPM and *ab initio* calculations based models was correct. These findings and the resulting optimised structure were further confirmed through the latest STM measurements in combination with SXRD data and DFT calculations by Gong *et al* [17]. Figure 3.7, shows a ball and stick model of the optimised TiO_2(011)-(2×1) geometry emerging from these studies in which the surface is terminated by 2-fold coordinated oxygen atoms in a zig-zag arrangement that bind asymmetrically to the underlying 5-fold coordinated titanium atoms. Most notably, only local atomic displacements are required to form this reconstruction and thus the surface has the same stoichiometry as the underlying substrate. In this optimised solution the topmost oxygen atoms O(1) and O(1*) form different bond lengths from each other with the underlying 5-fold coordinated titanium atoms creating the zig-zag rows observed in STM. The optimised structures determined in these three experimental studies are detailed in Table 3.2, where the atomic displacements (Δx, Δy, Δz) away from the ideal bulk terminated TiO_2(011)-(1×1) surface are listed. The Labelled ball and stick models of the surface in Figures 3.6 (ideal 1×1) and Figure 3.7 (2×1 reconstruction) facilitate identification of the atoms in Table 3.2.

3.3. Chromium (III) Dioxide (Cr_2O_3)

The alpha phase of chromium (III) oxide, also commonly known as the mineral eskolaite, has a wide variety of industrial and technological applications due to its unique chemical and physical properties. The importance of Cr_2O_3 in various applications, including heterogeneous catalysis, functioning as a binder layer in the production of magnetic recording media, and as the main constituent behind the corrosion control of stainless steels [20], has been the driving force behind many fundamental experimental surface investigations.

3.3.1. Bulk Structure of Cr_2O_3

Among the different chromium oxide solid phases, Cr_2O_3 is the most stable, existing over a wide range of temperatures and pressures. Bulk Cr_2O_3 has a corundum type structure made up of six oxygen stacking sub-layers and twelve single (six double) chromium sub-layers along the c-axis of the hexagonal lattice (unit cell dimensions: $a = b = 4.957$ Å, $c = 13.592$ Å, and $\gamma = 120°$ [21]). Cr_2O_3 is electrically insulating with a band gap of 3.4 eV. Figure 3.8 shows a ball and stick model representation of the bulk Cr_2O_3 unit cell along a direction perpendicular to (0001) plane, also shown is the intersection of the (0001) face with the bulk Cr_2O_3 unit cell.

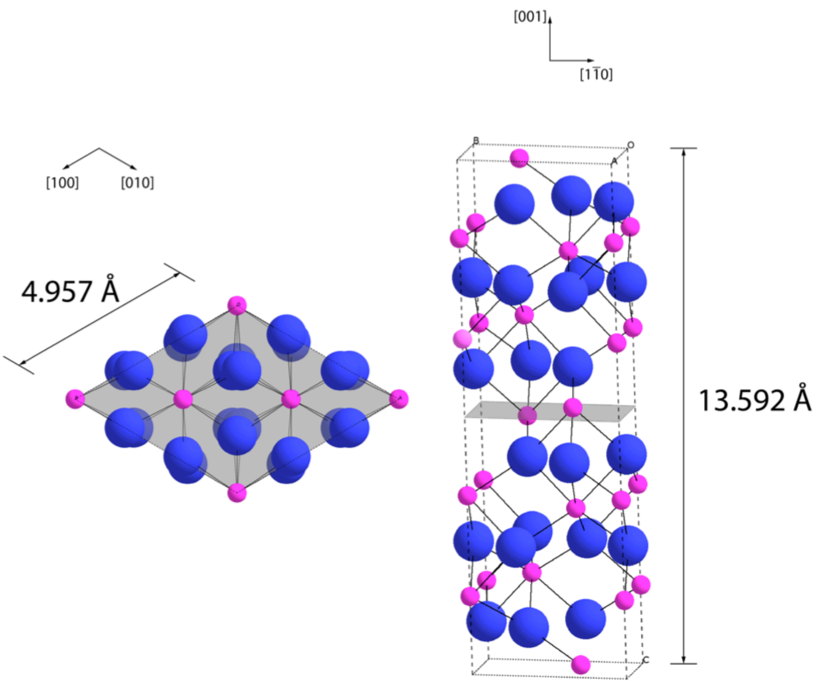

Figure 3.8: Ball and stick models of the bulk Cr_2O_3 hexagonal unit cell. Top view (left) of the Cr_2O_3 unit cell, also shown (right) is the intersection of the (0001) plane with the bulk Cr_2O_3 unit cell. Large blue (small purple) spheres are oxygen (chromium) atoms.

The bulk corundum structure consists of a hexagonally close packed sublattice of O^{2-} anions in a distorted octahedral arrangement with six-fold coordinated Cr^{3+} cations occupying two of three possible octahedral sites. This arrangement leads to a surface unit cell size of 4.957 Å × 4.957 Å. The bulk oxygen anions within the basal (0001) plane deviate slightly from the ideal arrangement and form distorted octahedra. This divergence from octahedral symmetry results in three slightly longer chromium – oxygen bonds at a bond length of 2.016 Å and three shorter bonds at a Cr – O bond length of 1.965 Å.

For Cr_2O_3, the two most studied surface terminations are the (0001) and the (0112). Given the direct relevance of (0001) surface to this thesis, the remaining discussion in this chapter will focus on Cr_2O_3(0001)-(1×1).

3.3.2. α-Cr_2O_3(0001)

Figure 3.9 shows (left) a space-filling top view model of the ideal bulk truncated (0001) surface of stoichiometric Cr_2O_3 terminated by a double Cr ion layer, also displayed (right) is a ball and stick model representing the arrangement of atoms perpendicular to (0001) plane. This is not a cleavage surface, but can be obtained by cutting and polishing.

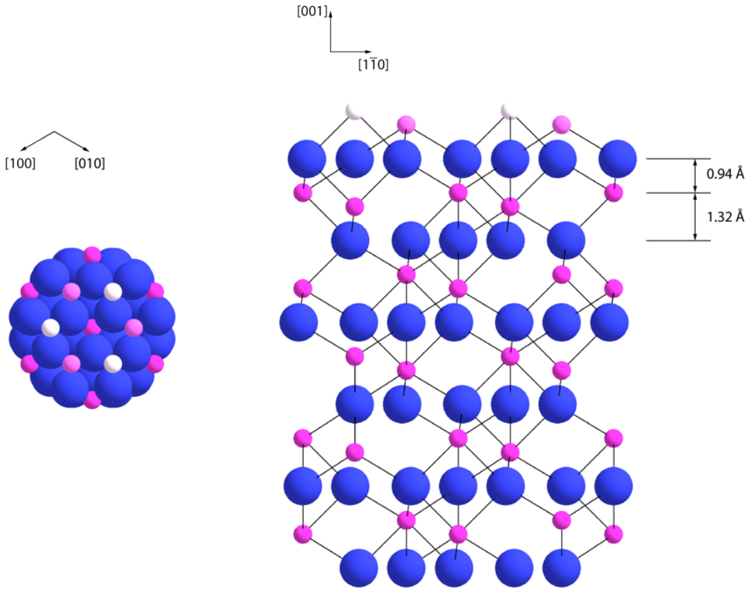

Figure 3.9: (left) Space filling top view model of the Cr_2O_3(0001) surface terminated by a full Cr ion layer alongside (right) a schematic representation of the stacking of oxygen and chromium atoms in Cr_2O_3 along on the (0001) direction into the bulk volume. Large blue (small purple) spheres are oxygen (chromium) atoms.

The Cr_2O_3(0001) surface has been the subject of several quantitative structure determinations in UHV, using both oriented thin film [5-7] and single crystal substrates [8,9]. Given the nature of the Cr_2O_3 unit cell, three ideal bulk truncated (0001) surface terminations are possible, namely a single metal layer termination (Cr-O_3-Cr-), a double metal layer termination (Cr-Cr-O_3-), and a close packed oxygen termination (O_3-Cr-Cr-) (the subscript indicates the average number of atoms in one 1×1 unit cell). These three surface terminations can be generated simply by cutting through the Cr_2O_3 bulk unit cell parallel to the (0001) plane, and are depicted in Figure 3.10. Interestingly, purely on the basis of electrostatics, both the double-metal layer and the close-packed oxygen layer terminations are deemed unstable due to the divergence of surface electrostatic potential [22, 23]. On the other hand, the Cr-O_3-Cr- termination (that can be envisaged by cutting in the middle of a double Cr layer such that only half of Cr ions from this layer remain at the surface) is expected to be energetically favourable. This termination for stoichiometric systems does not lead to divergence of the surface potential and, indeed, the vast majority of previous experimental and theoretical studies concerned with a 1x1 surface unit cell concluded that the single metal layer termination is the most likely surface termination generated in ultra high vacuum. However, their structural solutions are not identical. The Cr-O_3-Cr- surface termination is favored by Rohr *et al* [22, 23] based on LEED-IV measurements and by Priyantha and Waddill [24] on basis of X-ray photoelectron diffraction data from thick films of Cr_2O_3(0001) grown on Ag(111) by serial deposition.

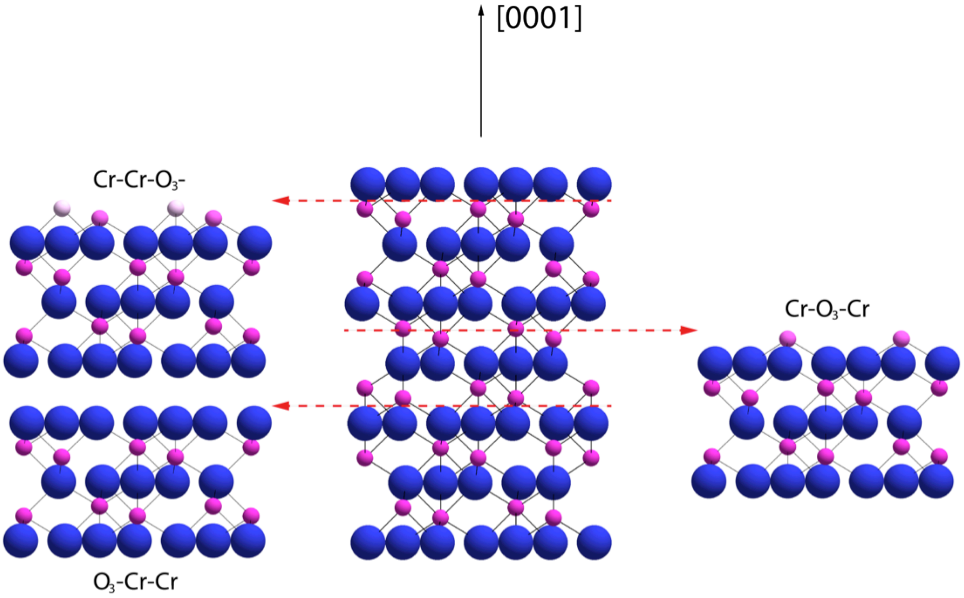

Figure 3.10: Schematic representation of the three bulk truncated surface terminations that can be generated simply by cutting through the α-Cr2O3 bulk parallel to the (0001) plane. Large blue (small purple) spheres are oxygen (chromium) atoms.

On the basis of SXRD measurements by Gloege *et al* [21], a surface geometry very similar to the Cr-O_3-Cr- termination, except that 30 % of the surface layer Cr atoms are in a sub-surface interstitial site (Cr^{int}), was deduced. This termination can be labeled as $Cr_{0.70}$-O_3-$Cr^{int}_{0.30}$.

Interestingly, more recent fully quantitative surface studies by Bikondoa *et al* [25] and by Lübbe and Moritz [26], employing SXRD and LEED-IV respectively, agree on a somewhat different termination to that previously cited. The proposed structure involves fractional occupied double Cr termination (Cr-Cr-O_3-), although some quantitative discrepancies between the two studies remain in terms of both site occupation and atomic coordinates. The solution of Bikondoa *et al* suggests a $Cr_{0.22}$-$Cr_{0.31}$-O_3- termination; where as Lübbe and Moritz propose a $Cr_{0.31}$-$Cr_{0.61}$-$O_{2.4}$- termination.

3.4. References

[1] U. Diebold, The surface science of titanium dioxide, Surface Science Reports, 48 (2003) 53-229.

[2] C.L. Pang, R. Lindsay, G. Thornton, Structure of Clean and Adsorbate-Covered Single-Crystal Rutile TiO_2 Surfaces, Chemical Reviews, 113 (2013) 3887-3948.

[3] O. Carp, C.L. Huisman, A. Reller, Photoinduced reactivity of titanium dioxide, Progress in Solid State Chemistry, 32 (2004) 33-177.

[4] A. Fujishima, K. Honda, Electrochemical Photolysis of Water at a Semiconductor Electrode, Nature, 238 (1972) 37.

[5] A. Fujishima, X. Zhang, D. Tryk, TiO2 photocatalysis and related surface phenomena, Surface Science Reports, 63 (2008) 515-582.

[6] Y. Xu, K. Yao, X. Zhou, Q. Cao, Platinum-titania oxygen sensors and their sensing mechanisms, Sensors and Actuators B: Chemical, 14 (1993) 492-494.

[7] F. Rupp, J. Geis-Gerstorfer, K.E. Geckeler, Dental implant materials: Surface modification and interface phenomena, Advanced Materials, 8 (1996) 254-257.

[8] G. Charlton, P.B. Howes, C.L. Nicklin, P. Steadman, J.S.G. Taylor, C.A. Muryn, S.P. Harte, J. Mercer, R. McGrath, D. Norman, T.S. Turner, G. Thornton, Relaxation of TiO_2(110)(1×1) Using Surface X-ray Diffraction, Physical Review Letters, 78 (1997) 495-498.

[9] R. Lindsay, A. Wander, A. Ernst, B. Montanari, G. Thornton, N.M. Harrison, Revisiting the Surface Structure of TiO_2(110): A Quantitative low-Energy Electron Diffraction Study, Physical Review Letters, 94 (2005) 246102.

[10] G. Cabailh, X. Torrelles, R. Lindsay, O. Bikondoa, I. Joumard, J. Zegenhagen, G. Thornton, Geometric structure of TiO_2(110)(1×1): Achieving experimental consensus, Physical Review B, 75 (2007) 241403.

[11] G.S. Parkinson, M.A. Munoz-Marquez, P.D. Quinn, M.J. Gladys, R.E. Tanner, D.P. Woodruff, P. Bailey, T.C.Q. Noakes, Medium-energy ion-scattering study of the structure of clean TiO_2(110)-(1×1), Physical Review B, 73 (2006) 245409.

[12] E.A. Kroger, D.I. Sayago, F. Allegretti, M.J. Knight, M. Polcik, W. Unterberger, T.J. Lerotholi, K.A. Hogan, C.L.A. Lamont, D.P. Woodruff, Photoelectron diffraction investigation of the structure of the clean TiO_2(110)(1×1) surface, Physical Review B, 75 (2007) 195413.

[13] O. Dulub, C.D. Valentin, A. Selloni, U. Diebold, Structure, defects, and impurities at the rutile TiO_2(011)-(2×1) surface: A scanning tunneling microscopy study, Surface Science, 600 (2006) 4407-4417.

[14] T.J. Beck, A. Klust, M. Batzill, U. Diebold, C. Di Valentin, A. Selloni, Surface Structure of TiO_2(011)-(2×1), Physical Review Letters, 93 (2004) 036104.

[15] T. Ohno, K. Sarukawa, M. Matsumura, Crystal faces of rutile and anatase TiO_2 particles and their roles in photocatalytic reactions, New Journal of Chemistry, 26 (2002) 1167-1170.

[16] T. Kubo, H. Orita, H. Nozoye, Surface Structures of Rutile TiO_2(011), Journal of the American Chemical Society, 129 (2007) 10474-10478.

[17] X.-Q. Gong, N. Khorshidi, A. Stierle, V. Vonk, C. Ellinger, H. Dosch, H. Cheng, A. Selloni, Y. He, O. Dulub, U. Diebold, The 2×1 reconstruction of the rutile TiO_2(011) surface: A combined density functional theory, X-ray diffraction, and scanning tunneling microscopy study, Surface Science, 603 (2009) 138-144.

[18] X. Torrelles, G. Cabailh, R. Lindsay, O. Bikondoa, J. Roy, J. Zegenhagen, G. Teobaldi, W.A. Hofer, G. Thornton, Geometric Structure of TiO_2(011)(2×1), Physical Review Letters, 101 (2008) 185501.

[19] S.E. Chamberlin, C.J. Hirschmugl, H.C. Poon, D.K. Saldin, Geometric structure of TiO_2(011)(2×1) surface by low energy electron diffraction (LEED), Surface Science, 603 (2009) 3367-3373.

[20] P. Marcus, V. Maurice, Corrosion and Environmental Degradation, First ed., Wiley, 1999.

[21] T. Gloege, H.L. Meyerheim, W. Moritz, D. Wolf, X-ray structure analysis of the Cr_2O_3(0001)-(1×1) surface: evidence for Cr interstitial, Surface Science, 441 (1999) L917-L923.

[22] F. Rohr, M. Baumer, H.J. Freund, J.A. Mejias, V. Staemmler, S. Muller, L. Hammer, K. Heinz, Strong relaxations at the Cr_2O_3(0001) surface as determined via low-energy electron diffraction and molecular dynamics simulations, Surface Science, 372 (1997) L291-L297.

[23] R. Rohr, M. Baumer, H.J. Freund, J.A. Mejias, V. Staemmler, S. Muller, L. Hammer, K. Heinz, Erratum to: "Strong relaxations a the Cr_2O_3(0001) surface as determined via low-energy electron diffraction and molecular dynamics simulations" [Surf. Sci. 372 (1997) L291], Surface Science, 389 (1997) 391.

[24] W.A.A. Priyantha, G.D. Waddill, Structure of chromium oxide ultrathin films on Ag(111), Surface Science, 578 (2005) 149-161.

[25] O. Bikondoa, W. Moritz, X. Torrelles, H.J. Kim, G. Thornton, R. Lindsay, Impact of ambient oxygen on the surface structure of alpha-Cr_2O_3(0001), Physical Review B, 81 (2010) 205439.

[26] M. Lubbe, W. Moritz, A LEED analysis of the clean surfaces of alpha-Fe_2O_3(0001) and alpha-Cr_2O_3(0001) bulk single crystals, Journal of Physics: Condensed Matter, 21 (2009) 134010.

Chapter 4

The geometry of α-Cr_2O_3(0001) as a function of H_2O partial pressure

4.1. Introduction

The presence of a passive surface film is key to the exceptional corrosion resistance of stainless steel alloys [1]. Consequently, much effort has targeted characterising and enhancing the functionality of this protective layer, which is composed, at least partially, of chromia [1, 2]. Such work includes fundamental studies of single crystal surfaces of α-Cr_2O_3 to gain atomic scale insight into pertinent properties e.g. interaction with H_2O [3, 4]. To date, however, most of these measurements have been conducted in ultra high vacuum (UHV), limiting their pertinence to mechanistic understanding of corrosion performance in engineering environments. Targeting this omission, the current study is concerned with determining the surface structure of α-Cr_2O_3(0001) in the presence of H_2O vapour through acquisition of surface X-ray diffraction (SXRD) data; H_2O is an essential ingredient for many corrosion phenomena.

The structure of α-Cr_2O_3(0001) as a function of both H_2O partial pressure and temperature has previously been explored by Costa *et al.* through *ab initio* modelling [5]. As a starting point for these calculations, a clean surface terminated by a single layer of 3-fold coordinated Cr's was assumed, as depicted in Figure 4.1 (a); this surface termination is labelled Cr-O_3-Cr- on the basis of its first three atomic layers (the subscript indicates the average number of atoms in each 1×1 unit cell). Near room temperature, it was concluded that two other terminations become energetically favourable in the presence of H_2O. At lower H_2O partial pressures, dissociative adsorption was proposed to be the most likely scenario with each surface Cr becoming decorated with two hydroxyls (OH), i.e. $(OH)_2$-Cr-O_3-; a (OH)-Cr-O_3- termination was found to be energetically unfavourable. Increasing the H_2O partial pressure resulted in the attachment of an intact H_2O molecule to each dihyroxylated Cr to form a new surface termination, i.e. $(H_2O(OH)_2)$-Cr-O_3-.

Figures 4.1 (b) and (c) illustrate the $(OH)_2$-Cr-O_3- and $(H_2O(OH)_2)$-Cr-O_3- adsorbate phases predicted in Reference [5], including the location of the acidic hydrogen resulting from dissociative adsorption of H_2O. This moiety is bound to topmost substrate oxygen atoms, forming a second distinct OH species. Hydrogen bonds formed between surface adsorbates (OH and H_2O) are also indicated in Figures 4.1 (b) and (c). These theoretical structures are consistent with experimental characterisation performed under UHV conditions of thin films of α-Cr_2O_3(0001) exposed to H_2O, in that dissociative adsorption leading to two distinct OH species is evidenced [3]. Moreover, the existence of inter-adsorbate hydrogen bonding is also apparent from vibrational data [3].

Here, the validity of Costa *et al*'s theoretical study [5] is explored experimentally. Analysis of SXRD data acquired at a H_2O partial pressure of ~ 30 mbar indicates that the α-Cr_2O_3(0001) surface is decorated by OH, but not as predicted [5]. This work furthers our previous SXRD study examining the impact of O_2 on the surface structure α-Cr_2O_3(0001) [6].

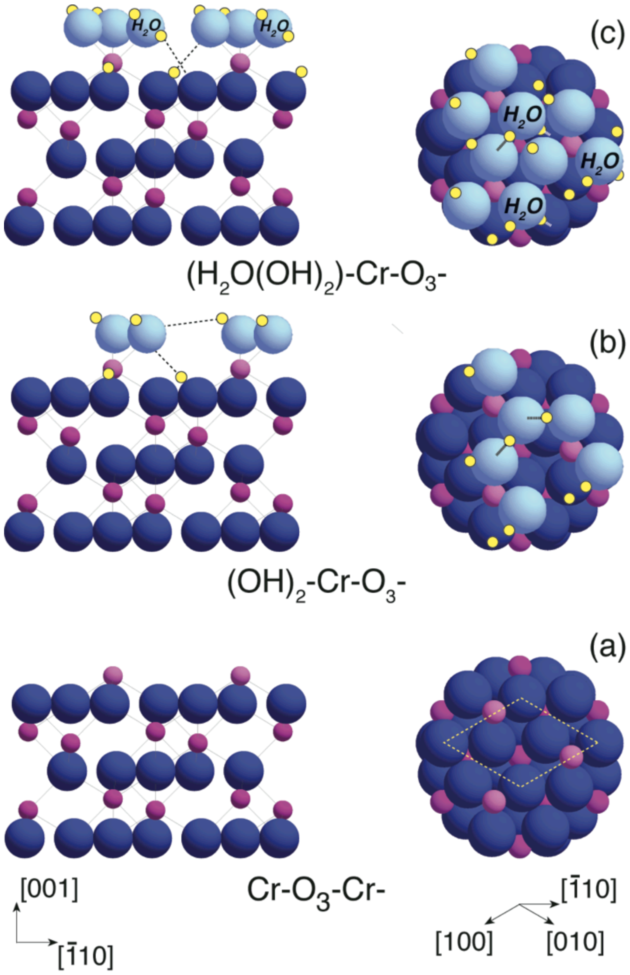

Figure 4.1: (a) Schematic illustration of the clean α-Cr_2O_3(0001)(1x1) surface employed by Costa *et al* in their *ab initio* calculations of the interaction of H_2O with this substrate [5]. To the left (right) is a side (plan) view. The larger (smaller) spheres are oxygen (chromium) atoms. (b) and (c) Similar models of stable OH/H_2O decorated terminations predicted by Costa *et al* at lower (b) and higher (c) H_2O partial pressures. Hydrogen bonding is indicated by means of dashed lines; the smallest spheres are hydrogen atoms.

4.2. Experimental Methods

Experimental work was carried out at the Diamond Light Source (DLS) synchrotron facility, employing the Surface Village's off-line UHV chamber for sample preparation, and beam line I07 for SXRD measurements. *In situ* cleaning of the single crystal α-Cr_2O_3(0001) sample (MaTecK GmbH) involved repeated cycles of Ar^+ bombardment and annealing in UHV to approximately 1200 K. Low energy electron diffraction (LEED), Auger Electron Spectroscopy (AES), and X-ray photoelectron spectroscopy (XPS) facilities were employed for sample characterisation. Figure 4.2 (a) shows a

LEED pattern of the α-Cr_2O_3(0001)(1×1) observed at 350 eV, much like that previously reported, exhibiting sharp diffraction spots and a low background indicating a well ordered and flat surface . Also displayed, Figure 4.2 (b), is an AES spectrum indicating an essentially contaminant free surface (within the detection limits of AES) following sample preparation.

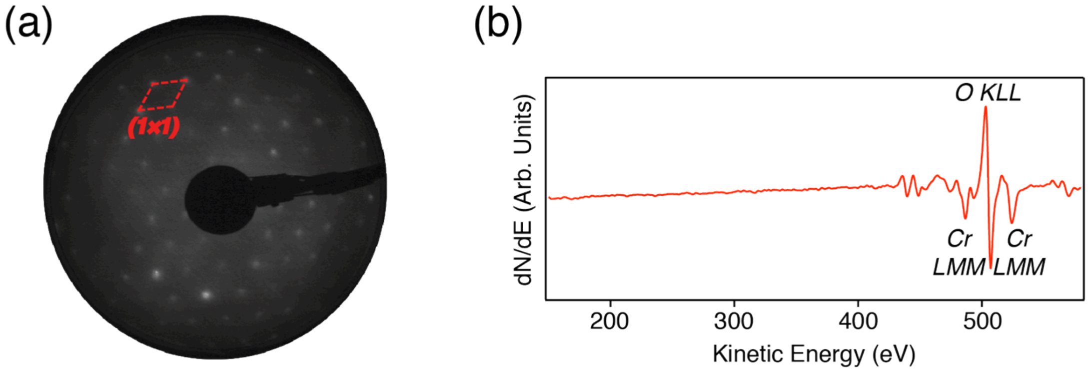

Figure 4.2: (a) LEED pattern taken at 350 eV. Hexagonal surface (1×1) unit cell indicated. (b) AES spectrum showing an essentially contaminant free surface, acquired subsequent to sample preparation.

Subsequent to producing a clean and well-ordered surface, the sample was exposed to ~ 1000 L (Langmuir) of H_2O vapour; prior to dosing the H_2O had been degassed through repeated freeze-thaw-pump cycles. The sample was then transferred under vacuum to I07's diffractometer in Experimental Hutch 1 (EH1), using a custom-built vacuum-suitcase and UHV *baby* chamber combination. The latter (base pressure ~ 1×10^{-9} mbar) incorporates a dome shaped X-ray transparent beryllium window suitable for undertaking SXRD measurements. Once located on the beamline the sample was exposed to a further ~ 1000 L of H_2O vapour; henceforth this surface will be referred to as Cr_2O_3-H_2O_{UHV}. The purpose of dosing H_2O prior to commencing diffraction measurements was to mitigate the risk of any surface contamination during the sample transfer process.

SXRD data were collected at an incidence angle of 1° with the substrate at room temperature, using a photon energy of hν = 17.7 keV (wavelength = 0.7 Å) and a 2D Pilatus photon detector. Initially, a systematic series of X-ray reflections was acquired from Cr_2O_3-H_2O_{UHV}. More specifically, for a given (h, k)-integer, data were measured as a function of l to facilitate generation of so called crystal truncation rods (CTRs); fractional-order rods (FORs) were also surveyed. h, k, and l are the reciprocal lattice vectors, and are defined with reference to the real space (1×1) unit cell of the α-Cr_2O_3(0001) surface, described by lattice vectors ($\boldsymbol{a_1}, \boldsymbol{a_2}, \boldsymbol{a_3}$) which are parallel to the [100], [010], [001] directions, respectively. The magnitudes of these lattice vectors are

$\boldsymbol{a_1} = \boldsymbol{a_2} = a = 4.957$ Å, and $\boldsymbol{a_3} = c = 13.592$ Å, where a and c are the bulk lattice constants [7].

Subsequent to compiling surface diffraction data from Cr_2O_3-H_2O_{UHV} in UHV, the H_2O partial pressure was increased in a stepwise fashion by appropriate back filling of the *baby* chamber with H_2O. We note that above 1×10^{-4} mbar a static volume of H_2O was employed rather than obtaining an equilibrium pressure through balancing the rates of H_2O inflow and pumping, i.e. the *baby* chamber was no longer continuously pumped. For each H_2O partial pressure, the intensity of the (1, 0, 2.9) reflection was monitored to identify changes in the Cr_2O_3(0001) surface structure. Selection of this reflection was based upon its sensitivity to such variation as a function of O_2 partial pressure [6]. On the basis of these measurements (see below), a further systematic series of X-ray reflections was acquired from Cr_2O_3(0001) at a H_2O partial pressure of ~ 30 mbar; henceforth this surface will be referred to as Cr_2O_3-H_2O_{30mbar}.

To facilitate fully quantitative structure determination, the raw diffraction data acquired at UHV and $p(H_2O)$ ~ 30 mbar were integrated and corrected [8] to enable plots of structure factor versus perpendicular momentum transfer for each CTR to be compiled. This procedure resulted in a total of 1054 (1142) non-equivalent reflections from six CTRs for Cr_2O_3-H_2O_{UHV} (Cr_2O_3-H_2O_{30mbar}). Concerning FORs, no evidence for any surface unit cell, other than 1×1, was found.

4.3. Results

Figure 4.3 displays the intensity of the (1, 0, 2.9) reflection as a function of increasing H_2O partial pressure; please note, as described above, the sample had already been dosed with ~ 2000 L of H_2O prior to acquisition of these data. Upon exposure of the sample to ~ 30 mbar of H_2O vapour, there is an increase of ~ 20 % in the signal; this increase is fully reversible, i.e. there is an ~ 20 % decrease in intensity subsequent to reducing the pressure down to ~ 8×10^{-7} mbar. The inset in Figure 4.3 compares rocking scans acquired at UHV (~ 1×10^{-9} mbar) and ~ 30 mbar, demonstrating the significance of the variation in reflection intensity. Furthermore, this comparison shows that there is no appreciable variation in the width of the reflection, indicating that terrace size is not significantly influenced by the presence of H_2O. These data suggest that the presence of ~ 30 mbar of H_2O vapour leads to a modification of the Cr_2O_3(0001) surface structure. This supposition will be confirmed below, through analysis of the CTR datasets acquired from Cr_2O_3-H_2O_{UHV} and Cr_2O_3-H_2O_{30mbar}.

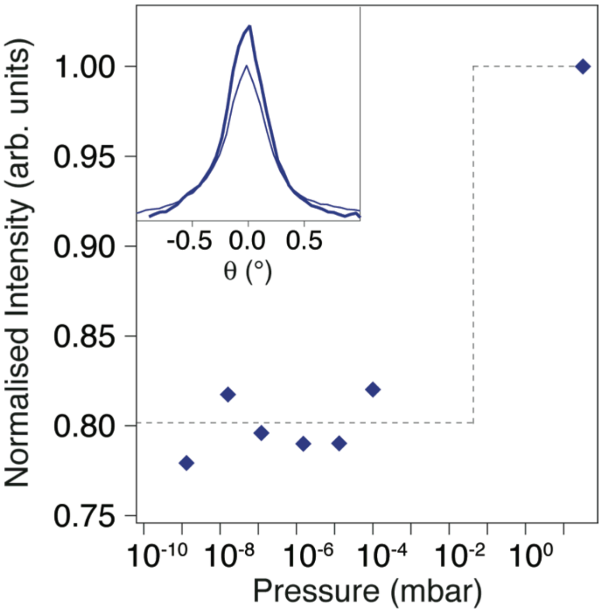

Figure 4.3: Plot of the intensity of the (1, 0, 2.9) reflection as a function of H_2O partial pressure; the Cr_2O_3(0001) sample had been dosed with ~ 2000 L of H_2O prior to acquisition of these data. Dashed line is a guide for the eye. Inset displays (1, 0, 2.9) rocking scans acquired at UHV (thin line) and ~ 30 mbar of H_2O (bold line).

For surface structure determination, we adopted the usual approach of generating simulated SXRD data for a series of potential model structures, and iteratively refining structural (and non-structural) parameters to find the overall best fit between experiment and theory. The ROD software [9] was employed for this purpose. Reduced χ^2 was used to evaluate the goodness of the fit, which is defined as follows:

$$\chi^2 = \frac{1}{N-P}\sum_{i=1}^{N}\left(\frac{\left|F_i^{exp}(hkl)\right|^2 - \left|F_i^{th}(hkl)\right|^2}{\sigma_i^{exp}(hkl)}\right)^2 \qquad (4.1)$$

N is the number of measured structure factors, P the number of parameters optimized during fitting. $F_i^{exp}(hkl)$ and $F_i^{th}(hkl)$ are the experimental and theoretically calculated structure factors, respectively. $\sigma_i^{exp}(hkl)$ is the uncertainty associated with the experimental data. χ^2 behaves such that a value of 1 indicates that experiment and theory are essentially coincident, with agreement decreasing with increasing χ^2. Values of χ^2 significantly less than 1 suggest that the magnitudes of experimental uncertainties have been overestimated. The quoted precision of each fitted parameter is determined by varying the parameter about its optimal value until χ^2 has increased by $\frac{1}{N-P}$ from its minimum value [10].

Initially, attention focused upon the diffraction data acquired from Cr_2O_3-H_2O_{UHV}. To begin the search for a structural solution, the clean surface structure (Cr_2O_3-clean$_{UHV}$) concluded in recent quantitative LEED (LEED-IV) [11] and SXRD [6] studies was considered as a starting point. This surface exhibits a topmost partially occupied double layer of Cr atoms ($Cr_{0.31}$-$Cr_{0.61}$-$O_{2.4}$- from LEED-IV [11], and $Cr_{0.22}$-$Cr_{0.31}$-O_3- from SXRD [6]). Given that the current measurements were undertaken subsequent to an exposure to ~ 2000 L of H_2O, terminations with surface Cr atoms bonded to one or more OH/H_2O species were tested. It should be noted that H atoms were not explicitly included during generation of simulated of SXRD data, due to their negligible X-ray scattering, i.e. only an oxygen atom was added for each OH/H_2O. Refinement of these OH/H_2O decorated structures, including atomic coordinates, site occupation, and a surface roughness parameter (β), resulted in χ^2's of 1.7, 2.1, and 1.8 for Cr atoms bound to one, two, or three OH/H_2O species, respectively. For completeness, a similar structural refinement was undertaken without any adsorbed OH/H_2O. Optimization of this structure resulted in a χ^2 of 1.2, indicating that the SXRD data provide no substantive evidence for adsorbed OH/H_2O under the prevailing experimental conditions. Given that previous studies of α-Cr_2O_3(0001) in UHV have revealed the presence of adsorbed OH/H_2O [3, 4], the most likely explanation for this discrepancy is that the impinging X-ray beam induces OH/H_2O desorption.

Figure 4.4 displays a comparison of the experimental CTRs acquired from Cr_2O_3-H_2O_{UHV} with the best-fit theoretical simulations. To achieve this fit 41 parameters were optimized, i.e. 35 atomic coordinates, a scale factor, a surface roughness parameter, and fractional occupancy factors for Cr(1), Cr(2), O(1), and Cr(3) (these atoms are identified in Figure 4.5); Debye-Waller factors for all atoms were maintained at bulk values, i.e. 0.5 Å^2. As may be expected for a χ^2 value of 1.2, there is a good level of agreement between theory and experiment. In a number of regions away from Bragg peaks, however, the uncertainty in the experimental structure factor is relatively large and can encompass zero. Given this situation, which may lead one to question the reliability of the optimum structure, a further structure refinement was undertaken excluding all data points where the error in the structure factor includes zero. Employing this more limited dataset did not result in any significant changes in the structural solution, and so was not considered further.

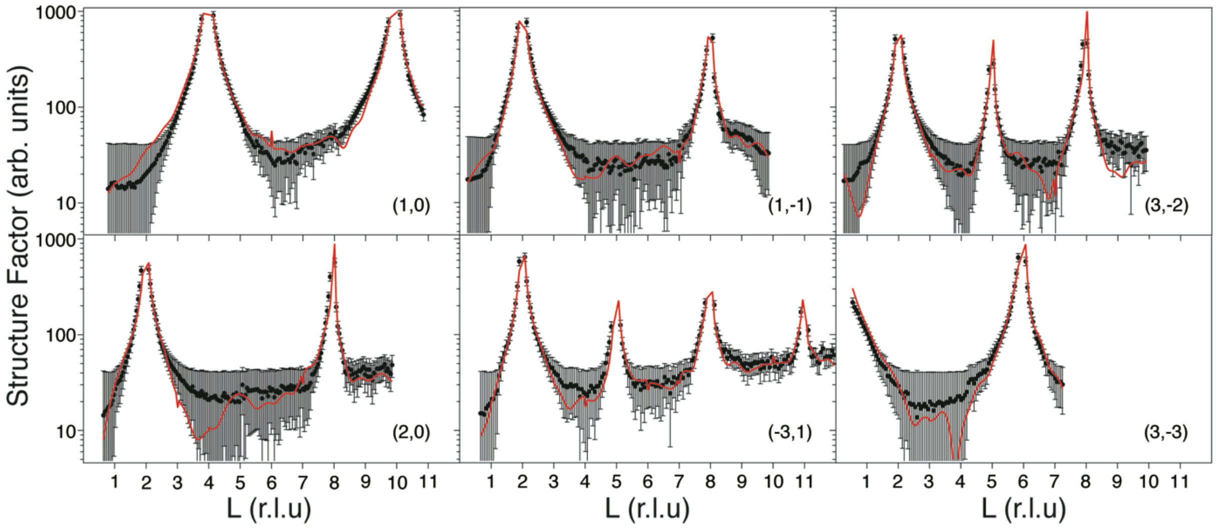

Figure 4.4: Comparison of experimental CTR data (solid markers with error bars), acquired from Cr_2O_3(0001) in UHV subsequent to exposure to ~ 2000 L of H_2O (Cr_2O_3-H_2O_{UHV}), and theoretical best-fit simulations (solid red lines).

The surface geometry emerging from analysis of the data acquired from Cr_2O_3-H_2O_{UHV} is illustrated in Figure 4.5. Corresponding atomic coordinates are listed in Table 4.1. A topmost partially occupied Cr double layer is maintained in the optimised structure, although the fractional occupancies of both Cr sites are significantly less than those determined previously for Cr_2O_3-clean$_{UHV}$ [6, 11]; layer occupancies determined from analysis of SXRD for Cr_2O_3-H_2O_{UHV} (current study) and Cr_2O_3-clean$_{UHV}$ [6] are indicated in Figure 4.5. Atomic layer spacings perpendicular to the α-Cr_2O_3(0001) surface derived from both the current results and the earlier measurements [6, 11] are listed in Table 4.2. Similar to the fractional occupancies, there are non-negligible variations in these values. As mentioned in Reference [6], a plausible explanation for these discrepancies in surface structure is that they arise from small variations in sample preparation, e.g. anneal temperature. Furthermore, it should be remembered that the latest SXRD data were recorded subsequent to an exposure of 2000 L of H_2O, which may have induced surface modification, even though no evidence of surface bound OH/H_2O was explicitly found during analysis of the diffraction data. For example, a proportion of topmost oxygen atoms may in reality be OH's due to reaction with the acidic hydrogen resulting from dissociative adsorption of H_2O. The optimum value of the surface roughness parameter (β = 0.42), along with lower fractional occupancies of surface layers, may also reflect surface modification induced by H_2O exposure; β = 0.2 was obtained during fitting of the SXRD data acquired from Cr_2O_3-clean$_{UHV}$ in Reference [6]. Greater surface roughness following H_2O exposure is apparently consistent with STM images acquired from a thin film of α-Cr_2O_3(0001) [4], which suggest that H_2O induces geometric disordering within terraces.

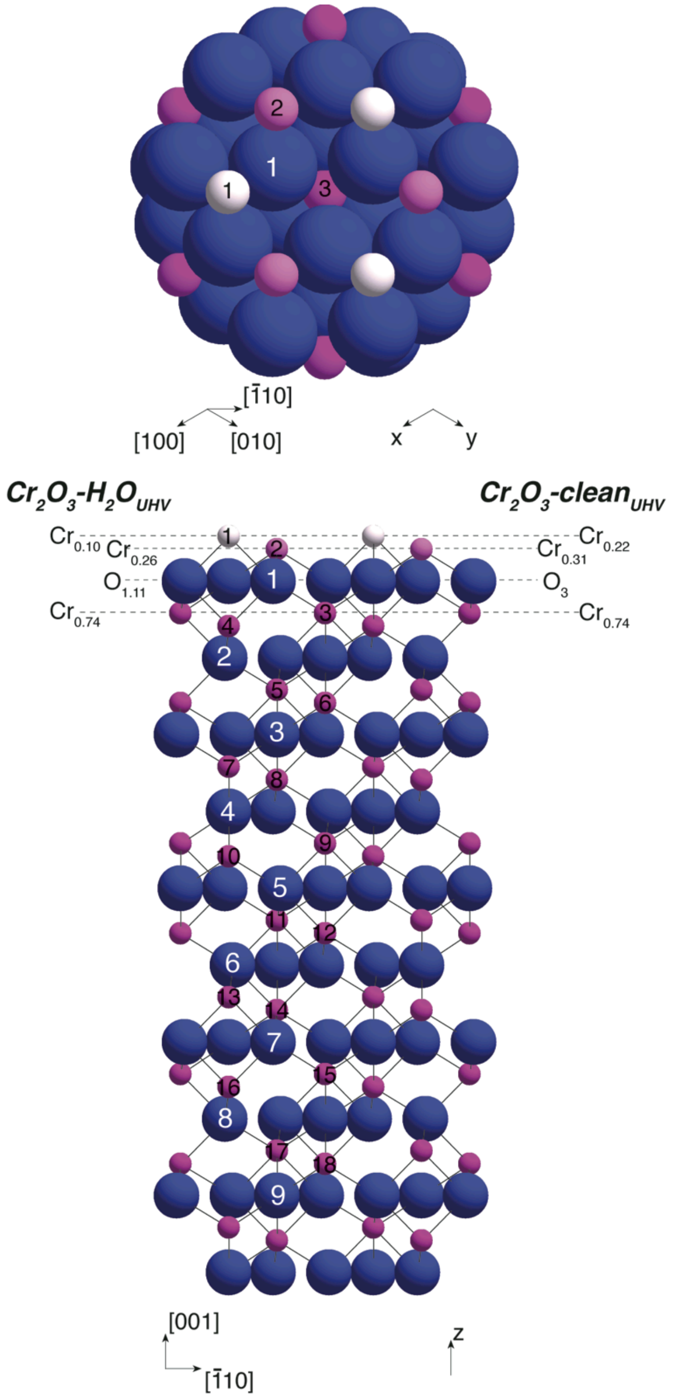

Figure 4.5: Schematic models of the a-Cr_2O_3(0001) surface structure determined from SXRD data acquired in UHV, following exposure to ~ 2000 L of H_2O (Cr_2O_3-H_2O_{UHV}). At the bottom (top) is a side (plan) view. Larger (smaller) spheres are oxygen (chromium) atoms. Numerical labeling of atoms is employed for identification purposes. Layer occupancies determined for Cr_2O_3-H_2O_{UHV} (current study) and Cr_2O_3-clean$_{UHV}$ [6] are indicated.

Table 4.1: Optimized (*x*, *y*, *z*) coordinates of atoms comprising the Cr_2O_3-H_2O_{UHV} surface resulting from analysis of the SXRD data presented in Figure 4.4. Fractional occupancy is indicated by a non-integer subscript in the 'Atom' column; the overall occupancy of oxygen atoms in the layer containing O(1) is 1.11 ± 0.12, as there are three symmetry equivalent oxygen atoms per (1x1) unit cell. Atomic coordinates

for the bulk-terminated Cr-Cr-O_3-structure are also listed. Figure 4.5 provides a key to the identity of the atoms, and the axes x, y, and z. An asterisk (*) indicates that the parameter has been held constant during optimization. x and y coordinates not optimized due to symmetry constraints are italicized.

	(x, y, z) coordinates (Å)	
Atom	Bulk-terminated	Optimised
$Cr_{0.10\pm 0.02}$(1)	3.31, 1.65, 22.65	_3.31*_, _1.65*_, 23.08 ± 0.09
$Cr_{0.26\pm 0.02}$(2)	0.00, 0.00, 22.27	_0.00*_, _0.00*_, 22.81 ± 0.03
$O_{0.37\pm 0.04}$(1)	1.79, 1.65, 21.33	1.90 ± 0.04, 1.57 ± 0.05, 21.54 ± 0.05
$Cr_{0.74\pm 0.01}$(3)	1.65, 3.31, 20.39	_1.65*_, _3.31*_, 20.55 ± 0.01
Cr(4)	3.31, 1.65, 20.00	_3.31*_, _1.65*_, 19.99 ± 0.01
O(2)	1.65, -0.14, 19.06	1.68 ± 0.02, -0.14 ± 0.04, 18.89 ± 0.03
Cr(5)	0.00, 0.00, 18.12	_0.00*_, _0.00*_, 18.22 ± 0.01
Cr(6)	1.65, 3.31, 17.74	_1.65*_, _3.31*_, 17.86 ± 0.01
O(3)	1.52, 1.52, 16.80	1.53 ± 0.03, 1.56 ± 0.02, 16.90 ± 0.03
Cr(7)	3.31, 1.65, 15.86	_3.31*_, _1.65*_, 15.96 ± 0.01
Cr(8)	0.00, 0.00, 15.47	_0.00*_, _0.00*_, 15.56 ± 0.01
O(4)	1.79, 0.14, 14.53	1.80±0.03, 0.05±0.02, 14.60 ± 0.03
Cr(9)	1.65, 3.31, 13.59	_1.65*_, _3.31*_, 13.64 ± 0.01
Cr(10)	3.31, 1.65, 13.21	_3.31*_, _1.65*_, 13.26 ± 0.01
O(5)	1.65, 1.79, 12.27	1.62 ± 0.02, 1.74 ± 0.03, 12.17 ± 0.04
Cr(11)	0.00, 0.00, 11.33	_0.00*_, _0.00*_, 11.38 ± 0.01
Cr(12)	1.65, 3.31, 10.94	_1.65*_, _3.31*_, 10.97 ± 0.01
O(6)	1.52, 0.00, 10.00	_1.52 *_, _0.00*_, 10.08 ± 0.03
Cr(13)	3.31, 1.65, 9.06	_3.31*_, _1.65*_, 9.10 ± 0.01
Cr(14)	0.00, 0.00, 8.68	_0.00*_, _0.00*_, 8.81 ± 0.01
O(7)	1.79, 1.65, 7.74	1.79*, 1.65*, 7.74 ± 0.02
Cr(15)	1.65, 3.31, 6.80	_1.65*_, _3.31*_, 6.83 ± 0.01
Cr(16)	3.31, 1.65, 6.41	_13.31*_, _1.65*_, 6.42 ± 0.01
O(8)	1.65, - 0.14, 5.47	1.65*, -0.14*, 5.47 ± 0.02
Cr(17)	0.00, 0.00, 4.53	_0.00*_, _0.00*_, 4.55 ± 0.01
Cr(18)	1.65, 3.31, 4.15	_1.65*_, _3.31*_, 4.16 ± 0.01
O(9)	1.52, 1.52, 3.20	1.52*, 1.52*, 3.24 ± 0.03

Table 4.2: Comparison of atomic layer spacings (d_z) perpendicular to the α-Cr_2O_3(0001) surface derived from previous UHV LEED-IV [11] and SXRD [6] work, and the current UHV SXRD measurements acquired following exposure to ~ 2000 L of H_2O. Bulk terminated interlayer distances are also listed. Figure 4.5 indicates the identity of the atomic layers.

Atomic Layers	d_z (Å) Bulk-terminated	LEED-IV [11]	SXRD [6]	SXRD This study
Cr(1)/Cr(2)	0.38	0.27	0.22 ± 0.04	0.27 ± 0.05
Cr(2)/O(1)	0.94	1.04	1.30 ± 0.03	1.27 ± 0.05
O(1)/Cr(3)	0.94	0.96	0.68 ± 0.03	0.99 ± 0.03
Cr(3)/Cr(4)	0.38	0.38	0.33 ± 0.01	0.56 ± 0.02
Cr(4)/O(2)	0.94	0.93	0.64 ± 0.01	1.10 ± 0.02
O(2)/Cr(5)	0.94	Not optimized	1.36 ± 0.01	0.67 ± 0.02

Turning to Cr_2O_3-H_2O_{30mbar}, structure determination commenced with refinement of the coordinates of the optimized Cr_2O_3-H_2O_{UHV} structure. A best-fit χ^2 of 3.2 was obtained, suggesting that the presence of ~ 30 mbar H_2O results in surface modification beyond mere relaxation. Consequently, terminations of the optimum Cr_2O_3-H_2O_{UHV} structure, where surface Cr atoms are bound to one or more OH/H_2O species, were tested. Refinement of these OH/H_2O decorated structures, resulted in χ^2's of 1.1, 2.1, and 2.3 for Cr atoms bound to one, two, or three OH/H_2O species, respectively, i.e. a structure where each surface Cr is bound to a single OH/H_2O species is favored. More specifically, OH/H_2O is concluded to be atop Cr, at a distance of 2.09 Å (error ranging from ± 0.01 to ± 0.05); off atop adsorption was also tested, but found to increase χ^2. A comparison of the experimental CTRs with the best-fit theoretical simulations is shown in Figure 4.5.

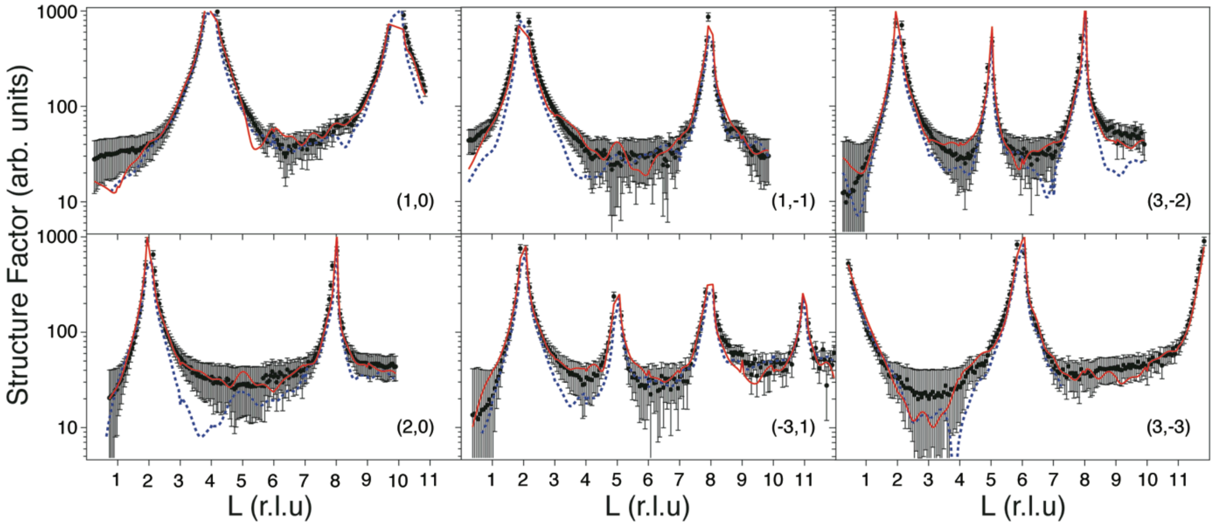

Figure 4.6: Comparison of experimental CTR data (solid markers with error bars), acquired from α-Cr_2O_3(0001) at $p(H_2O)$ ~ 30 mbar (Cr_2O_3-H_2O_{30mbar}), and theoretical best-fit simulations (solid red lines). Also included are theoretically simulated data (broken blue line) for optimum Cr_2O_3-H_2O_{UHV} geometry.

Figure 4.7 depicts the surface structural model employed to obtain the best-fit displayed in Figure 4.6, in which the oxygen atoms of adsorbed OH/H_2O species are labelled with 1′, 2′, 3′, and 4′. As illustrated, the best fit was obtained with OH/H_2O (O(1′) – O(4′)) located atop Cr(1) and Cr(2), as well as above Cr(3) and Cr(4) atoms available for bonding due to fractional occupation of the topmost oxygen layer (O(1)); it should be borne in mind that the presence of O(3′) and O(4′) does not result in unphysical inter-atomic distances, as the fractional occupancy of these atoms is governed by fractional occupancy of O(1). Optimum atomic coordinates are listed in Table 4.3. During fitting 35 atomic coordinates were varied. In addition, similar to above, a scale factor, a surface roughness parameter, and fractional occupancy factors for Cr(1), Cr(2), O(1), and Cr(3) were also optimized; Debye-Waller factors for all atoms were again maintained at bulk values, i.e. 0.5 Å^2. The optimum surface roughness parameter, $\beta = 0.39$, is very similar to that obtained for Cr_2O_3-H_2O_{UHV}, indicating that immersion in $p(H_2O) \sim 30$ mbar does not induce further surface roughening. Furthermore, it should be noted that O(1′) and O(2′) were constrained to have the same fractional occupancies as Cr(1) and Cr(2), respectively. Similarly, the fractional occupations of O(3′) and O(4′) were fixed to be equal to the fraction of available Cr(3) and Cr(4) atoms, respectively. Finally, all Cr-OH/H_2O bond lengths (i.e. Cr(1)-O(1′), Cr(2)-O(2′), Cr(3)-O(3′), and Cr(4)-O(4′)) were constrained to have the same value during optimisation.

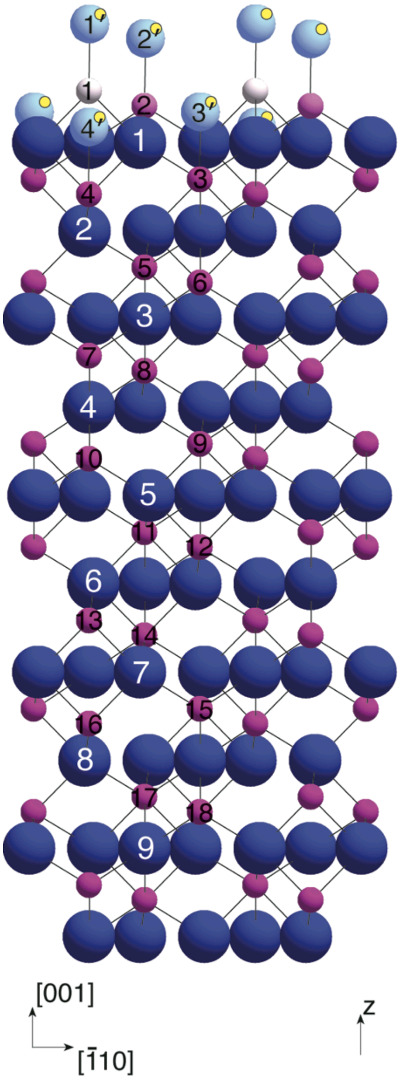

Figure 4.7: Ball and stick model (side view) of the surface termination of a-Cr_2O_3(0001) employed for fitting the SXRD data acquired at $p(H_2O)$ ~ 30 mbar (Cr_2O_3-H_2O_{30mbar}). Larger (smaller) spheres are oxygen (chromium) atoms; the smallest spheres are hydrogen atoms, which are employed to indicate location of adsorbed OH/H_2O. The oxygen atoms of adsorbed OH/H_2O species are labelled with 1′, 2′, 3′, and 4′. Numerical labeling of atoms is employed for identification purposes.

Table 4.3: Optimized (x, y, z) coordinates of atoms comprising the Cr_2O_3-H_2O_{30mbar} surface resulting from analysis of the SXRD data presented in Figure 4.6. Fractional occupancy is indicated by a non-integer subscript in the 'Atom' column; the overall occupancy of oxygen atoms in the layer containing O(1) is 1.2 ± 0.09, as there are three symmetry equivalent oxygen atoms per (1x1) unit cell. Atomic coordinates for the bulk-terminated Cr-Cr-O_3-structure are also listed. Figure 4.7 provides a key to the identity of the atoms. An asterisk (*) indicates that the parameter has been held constant during optimization. x and y coordinates not optimized due to symmetry constraints are italicized.

	(x, y, z) co-ordinates (Å)	
Atom	Bulk-terminated	Optimised
$O_{0.08\pm0.01}$(1′)	N/A	_3.31_*, _1.65_*, 24.88 ± 0.05
$O_{0.28\pm0.01}$(2′)	N/A	_0.00_*, _0.00_*, 24.14± 0.02
$Cr_{0.08\pm0.01}$(1)	3.31, 1.65, 22.65	_3.31_*, _1.65_*, 22.79 ± 0.05
$Cr_{0.28\pm0.01}$(2)	0.00, 0.00, 22.27	_0.00_*, _0.00_*, 22.05 ± 0.02
$O_{0.30\pm0.01}$(3′)	N/A	_1.65_*, _3.31_*, 22.60 ± 0.01
$O_{0.60\pm0.01}$(4′)	N/A	_3.31_*, _1.65_*, 22.36 ± 0.01
$O_{0.40\pm0.03}$(1)	1.79, 1.65, 21.33	1.76 ± 0.02, 1.74 ± 0.03, 21.25 ± 0.05
$Cr_{0.70\pm0.01}$(3)	1.65, 3.31, 20.39	_1.65_*, _3.31_*, 20.52 ± 0.01
Cr(4)	3.31, 1.65, 20.00	_3.31_*, _1.65_*, 20.27 ± 0.01
O(2)	1.65,- 0.14, 19.06	1.66 ± 0.01, -0.14± 0.02, 19.06 ± 0.02
Cr(5)	0.00, 0.00, 18.12	_0.00_*, _0.00_*, 18.22 ± 0.01
Cr(6)	1.65, 3.31, 17.74	_1.65_*, _3.31_*, 17.83 ± 0.01
O(3)	1.52, 1.52, 16.80	1.54 ± 0.02, 1.54 ± 0.01, 16.96 ± 0.02
Cr(7)	3.31, 1.65, 15.86	_3.31_*, _1.65_*, 15.99 ± 0.01
Cr(8)	0.00, 0.00, 15.47	_0.00_*, _0.00_*, 15.54 ± 0.01
O(4)	1.79, 0.14, 14.53	1.77±0.02, 0.01±0.01, 14.63 ± 0.02
Cr(9)	1.65, 3.31, 13.59	_1.65_*, _3.31_*, 13.74 ± 0.01
Cr(10)	3.31, 1.65, 13.21	_3.31_*, _1.65_*, 13.28 ± 0.01
O(5)	1.65,1.79,12.27	1.69 ± 0.01, 1.76 ± 0.02, 12.30 ± 0.02
Cr(11)	0.00,0.00,11.33	_0.00_*, _0.00_*, 11.39 ± 0.01
Cr(12)	1.65,3.31,10.94	_1.65_*, _3.31_*, 11.02 ± 0.01
O(6)	1.52,0.00,10.00	1.52*, 0.00*, 10.06 ± 0.01
Cr(13)	3.31, 1.65, 9.06	_3.31_*, _1.65_*, 9.12 ± 0.01
Cr(14)	0.00, 0.00, 8.68	_0.00_*, _0.00_*, 8.73 ± 0.01
O(7)	1.79, 1.65, 7.74	1.79*, 1.65*, 7.78 ± 0.01
Cr(15)	1.65, 3.31, 6.80	_1.65_*, _3.31_*, 6.85 ± 0.01
Cr(16)	3.31, 1.65, 6.41	_3.31_*, _1.65_*, 6.45 ± 0.01
O(8)	1.65, -0.14, 5.47	1.65*, -0.14*, 5.50 ± 0.01
Cr(17)	0.00, 0.00, 4.53	_0.00_*, _0.00_*, 4.57 ± 0.01
Cr(18)	1.65, 3.31, 4.15	_1.65_*, _3.31_*, 4.16 ± 0.01
O(9)	1.52, 1.52, 3.20	1.52*, 1.52*, 3.22 ± 0.03

4.4. Discussion

Figure 4.8 summarizes the variation in surface termination of α-Cr_2O_3(0001) determined through analysis of the SXRD data acquired from Cr_2O_3-H_2O_{UHV} and Cr_2O_3-H_2O_{30mbar}, i.e. in the presence of ~ 30 mbar of H_2O, each under-coordinated surface Cr atom becomes bound to a single atop OH/H_2O species. Regarding the significance of this result, it should be remembered that data from previous studies [3, 4] suggest that the Cr_2O_3-H_2O_{UHV} surface should exhibit hydroxyls. Hence, it is almost certain that the observed change is a result of the impinging synchrotron X-ray radiation inducing adsorbate desorption; such a process will still occur at $p(H_2O)$ ~ 30 mbar, but the OH/H_2O overlayer is dynamically maintained.

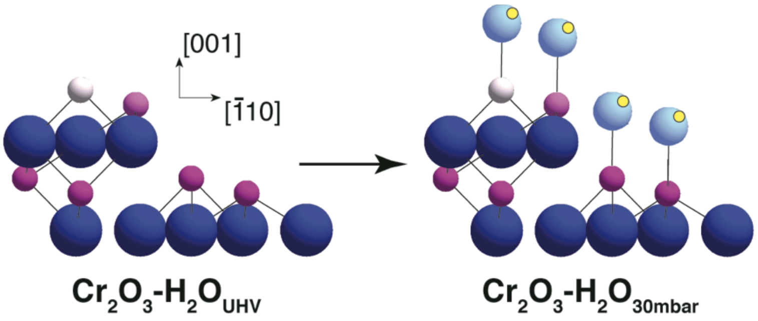

Figure 4.8: Cartoon of the variation in surface termination of a-Cr_2O_3(0001) with water partial pressure, as determined through analysis of the SXRD data acquired from Cr_2O_3-H_2O_{UHV} and Cr_2O_3-H_2O_{30mbar}.

Despite the apparently adverse impact of the X-ray beam, it can still be concluded that the structure determined at $p(H_2O)$ ~ 30 mbar is seemingly inconsistent with the predictions emerging from the calculations of Costa *et al.* [5]. They conclude that a (OH)-Cr-O_3- termination is energetically unfavourable, directly contradicting our experimental structure determination. Of course, it may be argued that this discrepancy is again due to the influence of the X-ray beam. However, in our opinion, that the X-ray beam would selectively desorb OH/H_2O species from each surface Cr leaving one remaining appears doubtful. A more plausible reason for the divergence between the *ab initio* predictions and experiment is that the initial clean substrate termination used for the calculations is significantly different to that determined from diffraction [5]. It could be that the more disordered surface found in experiment hinders the formation of an extended network of OH/H_2O hydrogen bonding, which emerges from the first principles modelling, resulting in Cr binding to multiple OH/H_2O species becoming energetically unfavourable. Another possible reason for the difference is that there is a significant energy barrier to the attachment of additional

OH/H_2O to each Cr, and so cannot be realised with the substrate at room temperature. Further *ab intio* modelling on Cr_2O_3(0001) substrates more closely mimicking reality are required to test these hypotheses.

Regarding the precise nature of the adsorbed species at 30 mbar of H_2O, only the Cr-(OH/H_2O) interatomic distance (i.e. Cr(1)-O(1′), Cr(2)-O(2′), Cr(3)-O(3′), and Cr(4)-O(4′)) provides any direct insight. As indicated above, a value of 2.09 Å, with an error bar ranging from ± 0.01 Å for Cr(3)-O(3′) and Cr(4)-O(4′) to ± 0.07 Å for Cr(1)-O(1′), has been obtained for this parameter. Costa *et al.* predict that the Cr-O bond length for a surface bound OH moiety should be 1.97 Å, increasing to 2.1 Å for adsorbed H_2O [5]. On this basis, one might propose that at 30 mbar of H_2O, Cr_2O_3(0001) is decorated with adsorbed molecular H_2O rather than OH. However, this deduction must be regarded with particular caution due to the approach employed for fitting the diffraction data, i.e. to limit the number of parameters optimized, the possibility for each substrate atom to adopt more than one location was not incorporated, even where there were variations in local environment. For example, regarding the Cr_2O_3-$H_2O_{30\text{mbar}}$ data, this approach resulted in employing only two atoms (Cr(3) and Cr(4)) to describe the first subsurface double layer of Cr atoms, even though some are bound to O(1) and others to O(3′) or O(4′) atoms. Given that this change in local coordination is likely to lead to somewhat different atomic coordinates, the Cr-(OH/H_2O) inter atomic distance (2.09 Å) is less well defined than indicated above. Consequently, we conclude that it is not possible to uniquely identify the adsorbate (OH or H_2O) present on Cr_2O_3-$H_2O_{30\text{mbar}}$ from the current SXRD dataset. However, the weight of other evidence [3,4,5] suggests that dissociative adsorption is more likely, i.e. OH.

Comparing the current results to those obtained for the interaction of H_2O with other (0001) surfaces of corundum type metal oxides, of particular pertinence are near ambient pressure photoemission data from a-Fe_2O_3(0001) [13]. In that study, it was concluded that as the partial pressure of H_2O increases, the surface becomes increasingly decorated with surface OH, attaining a maximum coverage of ~ 1 monolayer at ~ 10^{-4} mbar. Adsorbed H_2O is also observed, which is proposed to be located above the OHs, i.e. a three layer Fe_2O_3(0001)/OH/H_2O interface is formed. One might also expect similar layering on a-Cr_2O_3(0001) at 30 mbar of H_2O, but only a single OH/H_2O layer emerges from analysis of the SXRD data. However, it should be remembered that SXRD is sensitive to adsorbed layers displaying order both parallel and perpendicular to the surface plane of the substrate. Hence, the analysis presented here should not be interpreted as indicating that only a single layer of OH/H_2O is present on Cr_2O_3(0001) at 30 mbar H_2O, but that only this layer is sufficiently ordered to be apparent in SXRD.

Another result worthy of mention is the local adsorption geometry of OH obtained from photoelectron diffraction (PhD) measurements in UHV performed following exposure of V_2O_3(0001) to H_2O [14]. In contrast to the current study, no evidence for OH atop surface V atoms was found. Instead, only the surface oxygen atoms (equivalent to O(1) in Figs. 4 and 6) are hydroxylated through attachment of a H, presumably derived from H_2O dissociation; the location of the dissociated OH fragment is not identified. This difference may be due to the initial V_2O_3(0001) surface being terminated by vanadyl groups (V=O), rather than under-coordinated V atoms [14].

Of further interest is a brief consideration of the previous SXRD study probing the surface structure a-Cr_2O_3(0001) as a function of oxygen partial pressure [6]. It is pleasing to note that away from UHV (p(H_2O) ~ 30 mbar (current study), and p(O_2) = 1 × 10^{-2} mbar [6]) the optimum surface structures are not identical, i.e. data have not simply been acquired from similarly contaminated surfaces due to extrinsic components of the ambient environment. For both H_2O and O_2, adsorption occurs atop under coordinated surface Cr atoms, but the Cr-O bond distance is significantly shorter following immersion in O_2 (1.57 ± 0.03 Å) than in H_2O. This shorter Cr-O distance is consistent with the formation of surface chromyl (Cr=O) groups in the presence of oxygen [6]. Furthermore, unlike H_2O/OH decorated a-Cr_2O_3(0001), the chromyl terminated surface remains intact following reduction of the O_2 partial pressure.

4.5. Conclusions

To summarize, SXRD data have been acquired from α-Cr_2O_3(0001) as a function of H2O partial pressure. In UHV, subsequent to an exposure to ~ 2000 L of H_2O, the surface is terminated by a partially occupied double layer of chromium atoms; the lack of adsorbed OH/H_2O is concluded to be most likely a result of x-ray induced desorption. This surface geometry is largely consistent with those determined in recent LEED-IV [11] and SXRD [6] studies of clean α-Cr_2O_3(0001) in UHV, although there are differences in the values of atomic coordinates and fractional layer occupancies. At ~ 30 mbar of H_2O, a single OH/H_2O species is bound atop each surface Cr. This result is not consistent with the ab initio calculations of Costa et al. [5], which predict that surface termination evolves as follows as a function of H2O partial pressure at around room temperature: Cr-O_3-Cr- $(OH)_2$-Cr-O_3- ($H_2O(OH)_2$)-Cr-O_3-. One plausible explanation for this discrepancy between theory and experiment is that the initial clean substrate termination used for the calculations is not that determined experimentally.

4.6. References

[1] P. Marcus, V. Maurice, Passivity of Metals and Alloys, in: Materials Science and Technology: A Comprehensive Treatment: Corrosion and Environmental Degradation, Volumes I+II, Wiley-VCH Verlag GmbH, 2008, pp. 131-169.

[2] A. Iversen, B. Leffler, 3.04 - Aqueous Corrosion of Stainless Steels, in: B. Cottis, M. Graham, R. Lindsay, S. Lyon, T. Richardson, D. Scantlebury, H. Stott (Eds.) Shreir's Corrosion, Elsevier, Oxford, 2010, pp. 1802-1878.

[3] M.A. Henderson, S.A. Chambers, HREELS, TPD and XPS study of the interaction of water with the alpha-Cr2O3(001) surface, Surface Science, 449 (2000) 135-150.

[4] V. Maurice, S. Cadot, P. Marcus, Hydroxylation of ultra-thin films of alpha-Cr_2O_3(0001) formed on Cr(100), Surface Science, 471 (2001) 43-58.

[5] D. Costa, K. Sharkas, M.M. Islam, P. Marcus, Ab initio study of the chemical states of water on Cr_2O_3(0001): From the isolated molecule to saturation coverage, Surface Science, 603 (2009) 2484-2493.

[6] O. Bikondoa, W. Moritz, X. Torrelles, H.J. Kim, G. Thornton, R. Lindsay, Impact of ambient oxygen on the surface structure of alpha-Cr_2O_3(0001), Physical Review B, 81 (2010) 205439.

[7] T. Gloege, H.L. Meyerheim, W. Moritz, D. Wolf, X-ray structure analysis of the Cr_2O_3(0001)-(1x1) surface: evidence for Cr interstitial, Surface Science, 441 (1999) L917-L923.

[8] E. Vlieg, A (2+3)-Type Surface Diffractometer: Mergence of the z-Axis and (2+2)-Type Geometries, Journal of Applied Crystallography, 31 (1998) 198-203.

[9] E. Vlieg, ROD: a program for surface X-ray crystallography, Journal of Applied Crystallography, 33 (2000) 401-405.

[10] R. Feidenhans'l, Surface structure determination by X-ray diffraction, Surface Science Reports, 10 (1989) 105-188.

[11] M. Lubbe, W. Moritz, A LEED analysis of the clean surfaces of alpha-Fe_2O_3(0001) and alpha-Cr_2O_3(0001) bulk single crystals, Journal of Physics: Condensed Matter, 21 (2009) 134010.

[12] N. Papassiopi, F. Pinakidou, M. Katsikini, G.S.E. Antipas, C. Christou, A. Xenidis, E.C. Paloura, A XAFS study of plain and composite iron(III) and chromium(III) hydroxides, Chemosphere, 111 (2014) 169-176.

[13] S. Yamamoto, T. Kendelewicz, J.T. Newberg, G. Ketteler, D.E. Starr, E.R. Mysak, K.J. Andersson, H. Ogasawara, H. Bluhm, M. Salmeron, G.E. Brown, A. Nilsson, Water Adsorption on alpha-Fe_2O_3(0001) at near Ambient Conditions, The Journal of Physical Chemistry C, 114 (2010) 2256-2266.

[14] E. A. Kröger, D. I. Sayago, F. Allegretti, M. J. Knight, M. Polcik, W. Interberger, T. J. Lerotholi, K. A. Hogan, C. L. A. Lamont, M. Cavalleri, K. Hermann, D. P. Woodruff, The local structure of OH species on the V_2O_3(0001) surface: a scanned-energy mode photoelectron diffraction study, Surface Science, 602 (2008) 1267.

.

Chapter 5

Elucidating the geometry of the rutile-TiO_2(011)/ H_2O interface

5.1. Introduction

Titanium dioxide, in particular the rutile (110) surface termination, has emerged as the prototypical metal oxide surface for fundamental studies [1]. However, the much less studied (011) termination has been shown to display higher photocatalytic activity [2, 3], dependent to some extent on the geometry of the surface. Previously a number of structural models of the UHV prepared (011) surface termination displaying a (2×1) reconstructed surface were suggested on the basis of DFT calculations and scanning probe measurements [3-5], including a titanyl group (Ti=O) terminated surface [4]. It was hypothesized that the presence of these Ti=O species could be the source of the enhanced photocatalytic activity of the TiO_2(011) surface. Contradictory to these findings, recent quantitative structural studies using surface X-ray diffraction (SXRD) [6, 7] and low energy electron diffraction (LEED-IV) [8] have revealed a quite different morphology, a geometry presenting a saw-tooth-like morphology with five-fold coordinated titanium atoms and two-fold coordinated surface oxygen atoms arranged in rows along the $[01\bar{1}]$ direction is deduced. DFT calculations and STM images [9] corroborate this model.

Given the potential importance of the TiO_2(011) surface as a photocatalyst for water splitting, elucidating of the interface geometry in an aqueous environment is essential to furthering understanding of the photoactivity of this surface. In contrast to the lack of experimental data on this topic, the geometry of $TiO_2(011)/H_2O$ interface has been studied in some detail by means of first principles calculations by Aschauer *et al* [10]. These calculations suggest there is a significant rearrangement of surface atoms upon exposure to H_2O, whereby the (2×1) reconstruction reverts to a (1×1) unit cell. They also concluded that water dissociates at the interface to form a monolayer of hydroxyls at saturation coverage, which are adsorbed in alternating orientations at Ti_{5c} sites, Figure 5.1 shows the geometry proposed by Aschauer *et al*. In this study, the impact of H_2O vapour on the surface structure of $TiO_2(011)$ has been quantitatively determined. SXRD [11] has been employed for this purpose. The measurements taken here are a direct test of the *ab initio* predictions by Aschauer *et al* [10], and indeed the same interface geometry is observed in the presence of H_2O vapour ($p(H_2O) = 30$ mbar).

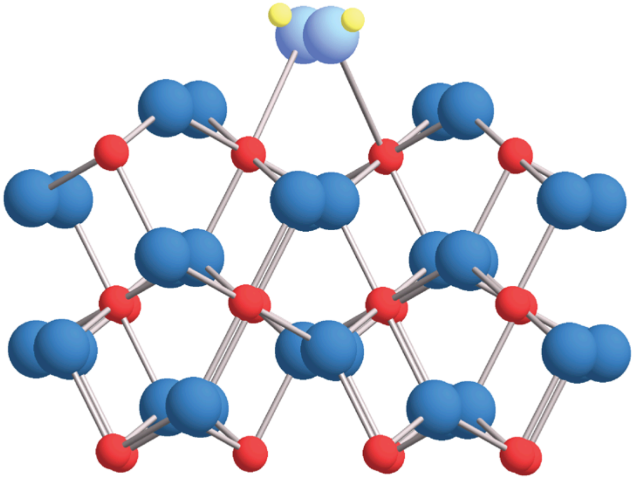

Figure 5.1: Schematic illustration of the OH/H_2O decorated (1×1) termination of the $TiO_2(011)$ surface predicted by Aschauer *et al*.

5.2. Experimental methods

Experimental work was performed at the Diamond Light Source, employing the Surface Village's off-line UHV chamber for sample preparation, and beam line I07 for SXRD measurements. *In situ* preparation of rutile $TiO_2(011)$ surface involved repeated cycles of Ar ion bombardment and annealing in vacuum to approximately 1150 K. During this process extensive surface characterisation was carried out using X-ray photoelectron spectroscopy (XPS), LEED, and STM to ensure the reliable formation of the (2×1) surface. In agreement with previous studies [3, 6, 8], following sample preparation, a sharp LEED pattern consistent with a (2×1) reconstruction was observed. Surface contamination following preparation was below the detection limit of XPS, and STM measurements taken at various sites on the sample surface were very much consistent with those typically acquired from this surface [9], presenting a well ordered, single phase (2×1) termination. A LEED pattern taken at ~ 54 eV following sample preparation and prior to SXRD measurements are shown in Figures 5.2. Following LEED and XPS measurements, a final cleaning cycle prior to acquisition of

SXRD data was conducted in order to eliminate the possibility of electron-induced surface damage.

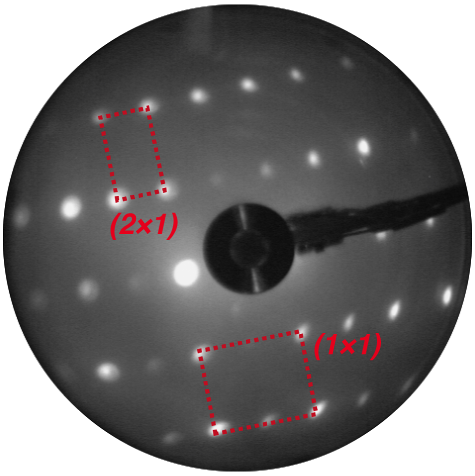

Figure 5.2: LEED pattern from $TiO_2(011)$ surface following sample preparation, taken at ~ 54 eV. Surface unit cells are indicated.

Once prepared, the sample was then transferred under vacuum to I07's (2+3) type diffractometer in experimental hutch 1 (EH1), using a custom-built vacuum-suitcase and UHV *baby* chamber combination (base pressure ~1.5×10^{-9} mbar). The *baby* chamber incorporates a dome shaped X-ray transparent beryllium window suitable for the collection of SXRD data, which were collected at room temperature at an incidence angle of 1°, a photon energy of $h\nu$ = 17.7 keV (wavelength 0.7 Å) and a 2D Pilatus photon detector. The sample was mounted such that the surface was in the horizontal plane.

A systematic series of X-ray reflections were acquired in stationary conditions (l-scans), for given integer values of (h, k), such scans are performed at a series of l-values, enabling profiles of scattered intensity versus perpendicular momentum transfer, known as crystal truncation rods (CTRs), to be compiled. Fractional order rods (FORs) containing information arising from the superstructure only and thus indicative of any surface reconstruction, in h and k, were also undertaken.

Subsequent to acquiring the dataset from the as-prepared $TiO_2(011)$ surface at UHV, $TiO_2(011)$-Clean$_{UHV}$, the leak valve was completely opened and the baby chamber simply backed filled with H_2O vapour (~ 30 mbar), the chamber's turbo molecular pump was switched off for measurements. A further systematic series of X-ray reflections were then acquired from the $TiO_2(011)$ surface at this H_2O partial pressure; henceforth this surface will be referred to as $TiO_2(011)$-H_2O_{30mbar}. Prior to allowing H_2O

(ultra-pure) into the vacuum chamber it was thoroughly degassed via freeze-thaw-pump cycles. Reference reflections at (h, k, l) = (-1, 0, 0.97) were recorded at regular intervals in order monitor surface degradation and eliminate the possibility of surface contamination within the data acquisition period. No significant changes were observed throughout the duration of the experiment.

5.3. Results and Discussion

To facilitate a fully quantitative structure determination, the raw diffraction data acquired at UHV and ~ 30 mbar H_2O partial pressure were integrated and corrected [12] to enable plots of structure factor versus perpendicular momentum transfer for each CTR and FOR measured. This procedure resulted in an extensive dataset totaling 10419 non-equivalent reflections from 21 CTRs and 23 FORs at UHV and 4978 non-equivalent reflections from 22 CTRs at ~30 mbar H_2O partial pressure. It should be noted that there was an absence of intensity in the FORs in the high-pressure regime suggestive of a loss of surface reconstruction. The measured data were indexed with reference to a monoclinic unit cell defined by lattice vectors ($\boldsymbol{a_1}, \boldsymbol{a_2}, \boldsymbol{a_3}$). Lattice vectors $\boldsymbol{a_1}$ and $\boldsymbol{a_2}$ are directed along the $[\bar{1}00]$ and the $[01\bar{1}]$ directions, respectively, and $\boldsymbol{a_3}$ lies in the plane defined by the $[01\bar{1}]$ and $[011]$ directions at an angle of $\theta = 2\times[\tan^{-1}(^{a}/_{c})]$ with respect to $\boldsymbol{a_2}$. The magnitudes of these lattice vectors are $\boldsymbol{a_1} = 2a$ and $\boldsymbol{a_2} = \boldsymbol{a_3} = \sqrt{(a^2 + c^2}$; where $a = 4.593$ and $c = 2.958$ are the lattice constants of the tetragonal rutile TiO_2 bulk unit cell [13]. Such a unit cell, rather than an orthorhombic unit cell with $\boldsymbol{a'_1}$, $\boldsymbol{a'_2}$ and $\boldsymbol{a'_3}$ (all orthogonal to one another) was employed for structure determination in order to minimize the number of parameters varied during refinement due to the large size of the c lattice constant of the orthorhombic unit cell. The corresponding reciprocal lattice vectors are denoted by h, k and l.

For surface structure elucidation, the usual approach of generating theoretical SXRD data for a potential structure, and then iteratively refining its geometry to find the best fit between experiment and theory was adopted. A modified version of the ROD software, originally written by Vleig *et al* [14], was used for this task. The goodness of fit is measured quantitatively by the reduced chi squared (χ^2) defined as follows [15]:

$$\chi^2 = \frac{1}{N-p}\sum_{i=1}^{N}\left(\frac{\left|F_i^{exp}(hkl)\right|^2 - \left|F_i^{th}(hkl)\right|^2}{\sigma_i^{exp}(hkl)}\right)^2 \tag{5.1}$$

where N is the number of measured structure factors, p is the number of independent parameters optimized during the fitting process, $F_{h,k,l}^{exp}$ are the experimentally measured structure factors, $F_{h,k,l}^{th}$ are the theoretically calculated structure factors, and $\sigma_{h,k,l}$ corresponds to the experimental uncertainties associated with $F_{h,k,l}^{exp}$.

A χ^2 value of ~1 is taken as an empirically validated indication of good agreement between the experiment and simulated structure i.e. the ideal structure is taken as the one that minimises this measure of discrepancy, since the difference between experiment and simulated data should be equal to the error in the data, $\sigma_{h,k,l}$. The agreement decreases with increasing χ^2.

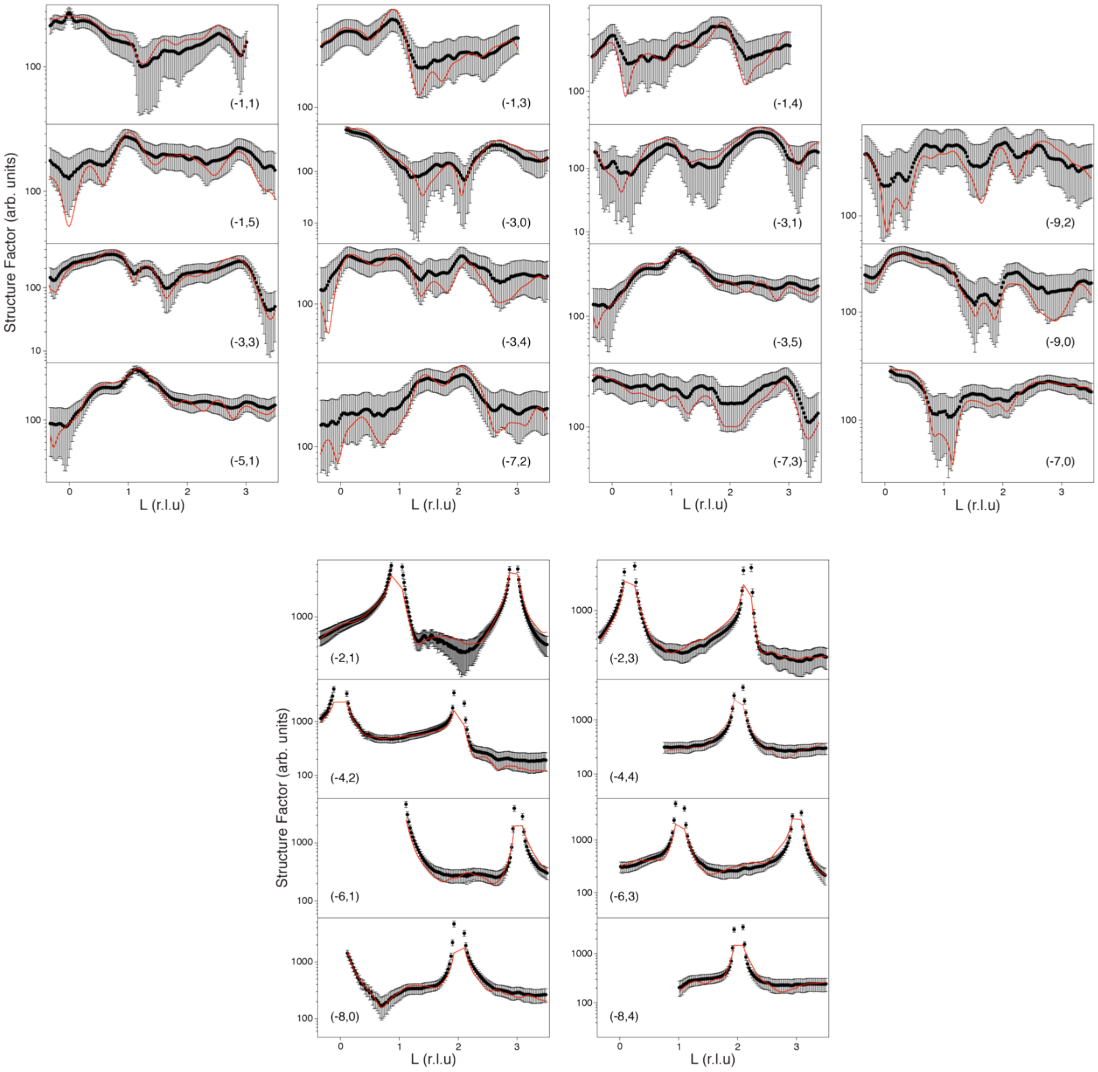

Figure 5.3: Comparison of experimental (black dots with error bars) and theoretically simulated (solid red line) FOR and CTR data acquired from TiO$_2$(011) in UHV . The red solid line indicate the optimum best fit (χ^2 = 1.03) structure proposed in this study. FOR data are displayed in the top four panels and CTR data in the bottom two panels.

Initial efforts focused on structure determination of the as-prepared UHV surface on the basis of the diffraction data acquired from TiO_2(011)-Clean$_{UHV}$. To begin the search for a structural solution, the clean surface termination resulting from recent quantitative SXRD [6, 7] and LEED-IV [8] studies were first considered. The best-fit model produced a χ^2 of 1.03, representing a very high degree of agreement between theory and experiment, the best fit is shown in Figure 5.3. In order to arrive to this solution 168 parameters were optimized, including 151 atomic displacements, 13 isotropic vibrational amplitudes (Debye-Waller factors), two scale factors (one for CTRs and one FORs), a surface fraction (the fraction of the surface that adopts the structure emerging from the analysis) and a surface roughness parameter. Figure 5.4 (middle) shows a ball and stick model of the surface geometry emerging from analysis of the SXRD data acquired from TiO_2(011)-Clean$_{UHV}$. Table 5.1 lists the atomic displacements for the optimum structure, expressed as displacements from the bulk-terminated TiO_2(011)(1×1) surface (depicted in Figure 5.4 (top)). Also listed are the displacements from bulk for the clean surface solution of Torrelles *et al* [6]. From comparison of atomic displacements in Table 5.1, it is clear, when taking into account the estimated errors, that the optimised structure obtained from the current SXRD measurements, TiO_2-Clean$_{UHV}$, is in excellent quantitative agreement with that derived in the earlier clean surface SXRD [6] study. All atomic occupancies remained fixed at 1. The Debye Waller factors all adopted reasonable values for both Ti and O atoms where the highest values corresponded to the top most atoms (Ti(1) = 0.87, O(1) = 5.36), decreasing with each layer through the model to their bulk values (Ti = 0.1, O = 0.25). The roughness parameter, calculated using the approximate beta model [16], for the optimised structure was very small ($\beta = 0.09$) indicating a very flat surface. This is in agreement with the STM images obtained prior to the SXRD experiment which show large flat terraces with an approximate area of individual terraces 25000 nm^2 in size and with apparent monatomic steps heights of 0.25 nm. The surface fraction parameter is 97.6%, indicating that essentially the entire surface adopts the structure obtained in this analysis.

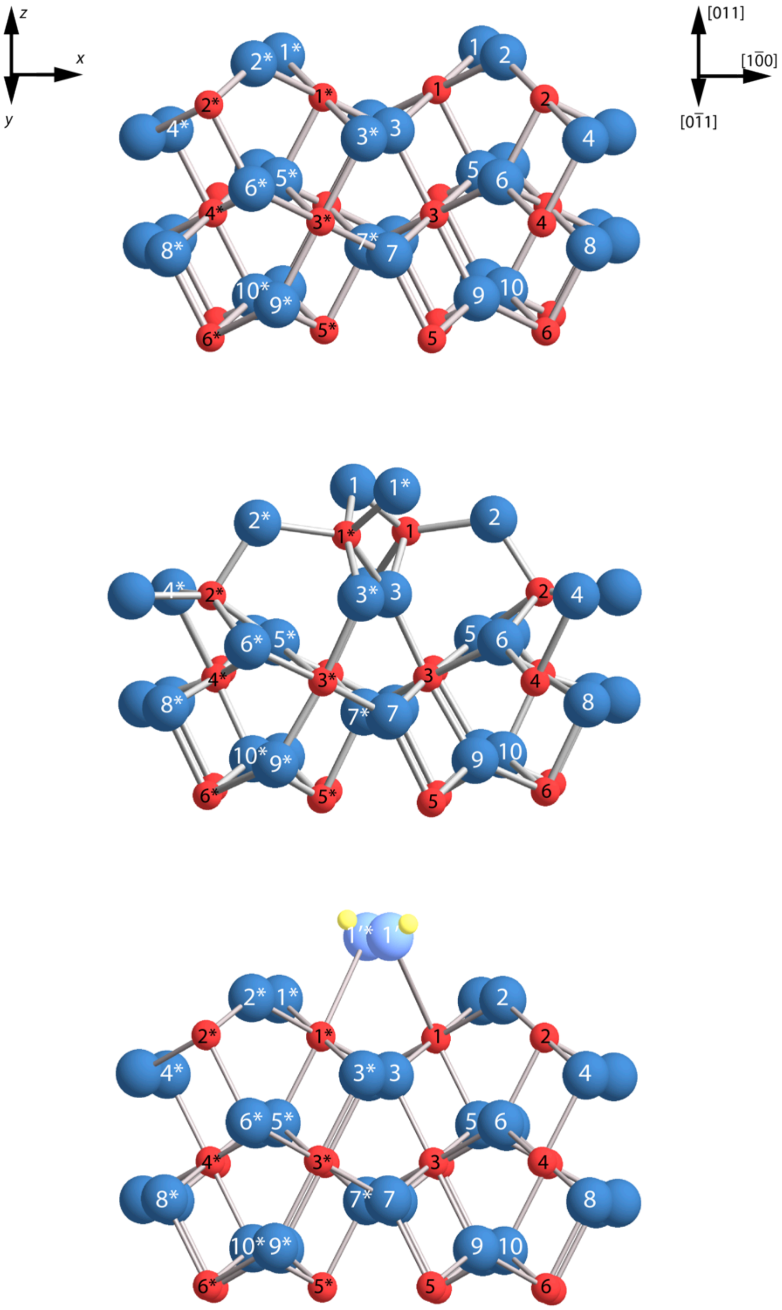

Figure 5.4: Ball and stick models of the ideal bulk truncated TiO_2(011)(1×1) (top), the optimum TiO_2(011)(2×1) geometry (middle) and the optimised TiO_2(011)(1×1) structure at ~30 mbar H_2O (bottom). Larger (smaller) spheres are oxygen (titanium) atoms. The numerical labelling of the atoms is employed in Table 5.1 and 5.2 for identification purposes. Symmetry paired atoms are denoted by an asterisk (*).

Table 5.1: Optimized locations of atoms in the TiO_2(011)(2×1) reconstruction, expressed as displacements from the bulk-terminated TiO_2(011)(1×1) surface, resulting from analysis of the SXRD

data presented in Figure 5.3 (current study) - TiO_2-Clean$_{UHV}$. Also listed are values obtained from the clean surface structure proposed by Torrelles *et al* [6], and (x, y, z) atomic coordinates for the bulk-truncated structure of TiO_2(011)(1×1). Figure 5.4 provides a key to the identity of the atoms. A positive value for x, y, and z indicates a displacement in the $[\bar{1}00]$, $[01\bar{1}]$, and [011] directions, respectively.

Atom	(1 x 1) bulk terminated (x, y, z) coordinates (Å)	Displacement (Å)		
		Δx [6] : TiO_2-Clean$_{UHV}$	Δy [6] : TiO_2-Clean$_{UHV}$	Δz [6] : TiO_2-Clean$_{UHV}$
O(1)	2.04, 1.55, 0.76	-2.52 ± 0.02: -2.48 ± 0.02	2.90 ± 0.02: 2.91 ± 0.03	0.62 ± 0.02: 0.59 ± 0.03
O(2)	2.55, 4.28, 0.76	-0.15 ± 0.02: -0.12 ± 0.02	-0.29 ± 0.02: -0.31 ± 0.02	-0.06 ± 0.02: -0.16 ± 0.03
Ti(1)	1.15, 0.00, 0.00	-0.56 ± 0.01: -0.56 ± 0.01	0.32 ± 0.01: 0.32 ± 0.01	0.43 ± 0.01: 0.42 ± 0.01
Ti(2)	3.44, 2.73, 0.00	-0.09 ± 0.02: -0.08 ± 0.01	-1.76 ± 0.02: -1.76 ± 0.01	-0.80 ± 0.02: -0.77 ± 0.01
O(3)	0.25, 3.91, -0.76	0.00 ± 0.02: -0.05 ± 0.01	0.27 ± 0.02: 0.27 ± 0.03	-0.06 ± 0.02: -0.04 ± 0.03
O(4)	4.34, 1.18, -0.76	-0.15 ± 0.02: -0.11 ± 0.01	0.42 ± 0.02: 0.43 ± 0.03	-0.01 ± 0.02: 0.01 ± 0.03
O(5)	2.04, 5.41, -1.73	0.00 ± 0.01: 0.05 ± 0.01	-0.04 ± 0.01: 0.02 ± 0.02	-0.06 ± 0.01: -0.08 ± 0.02
O(6)	2.55, 2.68, -1.73	0.03 ± 0.01: 0.01 ± 0.01	-0.27 ± 0.02: -0.23 ± 0.02	-0.06 ± 0.01: -0.04 ± 0.02
Ti(3)	1.15, 3.86, -2.49	-0.10 ± 0.01: -0.17 ± 0.01	-0.05 ± 0.01: -0.03 ± 0.01	-0.06 ± 0.01: -0.07 ± 0.01
Ti(4)	3.44, 1.13, -2.49	-0.12 ± 0.01: -0.17 ± 0.01	-0.27 ± 0.01: -0.27 ± 0.01	-0.07 ± 0.01: -0.04 ± 0.01
O(7)	0.25, 2.31, -3.25	0.04 ± 0.01: 0.06 ± 0.01	0.00 ± 0.02: 0.05 ± 0.02	-0.05 ± 0.01: -0.01 ± 0.01
O(8)	4.34, 5.04, -3.25	-0.02 ± 0.01: -0.08 ± 0.01	0.07 ± 0.02: 0.05 ± 0.02	0.12 ± 0.01: 0.11 ± 0.01
O(9)	2.04, 3.81, -4.22	-0.02 ± 0.01: 0.01 ± 0.01	-0.06 ± 0.02: -0.04 ± 0.02	-0.04 ± 0.01: -0.07 ± 0.01
O(10)	2.55, 6.54, -4.22	0.00 ± 0.01: -0.03 ± 0.01	-0.03 ± 0.02: -0.06 ± 0.02	0.00 ± 0.01: -0.02 ± 0.01
Ti(5)	1.15, 2.26, -4.98	0.02 ± 0.01: 0.01 ± 0.01	-0.06 ± 0.01: -0.06 ± 0.01	-0.11 ± 0.01: -0.10 ± 0.01
Ti(6)	3.44, 5.00, -4.98	0.01 ± 0.01: 0.04 ± 0.01	0.04 ± 0.01: 0.04 ± 0.01	0.05 ± 0.01: 0.06 ± 0.01

Turning to elucidation of the TiO_2(011) surface structure at $p(H_2O)$ ~ 30 mbar, TiO_2-H_2O_{30mbar}, initially structure determination began with refinement of the atomic coordinates along with various nonstructural parameters of a model similar to the optimised TiO_2-H_2O_{UHV} structure. This is because, as mentioned above, intensity in the FORs under the high pressure regime has reduced to the background level and thus the model here simulates a 'disordered' (2×1) reconstruction in which both (1×1) and (2×1) domains are accounted for by different occupancy parameters. A χ^2 of 3.6 was obtained. This value clearly in no way represents a reasonable agreement between theory and experiment, indicating that the presence of ambient H_2O leads to more than just relaxations of TiO_2 surface atoms. During the fit the occupancy of the (2x1) domains tended to a value close to zero. This, coupled with the lack of intensity in the FORs, leads us to believe that the surface must exhibit a (1×1) termination. On this basis, guided by the *ab initio* predictions of Aschauer *et al* [10], an alternative solution was sought. They predicted a model in which the clean UHV surface undergoes a transformation from a (2×1) reconstructed surface to a (1×1) structure. This surface is thought to be decorated with a monolayer of adsorbed OH/H_2O tightly bound with alternating orientations at under-coordinated surface titanium (Ti_{5c}) sites in the presence of an aqueous environment. A χ^2 of 1.29 was obtained for this optimum geometry, which represents a good agreement between theory and experiment. This fit is illustrated in Figure 5.5, showing the experimental CTRs (black errors bars) and best-fit theoretical simulations for the optimum TiO_2-H_2O_{30mbar} structure (red line). Removal of the adsorbed OH/H_2O increases the χ^2 to 1.55, indicating that the data are sensitive to the presence of this atom, visually evident in Figure 5.5 (blue dashed line).

The optimum TiO_2-H_2O_{30mbar} surface structure atomic coordinates, expressed as displacements from the bulk-terminated TiO_2(011)(1×1) surface, resulting from analysis of the SXRD data presented in Figure 5.5, are listed in Table 5.2. A total of 91 parameters were optimised during structure refinement process, i.e. 78 atomic coordinates, 10 vibrational amplitudes (Debye-Waller factors), a scale factor, a surface roughness parameter, and a surface fraction parameter. Due to symmetry constraints equivalent atoms where confined to the same magnitude displacements both in and out of plane. The surface fraction parameter is 91.3%, which much like the clean surface solution suggests that essentially the entire surface adopts the structure obtained in this analysis. As regards to the remaining 8.7% of the surface, this could comprise of surface defects. The optimum roughness parameter was $\beta = 0.15$, which implies that the presence of H_2O induces roughening of the surface. This increase in surface roughness in this higher partial pressure of H_2O regime is believed to be due to a combination of the change in the substrate termination and a manifestation of the dynamic nature of the water over-layer [10].

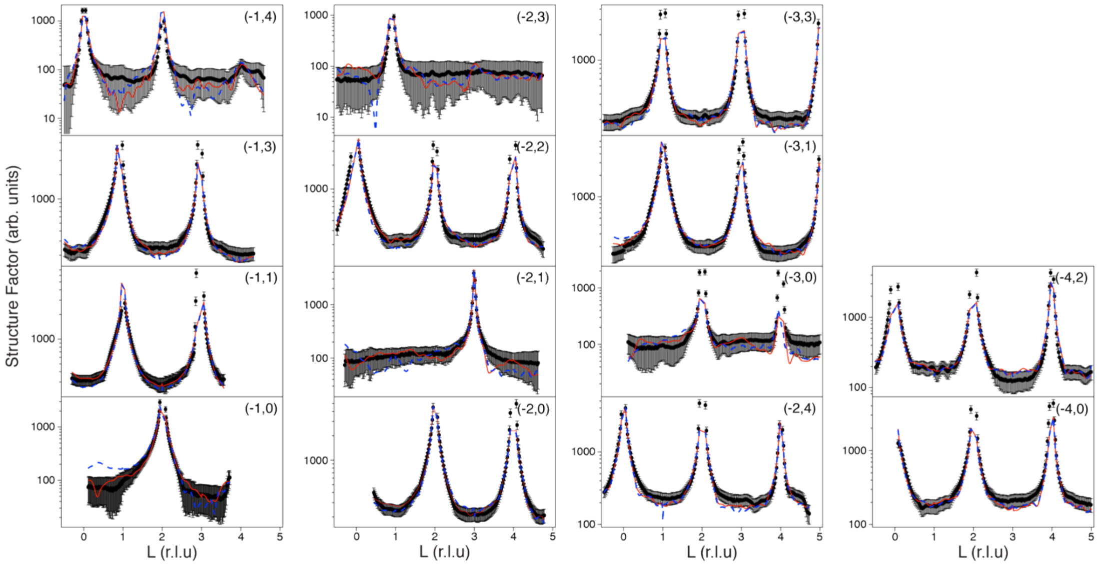

Figure 5.5: Comparison of experimental CTR data (solid markers with error bars), acquired from the TiO_2(011) surface at $p(H_2O)$ ~ 30 mbar (TiO_2-$H_2O_{30\ mbar}$), and theoretical best-fit simulations (solid red lines). Also included are theoretically simulated data (broken blue line) for optimum TiO_2-H_2O_{UHV} geometry

Turning to the nature of the adsorbed oxygen specie, X-ray scattering strength is proportional to the electron density, and thus it is extremely difficult in an SXRD experiment to distinguish directly between H_2O, OH, and O on the TiO_2(011) surface, because of the low scattering contribution from hydrogen. Consequently, the only way to distinguish between adsorbed H_2O and OH is through variation in the Ti-O adsorbate bond length; a difference of ~ 0.2 Å (1.83 Å for Ti-OH and 2.03 Å for Ti-H_2O) as concluded in the theoretical calculations [10], and a Ti-OH bond length of 1.85 ± 0.09 Å has been concluded experimentally on the TiO_2(110) surface [17]. The Ti-OH/H_2O bond length has been determined as 1.94 ± 0.02 Å in this study, which is precisely in-between the Ti-OH and Ti-H_2O bond lengths proposed by theory, although it can be argued that it is within the error of the Ti-OH bond length as determined by experiment. As a check to better define the chemical nature of the water moiety, a model in which two the bond length was fixed to values indicative of Ti-OH bond lengths (1.85 Å) up to values typically associated with the Ti-H_2O bond length (2.15 Å), at intervals of 0.05 Å, and the structure optimized. Analysis of Figure 5.6 shows that varying the bond length from 1.85 Å to 2.15 Å results in a $\Delta\chi^2$ of only 0.06, suggesting that it is not possible to clearly define the chemical nature of this water moiety. Further yet, Aschauer *et al* report that during their simulations a constant dissociation or reassociation of water molecules occurred leading to an apparent mixed dissociated/molecular adsorption state. On this basis and the fact that quite possibly the water overlayer at the interface is not necessarily ordered enough for a for SXRD to discriminate between OH and H_2O, it can be logically concluded here that for the $TiO_2(011)$ surface at $p(H_2O)$ ~ 30 mbar a mixed dissociated/molecular overlayer is favoured.

Considerable structural changes to the optimised $TiO_2(011)(2\times1)$ UHV geometry were required to achieve this fit, specifically the uppermost surface atoms (O(1), O(2), Ti(1) and Ti(2)), as apparent from Table 5.2. Although we are unable to comment on the mechanism by which this transformation occurs on the basis of SXRD data, nevertheless a mechanism has been proposed by Aschauer *et al* in which, over a long enough period of time, in the presence of water the surface 'slowly' undergoes a series of water dissociation events at (2×1) valley titanium sites with subsequent strong outwards relaxations of valley titanium atoms leading the fully OH/H_2O decorated (1×1) surface termination found in that and the present studies.

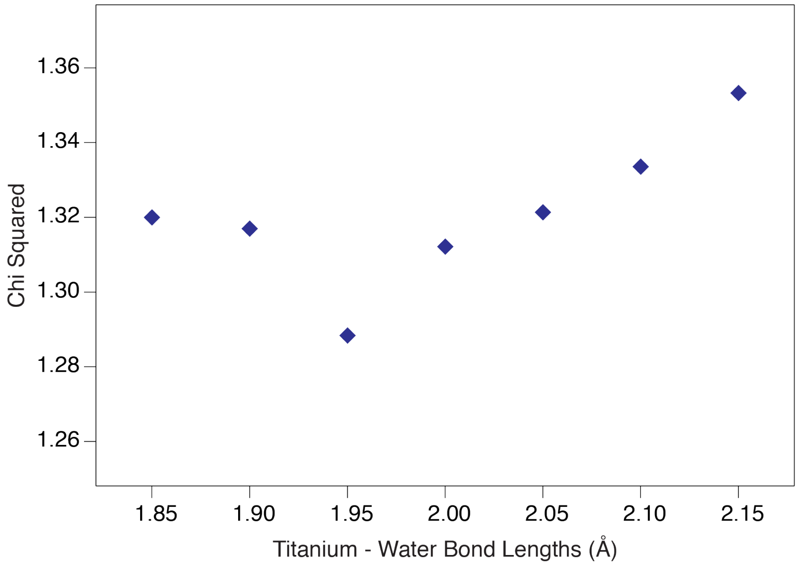

Figure 5.6: Plot of χ^2 against Ti – OH/H_2O bond length.

Table 5.2: Optimized locations of atoms comprising the TiO_2-H_2O_{30mbar} surface, expressed as displacements from the bulk-terminated $TiO_2(011)(1\times1)$ surface, resulting from analysis of the data presented in Figure 5.5. (*x*, *y*, *z*) atomic coordinates for the TiO_2-$Clean_{UHV}$ surface and for the bulk-truncated $TiO_2(011)(1\times1)$ surface are also listed. Figure 5.4 provides a key to the identity of the atoms.

The oxygen atoms of adsorbed OH/H_2O species are labelled O′. A positive value for x, y, and z indicates a displacement in the $[\bar{1}00]$, $[01\bar{1}]$, and $[011]$ directions, respectively.

Atom	(1 x 1) bulk terminated (x, y, z) coordinates (Å)	Displacement (Å)		
		Δx TiO_2-$Clean_{UHV}$: TiO_2-H_2O_{30mbar}	Δy TiO_2-$Clean_{UHV}$: TiO_2-H_2O_{30mbar}	Δz TiO_2-$Clean_{UHV}$: TiO_2-H_2O_{30mbar}
O′	0.25, 0.05, 1.73	N/A: -0.04 ± 0.02	N/A: -0.15 ± 0.03	N/A: 0.01 ± 0.01
O(1)	2.04, 1.55, 0.76	-2.48 ± 0.02: -0.01 ± 0.02	2.91 ± 0.03: -0.01 ± 0.02	0.59 ± 0.03: 0.09 ± 0.02
O(2)	2.55, 4.28, 0.76	-0.12 ± 0.02: 0.01 ± 0.02	-0.31 ± 0.02: -0.01 ± 0.02	-0.16 ± 0.03: 0.09 ± 0.02
Ti(1)	1.15, 0.00, 0.00	-0.56 ± 0.01: 0.05 ± 0.01	0.32 ± 0.01: -0.01 ± 0.01	0.42 ± 0.01: 0.02 ± 0.01
Ti(2)	3.44, 2.73, 0.00	-0.08 ± 0.01: -0.05 ± 0.01	-1.76 ± 0.01: -0.01 ± 0.01	-0.77 ± 0.01: 0.02 ± 0.01
O(3)	0.25, 3.91, -0.76	-0.05 ± 0.01: -0.02 ± 0.01	0.27 ± 0.03: -0.10 ± 0.02	-0.04 ± 0.03: 0.10 ± 0.02
O(4)	4.34, 1.18, -0.76	-0.11 ± 0.01: 0.02 ± 0.01	0.43 ± 0.03: -0.10 ± 0.02	0.01 ± 0.03: 0.10 ± 0.02
O(5)	2.04, 5.41, -1.73	0.05 ± 0.01: 0.03 ± 0.01	0.02 ± 0.02: 0.01 ± 0.01	-0.08 ± 0.02: -0.08 ± 0.02
O(6)	2.55, 2.68, -1.73	0.01 ± 0.01: -0.03 ± 0.01	-0.23 ± 0.02: 0.01 ± 0.01	-0.04 ± 0.02: -0.08 ± 0.02
Ti(3)	1.15, 3.86, -2.49	-0.17 ± 0.01: -0.03 ± 0.01	-0.03 ± 0.01: -0.03 ± 0.01	-0.07 ± 0.01: 0.03 ± 0.01
Ti(4)	3.44, 1.13, -2.49	-0.17 ± 0.01: 0.03 ± 0.01	-0.27 ± 0.01: -0.03 ± 0.01	-0.04 ± 0.01: 0.03 ± 0.01
O(7)	0.25, 2.31, -3.25	0.06 ± 0.01: 0.01 ± 0.01	0.05 ± 0.02: -0.01 ± 0.01	-0.01 ± 0.01: 0.01 ± 0.01
O(8)	4.34, 5.04, -3.25	-0.08 ± 0.01: -0.01 ± 0.01	0.05 ± 0.02: -0.01 ± 0.01	0.11 ± 0.01: 0.01 ± 0.01
O(9)	2.04, 3.81, -4.22	0.01 ± 0.01: 0.01 ± 0.01	-0.04 ± 0.02: 0.01 ± 0.01	-0.07 ± 0.01: -0.03 ± 0.01
O(10)	2.55, 6.54, -4.22	-0.03 ± 0.01: -0.01 ± 0.01	-0.06 ± 0.02: 0.01 ± 0.01	-0.02 ± 0.01: -0.03 ± 0.01
Ti(5)	1.15, 2.26, -4.98	0.01 ± 0.01: -0.01 ± 0.01	-0.06 ± 0.01: -0.02 ± 0.01	-0.10 ± 0.01: 0.02 ± 0.01
Ti(6)	3.44, 5.00, -4.98	0.04 ± 0.01: 0.01 ± 0.01	0.04 ± 0.01: -0.02 ± 0.01	0.06 ± 0.01: 0.02 ± 0.01

5.4. Conclusion

In summary, high precision SXRD data acquired from clean $TiO_2(011)$ surface and at a $p(H_2O)$ of ~ 30 mbar has been analysed. The optimised clean surface in vacuum geometry, (2×1) reconstruction, is same as that emerging from recent quantitative studies [6-8]. More specifically SXRD measurements from this study are a very close match to those reported by Torrelles *et al* [6], with almost all atomic displacements and site occupations being essentially identical. Prompted by *ab initio* calculations [10], the geometry of the $TiO_2(011)$/ H_2O interface has also been elucidated very precisely. Structural optimisation has yielded a best-fit solution consistent with these *ab initio* calculations, in which the surface reverts to a (1×1) structure at a $p(H_2O)$ of ~ 30 mbar. Most notably, the outcome of this structure determination indicates that the relative stabilities of the reconstructed and bulk-like (1×1) surface terminations are reversed in the presence of water. It has been suggested that these results are of direct relevance to the atomic scale understanding of the enhanced photo-catalytic activity displayed by the $TiO_2(011)$ surface specifically in the aqueous environments that more closely resemble 'real world' photocatalytic applications.

5.5. References

[1] C.L. Pang, R. Lindsay, G. Thornton, Structure of Clean and Adsorbate-Covered Single-Crystal Rutile TiO_2 Surfaces, Chemical Reviews, 113 (2013) 3887-3948.

[2] T. Ohno, K. Sarukawa, M. Matsumura, Crystal faces of rutile and anatase TiO_2 particles and their roles in photocatalytic reactions, New Journal of Chemistry, 26 (2002) 1167-1170.

[3] O. Dulub, C.D. Valentin, A. Selloni, U. Diebold, Structure, defects, and impurities at the rutile $TiO_2(011)$-(2×1) surface: A scanning tunneling microscopy study, Surface Science, 600 (2006) 4407-4417.

[4] T.J. Beck, A. Klust, M. Batzill, U. Diebold, C. Di Valentin, A. Selloni, Surface Structure of $TiO_2(011)$-(2×1), Physical Review Letters, 93 (2004) 036104.

[5] T. Kubo, H. Orita, H. Nozoye, Surface Structures of Rutile $TiO_2(011)$, Journal of the American Chemical Society, 129 (2007) 10474-10478.

[6] X. Torrelles, G. Cabailh, R. Lindsay, O. Bikondoa, J. Roy, J. Zegenhagen, G. Teobaldi, W.A. Hofer, G. Thornton, Geometric Structure of $TiO_2(011)(2\times1)$, Physical Review Letters, 101 (2008) 185501.

[7] X.-Q. Gong, N. Khorshidi, A. Stierle, V. Vonk, C. Ellinger, H. Dosch, H. Cheng, A. Selloni, Y. He, O. Dulub, U. Diebold, The 2×1 reconstruction of the rutile $TiO_2(011)$ surface: A combined density functional theory, X-ray diffraction, and scanning tunneling microscopy study, Surface Science, 603 (2009) 138-144.

[8] S.E. Chamberlin, C.J. Hirschmugl, H.C. Poon, D.K. Saldin, Geometric structure of $TiO_2(011)(2\times1)$ surface by low energy electron diffraction (LEED), Surface Science, 603 (2009) 3367-3373.

[9] T. Woolcot, G. Teobaldi, C.L. Pang, N.S. Beglitis, A.J. Fisher, W.A. Hofer, G. Thornton, Scanning Tunneling Microscopy Contrast Mechanisms for TiO_2, Physical Review Letters, 109 (2012) 156105.

[10] U. Aschauer, A. Selloni, Structure of the Rutile $TiO_2(011)$ Surface in an Aqueous Environment, Physical Review Letters, 106 (2011) 166102.

[11] P. Coppens, D. Cox, E. Vlieg, I.K. Robinson, Synchrotron radiation crystallography, Academic Press 1992.

[12] E. Vlieg, A (2+3)-Type Surface Diffractometer: Mergence of the z-Axis and (2+2)-Type Geometries, Journal of Applied Crystallography, 31 (1998) 198-203.

[13] A.F. Wells, Structural inorganic chemistry, Clarendon Press, 1984.

[14] E. Vlieg, ROD: a program for surface X-ray crystallography, Journal of Applied Crystallography, 33 (2000) 401-405.

[15] I.K. Robinson, D.J. Tweet, Surface X-ray diffraction, Reports on Progress in Physics, 55 (1992) 599.

[16] I.K. Robinson, Crystal truncation rods and surface roughness, Physical Review B, 33 (1986) 3830-3836.

[17] D.A. Duncan, F. Allegretti, D.P. Woodruff, Water does partially dissociate on the perfect TiO_2(110) surface: A quantitative structure determination, Physical Review B, 86 (2012) 045411.

Chapter 6

Substrate preparation for surface studies under non-UHV conditions

6.1 Introduction

A recent special issue of Surface Science was devoted to the topic of '*Surface science under environmental conditions*'. In the introductory editorial it was indicated that researchers in fundamental surface science are becoming increasingly concerned with more complex systems and conditions [1]. Focussing on the latter area, greater complexity largely involves a move away from ultra high vacuum (UHV) work to studies in more technologically pertinent environments, i.e. measurements performed with samples immersed in fluids (gases or liquids). An issue of interest associated with such effort is reliable preparation of well-defined substrate surfaces. One route is simply to prepare the sample under UHV conditions, and then introduce the fluid. Alternatively, a non-UHV recipe may be adopted. This second option is attractive as it potentially eliminates the requirement for UHV facilities, although substrate characterisation is still required to adhere strictly to a rigorous '*surface science approach*'. Furthermore, application of non-UHV processing may reveal previously unknown substrate terminations, which could have more '*real-world*' relevance. Here, we contribute to this topic through presenting a non-UHV recipe for the prototypical metal oxide surface for fundamental surface science, rutile-$TiO_2(110)$, as well as for the non-equivalent rutile-$TiO_2(011)$ surface [2].

To date, a number of non-UHV approaches for preparation of low Miller index single-crystal TiO_2 surfaces have been implemented [3-12]. Despite varying in detail, almost all of these recipes can be labelled as so called *wet-chemical* procedures, involving a combination of chemical cleaning/etching and high temperature annealing [3-5, 7-12]. Hydrofluoric acid (HF) [3-5, 7, 9-11], as well as other acidic reagents [8, 12], has been successfully employed for the former step. Concerning such preparation of $TiO_2(110)$, substrate characterisation subsequent to processing indicates the feasibility of forming a relatively clean, well-ordered (1×1) surface termination with significant terrace sizes (widths can be > 100 nm) [4, 7-9, 11]. A similar positive outcome has been achieved for the (011) surface of rutile-TiO_2 [9-11], with both (1×1) [11] and (2×1) [9] surface unit cells being observed; a (2×1) reconstruction is found following preparation in UHV [2].

In this chapter, a somewhat modified *wet-chemical* recipe for the preparation of single crystal surfaces of TiO_2 is described, and applied to both rutile-TiO_2(110) and rutile-TiO_2(011). The utility of this procedure is evaluated through detailed surface characterisation. Atomic force microscopy (AFM) and scanning tunneling microscopy (STM) are employed to assess surface topography, with low energy electron diffraction (LEED) probing surface order. Auger electron spectroscopy (AES) is applied to determine surface composition/cleanliness. Besides demonstrating the potential of our recipe for production of well-defined TiO_2 surfaces, a previously unreported termination is found for TiO_2(011). As a means of further surface structure exploration preliminary surface X-ray diffraction (SXRD) data from the (011) surface are also presented and compared with CTR's from the UHV prepared surface of Torrelles *et al* [13].

6.2 Materials and methods

Experimental work was undertaken with single crystal samples of (110) and (011) oriented rutile-TiO_2 sourced from PI-KEM. Typically, samples measured 10 mm × 10 mm × 1 mm, with an off-cut accuracy of ≤ 1°. *Wet-chemical* preparation of these substrates involved 4 steps (***STEPS 1-4***), beginning with sonication (~ 15 min duration) in a sequence of solvents, i.e. acetone, ethanol, and deionised water. Samples were then dried in a stream of nitrogen. The purpose of this first stage (***STEP 1***) is to remove any adhered debris and grease from the surfaces of the substrates.

Following ***STEP 1***, preparation continued with an anneal in air in a tube furnace at 973 K for ~ 90 min; identical annealing conditions were adopted for both the (110) and (011) surfaces on the basis of empirical trials. The objective of this heat treatment (***STEP 2***), which is analogous to that of the same procedure in UHV, is to form flat, well-ordered surfaces. Upon cooling to room temperature, samples were immersed in aqua regia (3:1 (volume ratio) mixture of HCl and HNO_3) for ~ 45 min, and then rinsed thoroughly with deionised water. Surface contamination removal is the target of this procedure (***STEP 3***).

Finally, samples were inserted into a UV-ozone cleaner (Novascan). Substrates were exposed to UV-light for 20 min, and left immersed in the locally generated ozone atmosphere for another 30 min. This ultimate step (***STEP 4***) is intended to eliminate adventitious carbon from the substrate surface [14]. To ascertain that the UV-treatment is having an impact on the substrate, water droplet contact angle data were acquired with a FTÅ188 contact angle and surface tension analyzer (First Ten Ångstroms Inc.). These measurements were undertaken with deionised water, using the static sessile drop approach [15]. On the basis of previous work [4], a hydrophobic to hydrophilic transition is expected to occur following effective UV-exposure.

Concerning surface characterisation, data were acquired at various points in the preparation sequence (***STEPS 1-4***). AFM images were recorded in air at room temperature with a Nanoscope IIIa Multimode AFM (Digital Instruments) in tapping mode. STM images were acquired using an omicron low temperature STM in constant current mode. Note that due to the insulating nature of TiO_2 STM measurements on the (110) surface were carried out using a niobium (Nb) doped (0.2-0.5 wt. % *n*-doped) crystal, also sourced from Pi-Kem; the reason why STM data can be measured on UHV prepared TiO_2 without the need for the sample to be (niobium) doped has been discussed in Chapter 3. For AES and LEED measurements, samples were inserted through a load-lock into an appropriately equipped UHV chamber; a four-grid rear view LEED optics (VG) was employed to collect both spectroscopy and diffraction data. Sample charging was an issue during acquisition of both AES and LEED data, due to the insulating nature of the *wet-chemically* prepared samples; UHV preparation (annealing) leads to bulk reduction of TiO_2, eliminating charging. To compensate for such charging effects in AES spectra, the kinetic energy (KE) scale was calibrated using the location of the O *KLL* feature reported previously for TiO_2 [14].

SXRD data for the $TiO_2(011)$ surface was collected at Diamond using the Surfaces and Interfaces beamline, I07, with the sample surface mounted in the horizontal plane using a (2+3) diffractometer. Measurements were performed with the substrate at room temperature employing a 2D Pilatus photon detector with an X-ray angle of incidence angle of 1.0° and photon energy of $h\nu = 17.7$ keV.

6.3 Results and Discussion

Figures 6.1 (a) and (b) show typical AFM images of $TiO_2(110)$ and $TiO_2(011)$, respectively, acquired subsequent to UV-treatment (***STEP 4***). Mimicking previous work [4, 7, 9-11], both surfaces exhibit relatively large, flat terraces, separated by well-defined steps; terraces are somewhat larger on the (110) surface, which is most likely a result of a smaller off-cut angle for this substrate. It should be noted that we attribute the small variations in intensity within terraces in Figure 6.1 to instrumental noise, rather than any significant topographical features. Concerning step heights, the smallest, and most prevalent, measures ~ 0.3 nm on $TiO_2(110)$ (see line profile in Figure 6.1 (c)), which is consistent with the value expected for a monatomic step (0.33 nm) separating equivalent terraces [9]. Monatomic steps (~ 0.25 nm) [10] are also observed on the (011) surface (see line profile in Figure 6.1 (d)). Larger step heights apparent on both surfaces can be simply reconciled with multiple monatomic steps, e.g. the ~ 0.6 nm step height in the line profile from $TiO_2(110)$ (Figure 6.1 (c)) is consistent with a double monatomic step. It should be emphasised, given the limited lateral resolution, that it is not possible to determine the precise morphology of these deeper steps, e.g. they may consist of a series of closely spaced single monatomic steps with narrow intervening terraces.

AFM images (not shown) recorded following aqua regia immersion (***STEP 3***) are essentially identical to those displayed in Figure 6.1. These data indicate that UV-treatment (***STEP 4***) does not have any significant impact on surface topography. Images acquired post annealing (***STEP 2***), but before aqua regia immersion (***STEP 3***), typically display a significantly greater degree of undulation within terraces, as demonstrated by the image of $TiO_2(110)$ in Figure 6.2 (a) and the corresponding line profile (Figure 6.2 (b)). We suggest that the origin of this morphology is most likely surface contamination, which is removed by the acid cleaning. Prior to annealing (***STEP 2***), AFM revealed very rough surfaces, with no clear terraces or steps apparent.

STM images of *wet chemically* prepared Nb-$TiO_2(110)$ acquired subsequent to UV-treatment are displayed in Figure 6.3 (a) and (b). Much like the AFM images, these images show that surfaces exhibit relatively large, flat terraces, separated by well-defined steps. Line profiles along the surface show that equivalent terraces are separated by steps measuring ~ 0.35 nm in height, which is again consistent with a monatomic step. However, it has been very difficult to image this surface in STM and to date no ultra high-resolution images have been achieved, and hence one cannot obtain details of terrace structure at the atomic scale.

Turning to surface composition, AES spectra are displayed in Figure 6.4 of (a) $TiO_2(110)$ and (b) $TiO_2(011)$. In each panel there are two spectra, one acquired subsequent to aqua regia immersion (***STEP 3***), and the other post UV-treatment (***STEP 4***). All of the spectra exhibit features expected of the substrate, i.e. Ti *LMM* and O *KLL* Auger peaks. Additionally, a feature assigned to the C *KLL* Auger peak is apparent in the two spectra acquired after aqua regia immersion (***STEP 3***). This signal is attributed to surface adsorbed adventitious carbon. As indicated by the corresponding spectra, UV-treatment (***STEP 4***) essentially quenches this carbon peak, i.e. this step removes adventitious carbon from the substrate surface, as intended.

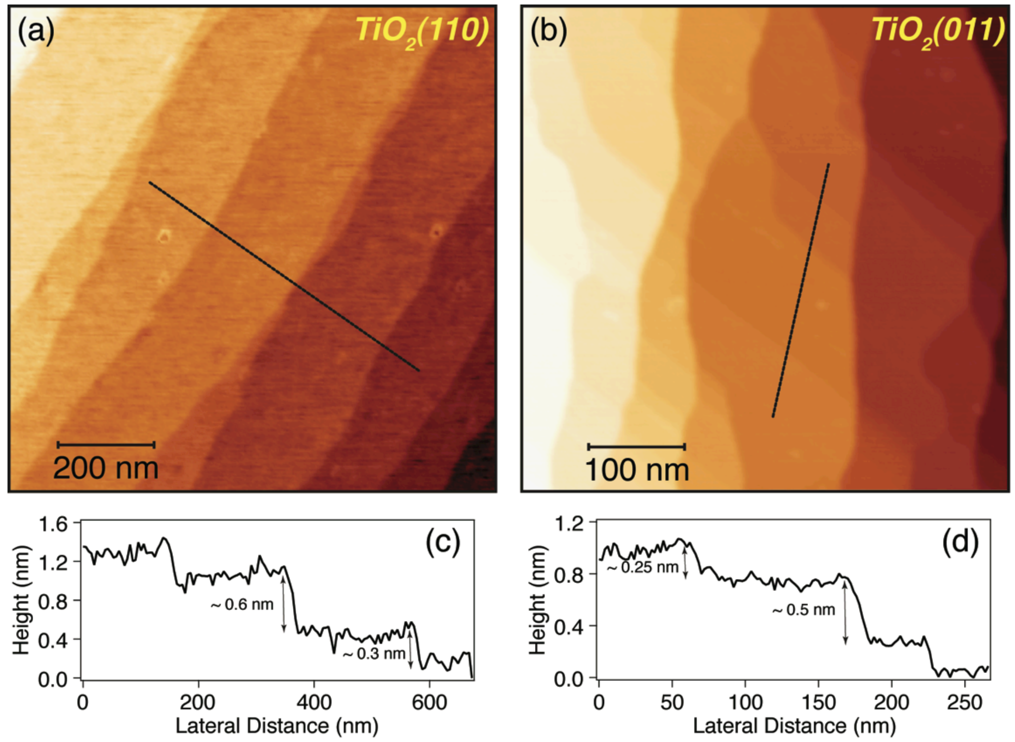

Figure 6.1: AFM images of (a) $TiO_2(110)$ and (b) $TiO_2(011)$ acquired subsequent to *STEP 4* (UV-treatment) of the *wet chemical* preparation procedure. (c) and (d) display line profiles from along the broken lines indicated in (a) and (b), respectively.

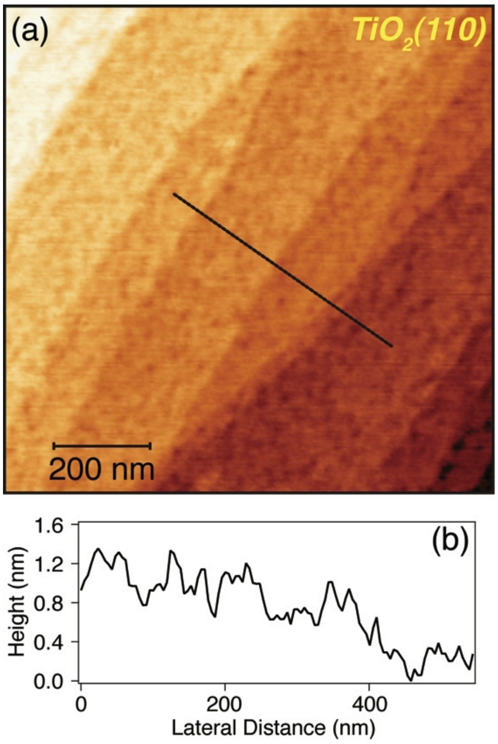

Figure 6.2: AFM image of TiO_2(110) acquired subsequent to *STEP 2* (annealing) of the *wet chemical* preparation procedure. (b) displays a line profile from along the broken line indicated in (a).

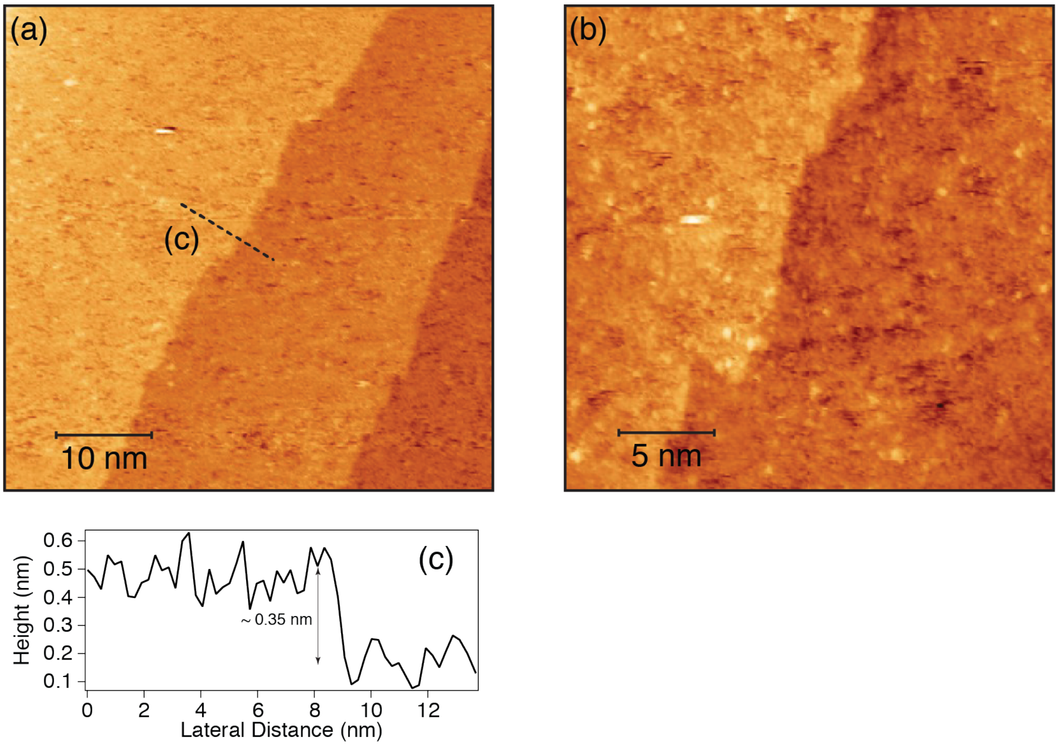

Figure 6.3: STM images of Nb-TiO_2(110)) acquired subsequent to *STEP 4* (UV-treatment) of the *wet chemical* preparation procedure at a a scan size of (a) 50×50 nm and (b) 25×25 nm, (c) displays a line profiles along the broken line indicated in (a).

Besides removing adventitious carbon, the UV-treatment (*STEP 4*) also effects a step change in the hydrophilic nature of both TiO_2(110) and TiO_2(011). This phenomenon is demonstrated in Table I, which lists the water droplet contact angles recorded before and after UV-treatment. In accord with previously published data for TiO_2(110) [4], the surfaces become highly hydrophilic subsequent to the UV-treatment. Such a clear increase in wetability has the potential to be useful as a simple test to ascertain the effectiveness of the UV-treatment; a quick, semi-quantitative assessment can be achieved by visual inspection of the shape of a water droplet delivered to the surface through a hypodermic syringe/needle.

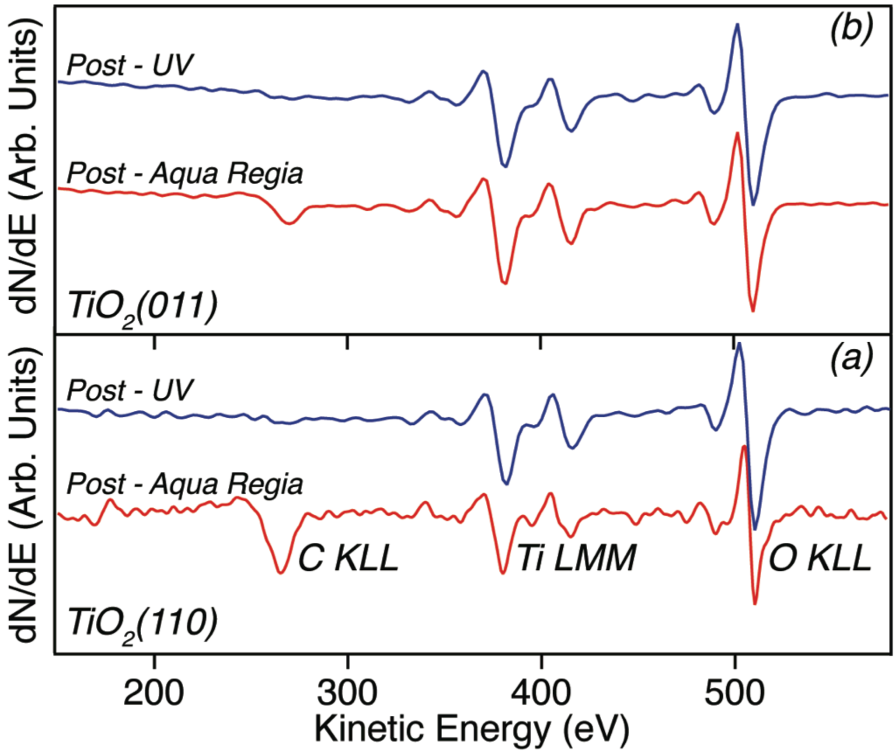

Figure 6.4: AES spectra of (a) TiO_2(110) and (b) TiO_2(011). In each panel one spectrum (red line) has been acquired subsequent to *STEP 3* (aqua regia immersion), the other (blue line) following *STEP 4* (UV-treatment) of the *wet chemical* preparation procedure.

Table 6.1: Water (deionised) droplet contact angles acquired from wet-chemically prepared rutile $TiO_2(110)$ and $TiO_2(011)$ substrates. Data were acquired subsequent to both *STEP 3* (aqua regia immersion) and *STEP 4* (UV-treatment) of the preparation procedure, i.e. before and after UV-treatment. The static sessile drop approach was adopted for these measurements [15].

	Contact Angle (°)	
	Post - Aqua Regia (*STEP 3*)	**Post – UV (*STEP 4*)**
$TiO_2(110)$	**~ 80**	**~ 0**
$TiO_2(011)$	**~ 78**	**~ 0**

Regarding surface order, Figure 6.5 displays LEED patterns from (a) $TiO_2(110)$ and (b) $TiO_2(011)$ post UV-treatment (***STEP 4***). Distinct diffraction spots can be observed in each of the images, indicating that both surfaces possess significant translational order. Surface unit cells are indicated. For $TiO_2(110)$ (Figure 6.5 (a)), the relative dimensions of the unit cell are those expected for an unreconstructed (1×1) surface; all other *wet-chemical* preparations of $TiO_2(110)$ implemented to date have also produced a (1×1) termination [4, 7, 11]. Hence, *wet-chemical* preparation replicates typical UHV preparation (Ar^+ bombardment and anneal cycles) of $TiO_2(110)$ in that both result in a (1×1) termination, at least for lower degrees of bulk reduction in UHV [2]. More notably, given that preparation of $TiO_2(011)$ in UHV results in a (2×1) unit cell [13], a (4x1) surface reconstruction is found for our *wet-chemical* preparation of $TiO_2(011)$. For clarity, both the (4×1) and (1×1) surface units cells are highlighted in Figure 5(b). Additionally, as expected [16], the (0, 2n-1) diffraction spots are absent from the $TiO_2(011)$ LEED patterns, due to the presence of a glide plane. Annealing of this (4×1) phase in UHV changes the surface termination to a (2×1) reconstruction, as demonstrated by Figure 6.6.

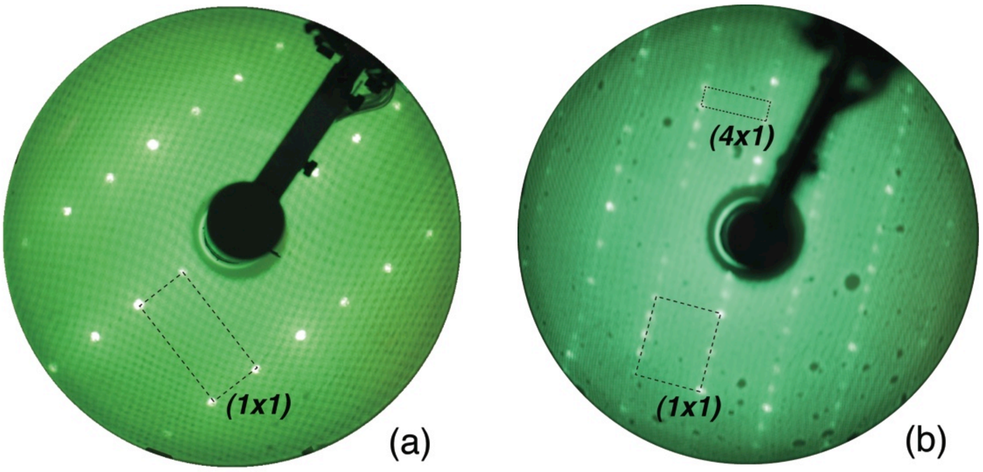

Figure 6.5: LEED patterns of (a) TiO_2(110) and (b) TiO_2(011) acquired subsequent to *STEP 4* (UV-treatment) of the *wet chemical* preparation procedure. Surface unit cells are indicated.

Given that rutile-TiO_2(011) is reported to exhibit enhanced photocatalytic activity [2, 16], the observation of a (4×1) termination following *wet-chemical* preparation has potentially significant implications. It may be that the presence of this *non-UHV* phase underpins the phenomenon, and that previous studies (see Reference [2] and References therein) of the (2×1) structure formed in UHV are not particularly pertinent in this regard. It should, however, be recalled that (1×1) [11] and (2x1) [9] surface unit cells have also been observed for *wet-chemically* prepared TiO_2(011), and one would need to correlate surface termination with photocatalytic activity to facilitate reliable mechanistic insight.

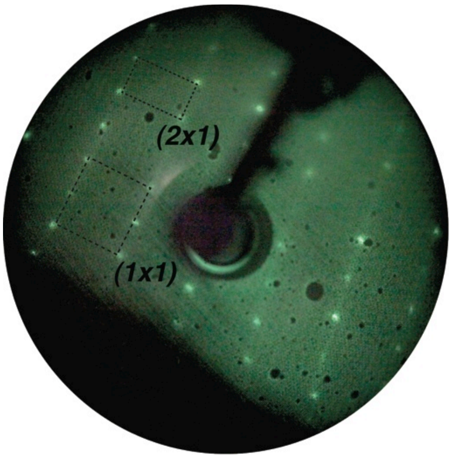

Figure 6.6: LEED pattern of *wet-chemically* prepared TiO_2(011) acquired subsequent to annealing (873 K for 20 min) in UHV. Surface unit cells are indicated.

A very limited set of SXRD measurements were acquired from *wet chemically* prepared rutile-TiO_2(011) for the purpose of further surface characterisation. Figure 6.7 shows a comparison of CTR data, namely the (-4, 0) reflection (bottom) and the (-8, 0) reflection (top), for the *wet chemically* prepared (011) surface alongside the equivalent optimised UHV prepared clean surface from the study by Torrelles *et al* [13].

Given that this very limited data set is by no means comprehensive enough for a quantitative structure determination, it is difficult to establish the exact surface termination on the basis of these measurements. However, coupled with the LEED data, indicating a (4×1) unit cell, the profiles of the integer order rods displayed in Figure 6.7, suggest that the surface exhibits a termination significantly different from the previously reported (2×1).

On the basis of the above, a fully quantitative structure determination of this wet-chemically prepared TiO_2(011)(4×1) surface is clearly of significant interest. Similar effort is also required for the (110) surface, as a (1×1) surface unit cell does not guarantee that the surface termination is identical to that found in UHV (see Reference [2] and References therein). Indeed, it seems plausible that wet-chemically TiO_2 surfaces may be decorated to some extent with surface hydroxyls.

Finally, comparing the current *wet-chemical* preparation recipe with previous variants [3-5, 7-12], it appears to be at least as effective in terms of producing well-defined surfaces suitable for surface science type studies under environmental conditions. In particular, the employment of UV-treatment as a final step enables carbon-free surfaces to be generated Additionally, replacing HF with aqua regia in the chemcial cleaning step eases safety concerns, increasing portability.

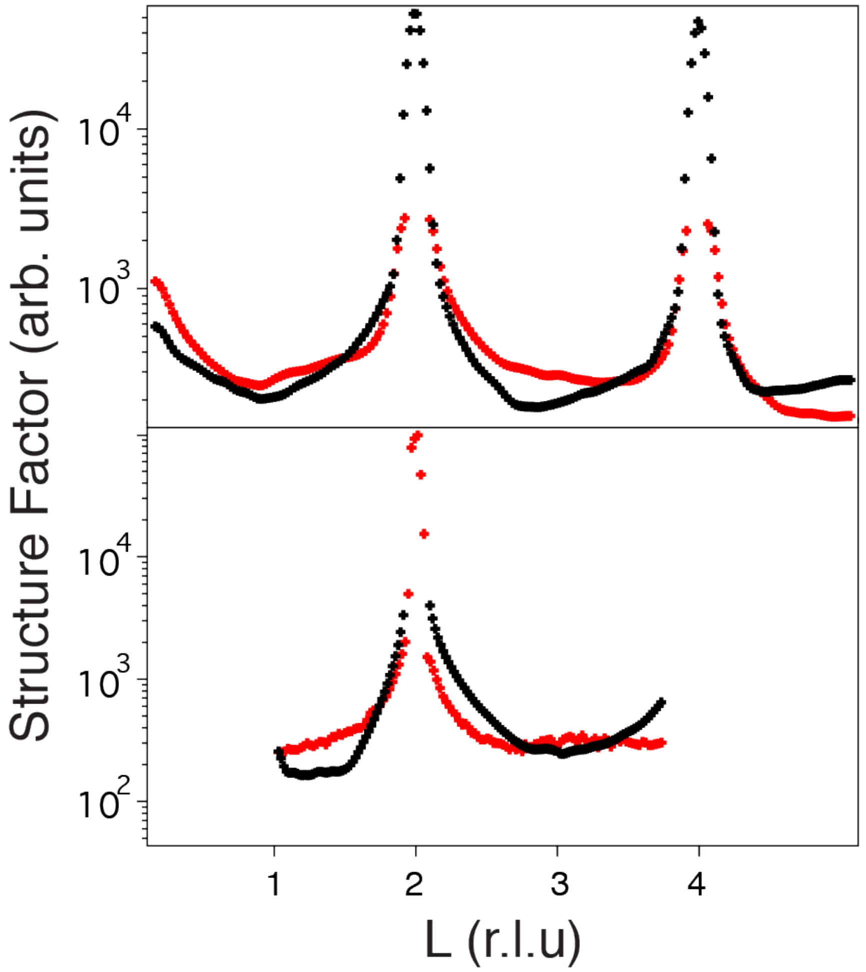

Figure 6.7: Comparison of experimental CTR data from the *wet chemically* prepared (011) surface (black markers) and the equivalent data from the UHV prepared clean surface from the study by Torrelles *et al* [13] (red marker). (Bottom panel) and (Top panel) show experimental data acquired for the the (-4, 0) reflection and the (-8, 0) reflections respectivily.

6.4 Conclusions

In summary, a *wet-chemical* (non-UHV*)* recipe, involving thermal annealing, immersion in aqua regia, and exposure to UV-light, for preparation of single crystal TiO_2 surfaces is presented. The utility of the method is demonstrated through characterisation of rutile-TiO_2(110) and rutile-TiO_2(011) samples subjected to such preparation. Well-defined substrates, displaying relatively large terraces, are produced; surface adsorbed adventitious carbon is depleted by UV-treatment. Furthermore, and perhaps of greatest potential interest, a previously unreported (4×1) termination is observed for TiO_2(011); UHV preparation of the same surface leads to a (2×1) reconstruction.

6.5 References

[1] A. Ciszewski, R. Kucharczyk, K. Wandelt, Special issue on 'Surface science under environmental conditions', Surface Science, 607 (2013) 1.

[2] C.L. Pang, R. Lindsay, G. Thornton, Structure of Clean and Adsorbate-Covered Single-Crystal Rutile TiO_2 Surfaces, Chemical Reviews, 113 (2013) 3887-3948.

[3] R. Franking, R.J. Hamers, Ultraviolet-Induced Grafting of Alkenes to TiO_2 Surfaces: Controlling Multilayer Formation, The Journal of Physical Chemistry C, 115 (2011) 17102-17110.

[4] D.C. Hennessy, M. Pierce, K.-C. Chang, S. Takakusagi, H. You, K. Uosaki, Hydrophilicity transition of the clean rutile TiO_2(110) surface, Electrochimica Acta, 53 (2008) 6173-6177.

[5] C. Kunze, B. Torun, I. Giner, G. Grundmeier, Surface chemistry and nonadecanoic acid adsorbate layers on TiO_2(100) surfaces prepared at ambient conditions, Surface Science, 606 (2012) 1527-1533.

[6] Y. Lu, B. Jaeckel, B.A. Parkinson, Preparation and Characterisation of Terraced Surfaces of Low-Index Faces of Anatase, Rutile, and Brookite, Langmuir, 22 (2006) 4472-4475.

[7] R. Nakamura, N. Ohashi, A. Imanishi, T. Osawa, Y. Matsumoto, H. Koinuma, Y. Nakato, Crystal-Face Dependences of Surface Band Edges and Hole Reactivity, Revealed by Preparation of Essentially Atomically Smooth and Stable (110) and (100) n-TiO_2 (Rutile) Surfaces, The Journal of Physical Chemistry B, 109 (2005) 1648-1651.

[8] Y. Namai, O. Matsuoka, NC-AFM Observation of Atomic Scale Structure of Rutile-type TiO_2(110) Surface Prepared by Wet Chemical Process, The Journal of Physical Chemistry B, 110 (2006) 6451-6453.

[9] H. Takahashi, R. Watanabe, Y. Miyauchi, G. Mizutani, Discovery of deep and shallow trap states from step structures of rutile TiO_2 vicinal surfaces by second harmonic and sum frequency generation spectroscopy, The Journal of Chemical Physics, 134 (2011) 154704.

[10] Y. Yamamoto, Y. Matsumoto, H. Koinuma, Homo-epitaxial growth of rutile TiO_2 film on step and terrace structured substrate, Applied Surface Science, 238 (2004) 189-192.

[11] Y. Yamamoto, K. Nakajima, T. Ohsawa, Y. Matsumoto, H. Koinuma, Preparation of Atomically Smooth TiO_2 Single Crystal Surfaces and Their Photochemical Property, Japanese Journal of Applied Physics, 44 (2005) L511-L514.

[12] Z. Zhang, P. Fenter, L. Cheng, N.C. Sturchio, M.J. Bedzyk, M. Pôedota, A. Bandura, J.D. Kubicki, S.N. Lvov, P.T. Cummings, A.A. Chialvo, M.K. Ridley, P. Bnzeth, L. Anovitz, D.A. Palmer, M.L. Machesky, D.J. Wesolowski, Ion Adsorption at the Rutile-Water Interface: Linking Molecular and Macroscopic Properties, Langmuir, 20 (2004) 4954-4969.

[13] X. Torrelles, G. Cabailh, R. Lindsay, O. Bikondoa, J. Roy, J. Zegenhagen, G. Teobaldi, W.A. Hofer, G. Thornton, Geometric Structure of TiO_2(011)(2×1), Physical Review Letters, 101 (2008) 185501.

[14] T. Zubkov, D. Stahl, T.L. Thompson, D. Panayotov, O. Diwald, J.T. Yates, Ultraviolet Light-Induced Hydrophilicity Effect on TiO_2(110)(1×1). Dominant Role of the Photooxidation of Adsorbed Hydrocarbons Causing Wetting by Water Droplets, The Journal of Physical Chemistry B, 109 (2005) 15454-15462.

[15] A.W. Neumann, R.J. Good, Techniques of Measuring Contact Angles, in: R. Good, R. Stromberg (Eds.) Surface and Colloid Science, Springer US, 1979, pp. 31-91.

[16] T.J. Beck, A. Klust, M. Batzill, U. Diebold, C. Di Valentin, A. Selloni, Surface Structure of TiO_2(011)-(2×1), Physical Review Letters, 93 (2004) 036104.

Chapter 7

Conclusions and Future Work

The work presented in this thesis concerns investigations of metal oxide surfaces beyond UHV, in an attempt to bridge the so-called 'pressure' gap. Surface structure and chemistry have been investigated using several surface sensitive probing techniques, most notably, with surface X-ray diffraction (SXRD), a rigorous quantitative probe of surface geometry. The theory and practice of these techniques has been discussed in Chapter 2.

In Chapter 4 an SXRD study of the α-Cr_2O_3(0001) surface as a function of H_2O partial pressures is described. It has been concluded that the surface geometry is modified in the presence of H_2O at room temperature. A surface terminated with a partially occupied double layer of chromium atoms is concluded at UHV, and at a H_2O partial pressure of ~30 mbar a termination in which each surface Cr atom is bound to an atop OH/H_2O species is concluded. The UHV surface geometry is largely qualitatively consistent with that derived from previous SXRD and LEED-IV measurements. However, there are some quantitative differences in atomic coordinates and fractional layer occupancies. These differences could be attributed to the fact that the surface was dosed with ~ 2000 L of H_2O prior to acquisition of these data under UHV conditions. *Ab initio* calculations performed by Costa *et al* have not predicted the surface structure under any of the two regimes. In light of what has been mentioned, an obvious extension to this work would involve further quantitative studies of the high H_2O partial pressure regime. An interesting technique to apply to this system would be near ambient X-ray photoelectron spectroscopy as it could provide key information in order to evaluate the precise nature of the adsorbed OH/H_2O species at ~30 mbar H_2O; a task that is not so trivial with SXRD. Further as a complementary study it would be interesting to use in situ AFM to get real space imaging of the surface following dosing with H_2O at ~30 mbar. Assuming atomic resolution is achieved, this would be a promising approach to determine adsorption sites. Alongside the above mentioned further experimental work, a re-evaluation of theoretical predications is necessary before a consensus on the exact α-Cr_2O_3 (0001)/H_2O interface geometry can be reached and a solid basis for a nanoscale understanding of surface properties of this material under environmental conditions can be achieved.

In Chapter 5 a second SXRD study elucidating the geometry of the $TiO_2(011)/H_2O$ interface is described. A (2×1) reconstruction in quantitative agreement with previous clean surface studies has been determined in UHV. Most notably, a (1×1) surface termination that is structurally consistent with that predicted by theory was obtained under the high H_2O partial pressure regime. Future work could profitably explore liquid water adsorption on this surface. An understanding of this interface coupled with the current study would give a more complete understanding of the $TiO_2(011)$ surface in an aqueous environment, given the importance of rutile $TiO_2(011)$ as model photocatalyst for water splitting .

Finally, in the last of the experimental chapters of the thesis, Chapter 6, a modified wet chemical recipe for preparation of TiO_2 (110) and (011) has been presented and evaluated. Most importantly, aqua regia has replaced aqueous hydrofluoric acid (HF) as an etching agent, removing the difficulties associated with handling this latter solution. AFM, STM LEED, and AES and SXRD demonstrate that a flat, well-ordered surface is produced by annealing in air, and etching with aqua regia. However, carbon remains on the surface after completion of these steps. As a final measure, irradiation with UV light easily and effectively removes this contamination, resulting in a surface suitable for fundamental surface studies. Most notably, in contrast to the (2×1) surface unit cell found for $TiO_2(011)$ prepared in ultra high vacuum, *wet-chemical* preparation results in a (4×1) termination. To date, this discrepancy remains an open-ended question and certainly requires further investigation. Although this methodology has been successful in producing flat, well ordered and largely contaminant free TiO_2 (110) and (011) surfaces, it is still necessary to evaluate the efficiency of this methodology for the surface preparation of other metal oxide surfaces. Following surface preparation, ancillary characterisation measurements (LEED, AES etc. …), and assuming a well ordered surface, SXRD would be a most promising approach for determining the atomic surface structure of these metal oxide surfaces prepared using this non-UHV methodology, and thus a greatly beneficial means of further evaluating the efficiency of this methodology. The success of this alternative non-UHV sample preparation technique is a major stepping stone in the development of metal oxide surface studies in more ‘real world’ and technologically relevant environments. However a surface science approach would dictate that such samples are well-characterised.